NEUTRON ARM STUDY AND CALIBRATION FOR THE G_E^n EXPERIMENT AT THOMAS JEFFERSON NATIONAL LABORATORY

A Thesis

Presented to

The Faculty of the Department of Physics and Astronomy

California State University, Los Angeles

In Partial Fulfillment

Of the Requirements for the Degree

Master of Science

by

Timothy Ngo

July 2007

APPROVAL PAGE FOR GRADUATE THESIS OR PROJECT

GS-13

SUBMITTED IN PARTIAL FULFILLMENT OF REQUIREMENTS FOR DEGREE OF MASTER OF SCIENCES AT CALIFORNIA STATE UNIVERSITY, LOS ANGELES BY

Timothy Ngo
Candidate

Physics
Field of Concentration

TITLE: Studies and Calibration of Neutron Arm for the G_E^n Experiment at Thomas Jefferson National Laboratory

APPROVED:

Demetrius Margaziotis Faculty Member	Signature
Marty Epstein Faculty Member	Signature
Radi Al Jishi Faculty Member	Signature
Konrad Aniol Department Chairperson	Signature

DATE: ____________________

ACKNOWLEDGMENTS

I would like to thank my adviser, the staff and fellow students at Thomas Jefferson National Laboratory who worked with me during the experiment and offered me valuable support with data analysis. In alphabetical order:

Abrahamyan, Sergey - Yerevan Physics Institute

Aniol, Konrad - California State University, Los Angeles (Adviser)

Craver, Brandon - University of Virginia

Feuerbach, Robert - Jefferson Laboratory (Analysis Expert)

Folts, Ed - Jefferson Laboratory

Hicks, Robby - Jefferson Laboratory

Kelleher, Aidan - College of William and Mary

Kolarkar, Ameya - University of Virginia

Liyanage, Nilanga - University of Virginia (Spokesperson)

Miller, Jonathon - University of Maryland

Riordan, Seamus - Carnergie Mellon University

Shahinyan, Albert - Yerevan Physics Institute

Wojtsekhowski, Bogdan - Jefferson Laboratory (Spokesperson)

ABSTRACT

Neutron Arm Study and Calibration for the G_E^n Experiment at Thomas Jefferson National Laboratory

by

Timothy Ngo

The measurement of the neutron electric form factor, G_E^n, will allow us to solve indirectly for the quark charge distribution inside of the neutron. At Jefferson Lab we have measured G_E^n at four-momentum transfer values of Q^2 at 1.3, 2.4 and 3.4 $(GeV/c)^2$ using a polarized electron beam and polarized Helium target. The scattered electrons off of the Helium target are detected in the BigBite spectrometer and the scattered neutrons from the Helium are detected in the Neutron Arm, which is composed of an array of scintillators. The main focus of this thesis will be devoted to my work on the geometry, timing and energy calibrations of the Neutron Arm.

TABLE OF CONTENTS

LIST OF TABLES

LIST OF FIGURES

1 INTRODUCTION

The mass of visible matter strewn across the universe is due mostly to protons and neutrons, so understanding the internal structure of these particles will allow us better to comprehend how the physical universe came to be. It has been known for many years that protons and neutrons are not fundamental particles, but are instead made up of smaller particles called quarks. Protons and neutrons both have three quarks that can carry electric charge, of $-\frac{1}{3}$e for the down quark and $+\frac{2}{3}e$ for the up quark, where -1e is the unit charge for an electron. In protons there are two up quarks and one down quark giving them a total electric charge of +1e whereas neutrons have two down quarks and one up quark and thus have charge equal to zero. The motion of these charged quarks contributes to the gyro-magnetic moment of the nucleon. Although knowledge of the existence of quarks has been firmly established, the quark distribution in the nucleon is still debatable.

In order to gain better insight into the quark distribution in nucleons we look to their charge density $\rho_{ch}(r)$, and the magnetic density $\rho_m(r)$. In the Breit frame, where the square of the three-momentum transfer of the virtual photon, q^2, is equal to the square of the Lorentz invariant four-momentum transfer of the virtual photon, Q^2, the charge and magnetic densities are Fourier transforms of the Sachs form factors, G_E and G_M, which are defined as

$$G_E = F_1(Q^2) - \tau\kappa F_2(Q^2) \quad and \tag{1}$$

$$G_M = F_1(Q^2) + \kappa F_2(Q^2), \tag{2}$$

where $F_1(Q^2)$ is the Dirac Form Factor and $F_2(Q^2)$ is the Pauli form factor. The anomalous magnetic moment is parametrized by κ different from 1 and $\tau = \frac{Q^2}{4m_N^2}$ is a dimensionless measure of the squared four-momentum transfer in units of the nucleon rest mass, m_N. The best way experimentally to obtain the values of G_E and G_M is through charged lepton, or electron scattering from nuclei. This is due to the fact that the electromagnetic interaction of spin-$\frac{1}{2}$ leptons is a very well understood process through quantum electrodynamics with experimental results that are in excellent agreement with this theory. Since the leptonic vertex, see figure 1, is well understood it restricts all of the uncertainties onto the hadronic vertex, thus making electron scattering an excellent probe to gather information on the internal structure of the nucleons.

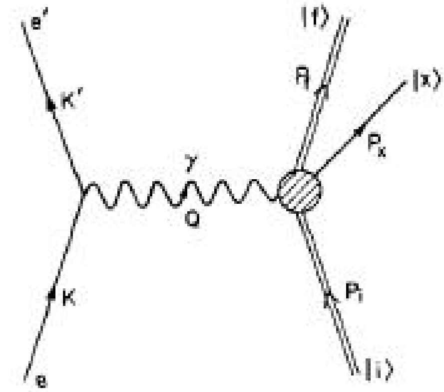

Figure 1: Lowest order diagram for the exclusive electromagnetic (e,e'x) electron scattering process in the one-photon approximation. In the figure K and K' are the four-momenta of the incident and scattered electrons, Q is the four-momentum transfer of the virtual photon, P_i and P_f are the initial and final four-momenta of the nucleus, and P_x is the exclusive particle. Figure courtesy of [1]

Another reason for using the charged lepton, or in this case electron scattering, is due to the electromagnetic interaction itself, particularly the coupling strength characterized by the fine structure constant $\alpha = \frac{e^2}{\hbar c}$ which is relatively small. Therefore only the lowest order process, the more dominant single photon exchange process is traditionally considered and other higher order processes are ignored. With the Sachs form factors the cross section for the unpolarized elastic electron-nucleon scattering can be written using the Rosenbluth form.

$$\left(\frac{d\sigma}{d\Omega_e}\right) = \sigma_{Mott}\left(\frac{G_E^2+\tau G_M^2}{1+\tau} + 2\tau G_M^2 tan^2(\theta/2)\right). \tag{3}$$

with

$$\sigma_{Mott} = 4\alpha^2(\hbar c)^2\frac{E_f^2}{Q^4}\cos^2(\theta/2)\frac{E_f}{E_i}, \tag{4}$$

where the Mott cross section describes the scattering from a point like spin-$\frac{1}{2}$ target and θ represents the electron scattering angle, E_i and E_f represent the electron's initial and final energy. Early measurements of the form factor at moderate Q^2 using the Rosenbluth technique established a form factor scaling law that related three of the four nucleon form factors to the dipole in terms of their Q^2 dependence such that,

$$G_E^p(Q^2) \approx \frac{G_M^p(Q^2)}{\mu_p} \approx \frac{G_M^n(Q^2)}{\mu_n} \approx G_D \equiv (1+Q^2/0.71)^{-2}. \tag{5}$$

However with new measurements using polarized electron beams the proton form factors at Q^2 up to 3.5 $(GeV/c)^2$ have shown that above 1.0 $(GeV/c)^2$ the scaling laws are inconsistent with the dipole form.

Recent experiments at Jefferson Laboratory [2], [3] using double polarization techniques, in which the electron beam and the target are both polarized, found that the ratio of $\frac{\mu G_E^p}{G_M^p}$ shows a steep decline above 1.0 $(GeV/c)^2$ where the scaling laws predict an approximately constant value as Q^2 is increased, see

Fig 2. The mechanisms causing this behavior in the proton within this regime of Q^2 may also play a role in the neutron. However, measurements pertaining to the form factors of the neutron are extremely limited. This limitation is due to the lack of a free neutron target and the dominance of G_M^n over G_E^n. New experiments using a double polarization method have made it possible to measure the neutron form factors with greater certainty at higher Q^2 as shown in the experiments at Mainz [4], [5], [6], and Bates [7]. Currently G_M^n is being analyzed bringing our knowledge of this form factor up to $Q^2 = 4.8\ (GeV/c)^2$ and G_E^n is currently measured up to $Q^2 = 1.5\ (GeV/c)^2$.

Even as experiments are being built to expand our understanding of G_E^n, new studies are contradicting our understanding of what G_E^n is supposed to be. A recent model-independent analysis of the internal structure of the neutron shows that it contains a negative central charge density as well as a long negative tail, contrasting the expectation of a positive central charge density due to the negative pion cloud [8]. It is in this light that we now look to the use of double polarization polarized experiments to extract G_E^n and G_E^n at higher Q^2 with greater certainty, see figure 3.

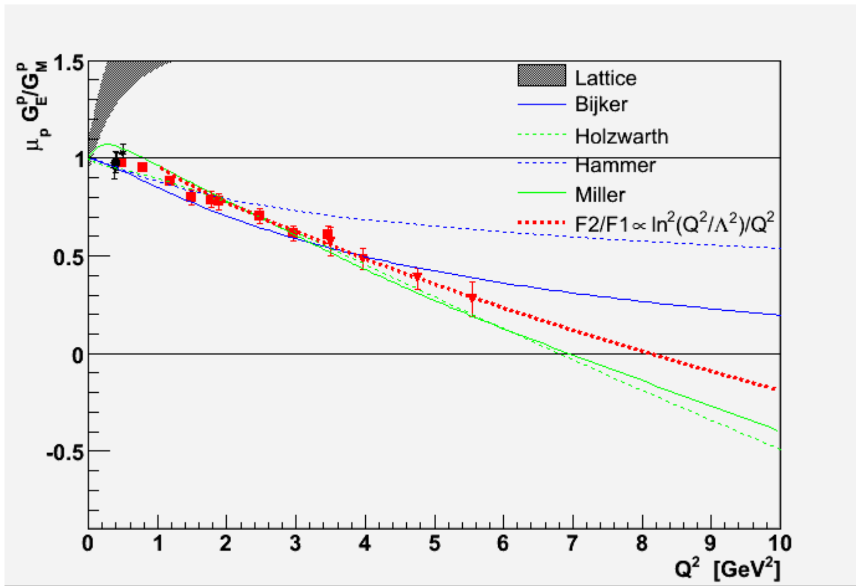

Figure 2: Various experimental results for $\frac{\mu G_E^p}{G_M^p}$

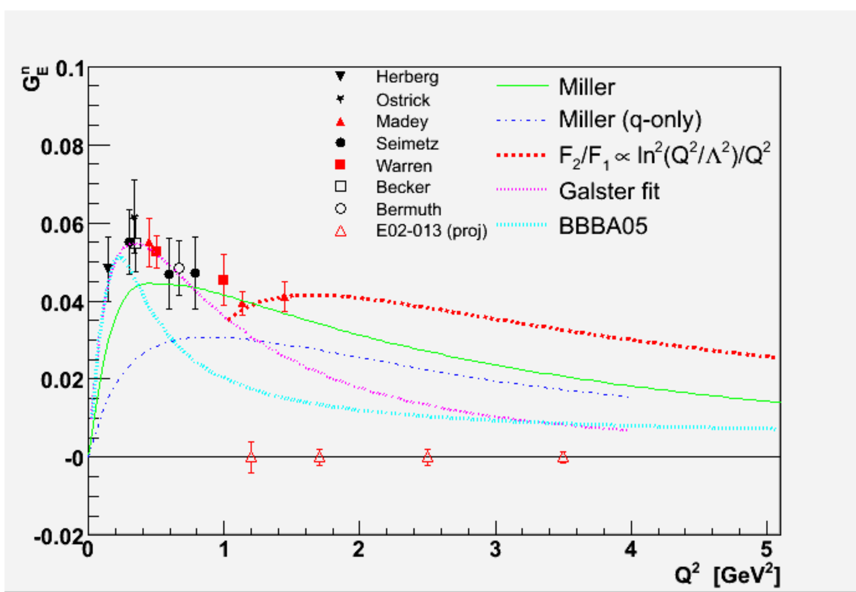

Figure 3: Various experimental results for G_E^n

In using electron scattering on nuclei there are either inclusive or exclusive electron scattering measurements. Inclusive scattering is when only the electron is detected after it interacts with the nuclei whereas exclusive electron scattering requires some particle detected in coincidence with the scattered electron. In either case, to extract the Sachs form factor we use the method of Rosenbluth decomposition [9]. Due to different angular weights in equation 3, G_E and G_M can be separated by varying the kinematical conditions of the incident and the scattered electrons, such as incident energy and scattering angle, at a constant Q^2 value.

In inclusive scattering experiments no information on the nuclei is recorded after the interaction; only the form factors corresponding to the longitudinal and transverse polarizations of the exchanged virtual photon can be obtained. On the other hand with exclusive scattering where an additional particle is detected in coincidence with the electron it is possible to obtain much more information pertaining to nuclear structure.

It can be shown that by using unpolarized exclusive electron scattering, four of the six nuclear response functions can be determined namely $\mathscr{R}^L, \mathscr{R}^T, \mathscr{R}^{TT}$ and $\mathscr{R}^{TL}$. The subscripts T and L correspond to the longitudinal and transverse polarization of the virtual photon. If a polarized electron is used then a fifth response function can be solved for by using the helicity to separate $\mathscr{R}^{TL\prime}$ from the unprimed response functions. The last response function, $\mathscr{R}^{T\prime}$, can be extracted from $\mathscr{R}^{TL\prime}$ but requires the use of a polarized hadronic target and by varying the electron kinematics. The nuclear response functions contain all the information relating to the nuclear structure.

Donnelly and Raskin [1], [10] provided a prescription to describe the cross sections and asymmetries to obtain the form factors in doubly polarized electron scattering experiments. In the Born approximation the elastic electron-nucleon scattering cross section can be written as a sum of two parts,

$$\left(\frac{d\sigma}{d\Omega_e}\right)_h = \Sigma + h\Delta \tag{6}$$

where h corresponds to the incoming electron helicity with a value of ± 1. The term Σ corresponds to the unpolarized elastic cross section, and Δ, which is non-zero if the electron is longitudinally polarized, is the polarized cross section.

The cross section written in terms of the nuclear response functions is,

$$\begin{aligned}\left(\frac{d\sigma}{d\Omega_e}\right) &= \sigma_{Mott} f_{rec}^{-1}\{(\nu_L \mathscr{R}^L + \nu_T \mathscr{R}^T + \nu_{TT} \mathscr{R}^{TT} + \nu_{TL} \mathscr{R}^{TL}) \\ &\quad + h(+\nu_{T'} \mathscr{R}^{T'} + \nu_{TL'} \mathscr{R}^{TL'})\} \\ &\equiv \Sigma + h\Delta.\end{aligned} \tag{7}$$

where σ_{Mott} is the Mott cross section equation 4. f_{rec} is the nuclear recoil correction in the extreme relativistic limit,

$$f_{rec} = 1 + \frac{Ek' - E'kcos\theta_e}{k'M_{target}} \tag{8}$$

where k and k′ are the initial and final three-momenta of the electron.

The unpolarized electron-nucleon scattering cross section Σ for elastic scattering off a free nucleon at rest is again the Rosenbluth form (equation 3). The polarized part is given by

$$\Delta = -2\sigma_M \sqrt{\frac{\tau}{1+\tau}} tan\left(\frac{\theta}{2}\right) \left[\sqrt{\tau(1+(1+\tau)tan^2\left(\frac{\theta}{2}\right))} cos\theta^\star G_M^2 + sin\theta^\star cos\phi^\star G_M G_E\right], \tag{9}$$

where $\theta^\star$ is the polar angle and $\phi^\star$ is the azimuthal angle of the target polarization in the laboratory frame with respect to the axis of the momentum transfer.

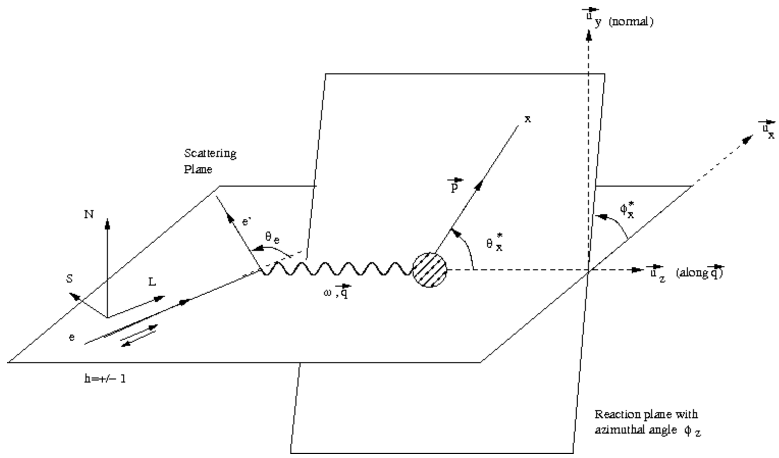

Figure 4: Kinematics and coordinate systems for the exclusive (e,e'x) scattering process. Figure courtesy of [1]

In solving for G_E^n we look to the asymmetry A_{phys} for the electron nucleon scattering cross section, which is defined as

$$A_{phys} = \frac{\left(\frac{d\sigma}{d\Omega_e}\right)_+ - \left(\frac{d\sigma}{d\Omega_e}\right)_-}{\left(\frac{d\sigma}{d\Omega_e}\right)_+ + \left(\frac{d\sigma}{d\Omega_e}\right)_-} = \frac{\Delta}{\Sigma}. \tag{10}$$

expanding the Δ and Σ we then have,

$$\begin{aligned} A_{phys} = & -\frac{2\sqrt{\tau(\tau+1)}tan\left(\frac{\theta}{2}\right) G_E^n G_M^n sin\theta^\star cos\phi^\star}{(G_E^n)^2 + (G_M^n)^2(\tau + 2\tau(1+\tau)tan^2\left(\frac{\theta}{2}\right))} \\ & - \frac{2\tau\sqrt{1+\tau+(1+\tau)^2 tan^2\left(\frac{\theta}{2}\right)}tan\left(\frac{\theta}{2}\right)(G_M^n)^2 cos\theta^\star}{(G_E^n)^2 + (G_M^n)^2(\tau + 2\tau(1+\tau)tan^2\left(\frac{\theta}{2}\right))}. \end{aligned} \tag{11}$$

The experimentally measured asymmetry A$_{exp}$ will be reduced from this ideal asymmetry due to the finite polarization of the electron beam, P_e, and the neutrons in the ^3He target, P_n, the dilution D of atoms other then ^3He in the target, and the dilution of events originating from random coincidences and reactions other than quasi-elastic scattering expressed as $V = (1+\frac{N}{S})^{-1}$ where $\frac{N}{S}$ is the noise to signal ratio. The experimentally measured asymmetry can then be expressed as

$$A_{exp} = P_e \cdot P_n \cdot D \cdot V \cdot A_{phys}, \tag{12}$$

By aligning the target spin so that it is perpendicular to the momentum transfer thus giving us the perpendicular asymmetry,

$$A_{perp} = -\frac{G_E^n}{G_M^n} \cdot \frac{2\sqrt{\tau(\tau+1)}tan\left(\frac{\theta}{2}\right)}{(G_E^n/G_M^n)^2 + (\tau + 2\tau(1+\tau)tan^2\left(\frac{\theta}{2}\right))} \tag{13}$$

is obtained. Since $(G_E^n/G_M^n)^2$ is small compared to the second term of the denominator, G_E^n is then nearly proportional to A_{perp}. To extract G_E^n out of A_{perp} knowledge of G_M^n is required, which is now being analyzed up to $Q^2 = 4.8\ (GeV/c)^2$.

In the G_E^n experiment we measure the electric form factor of the neutron up to a momentum transfer of $Q^2 = 3.4\ (GeV/c)^2$ using a polarized electron beam and polarized target. This measurement of G_E^n at $Q^2 = 1.3$, 2.4 and 3.4 $(GeV/c)^2$ and the already existing data on the magnetic form factor of the neutron G_M^n will give us a better picture of how the valence quarks are distributed inside the neutron. Along with the polarized target and polarized beam, an electron detector, BigBite, and neutron detector, Neutron Arm/BigHand, are needed to track and detect events in coincidence. Although equation 13 suggests that we need only measure the electron's elastic scattering asymmetry, in practice it is essential to detect the neutron in coincidence because we need to be certain that the electron scattered off a neutron and not a proton. The BigBite spectrometer is used for detection and track reconstruction of the scattered electron, and as a trigger for the Neutron Arm, whereas the Neutron Arm is used to detect the scattered neutrons and protons from the reaction. My part on this experiment primarily dealt with the geometry, energy and timing calibrations of the Neutron Arm and thus will comprise most of this thesis, although I will also briefly describe other parts of the experiment and its detectors.

3 EXPERIMENTAL SETUP

The (G_E^n experiment took place in Hall A at Jefferson National Laboratory, and took data from February 02, 2006 to May 12, 2006. The experiment is a doubly polarized experiment in which a polarized electron beam provided by the accelerator facility at Jefferson Laboratory, and a polarized neutron target is used. The polarized electron beam can achieve an electron polarization of about 75% and the polarized neutron target is obtained from a ^{3}He target, which can achieve a neutron polarization of up to 50%. To detect the scattered electron with momenta between 1200-1500 MeV/c, we use the BigBite spectrometer and calorimeter package, with has a solid angle acceptance of about 76msr. To detect the scattered neutrons from the target the Neutron Arm was built at Jefferson Laboratory to have a solid angle acceptance of 100msr at 8 meters. The Neutron Arm comprise of 340 scintillator bars arranged into nine separate planes. Each scintillator bar will have two PMTs attached to the scintillator at the 2 ends. The Neutron Arm was optimized to have the best efficiency for a neutron momentum of 2.58 GeV/c, which is due to a incidental electron beam energy of 3.2 GeV, our highest Q^2 point. A figure of the experimental setup is shown in figure 5.

My contribution to the experiment, and the main focus of this thesis will be centered around geometry, and the timing and energy calibration on the Neutron Arm. The timing and energy calibrations will be done using long tracks created by muons and protons through the Neutron Arm. I will also briefly describe the target and the BigBite spectrometer and detector package.

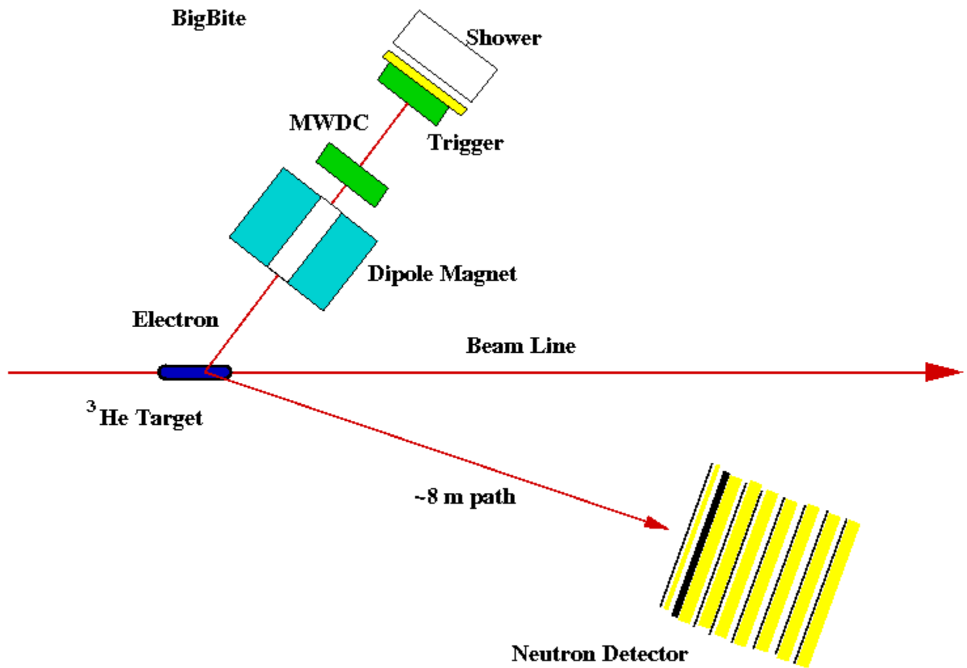

Figure 5: Layout of the experiment, not drawn to scale. Courtesy of [11]

4 NEUTRON DETECTION

To detect neutrons in G_E^n, a large neutron detector referred to as the Neutron Arm was built at Jefferson Laboratory. The size of the Neutron Arm as a whole was 4.2x2.0x6.2m^3 and was comprised of 340 scintillator bars, each connected to two PMTs. The solid angle on the Neutron Arm is approximately 100msr at a distance of 8 meters. The Neutron Arm arm is built with an aspect ratio of 1:2.5 is well matched with BigBite's acceptance. The time resolution is expected to be 0.3ns at a distance of 8 meters which leads to a neutron momentum resolution of 250 MeV/c for a neutron momentum of 2.58 GeV/c [11]. This section will describe the geometry of this detector and how it works.

4.1 SCINTILLATION DETECTORS

The Neutron Arm employs an array of scintillator bars of varying sizes to detect protons and neutrons. Scintillation Detectors in the Neutron Arm are made up of organic plastics and work by giving off light as charged particles such as protons or charged pions deposit energy as they pass through them. Neutrons will cause scintillators to emit light only when they hit a nucleus in the shielding or the scintillator causing charged particles such as protons to be ejected into the scintillator.

Because neutrons can not be directly detected, enough conversion material such as lead must be placed in front of the detector so that there is a high probability of the neutron interacting and causing a shower of secondary particles to traverse the scintillators. In order to calibrate scintillation detectors we use cosmic muons that create vertical tracks in the Neutron Arm to calibrate the PMTs, and protons from hydrogen and helium which create vertical tracks in the Neutron Arm to calibrate the timing.

To read out the amount of light emitted by the scintillator bars we attach photomultiplier tubes (PMTs) to both ends of the scintillator bars, which serve to amplify and digitize the light signal. These signals can then be used to give us both the amplitude of the signal using an Analog-To-Digital Converter, which correlates to the energy deposited by the particle passing through the scintillator, and the time when the particle passes through the detector, using a Time-To-Digital Converter (TDC).

4.2 NEUTRON ARM

The scintillator shapes used were long and rectangular, a shape which would provide a high light collection efficiency[12]. PMTs were attached to both ends of the scintillators via a light guide to channel light into the PMTs face glass and to reduce the position dependence of the collected light. An example of the scintillator used can be found in figure 20 in the appendix. The scintillator bars in the Neutron Arm are arranged into modular cassettes which allow for easy installation into the frame of the Neutron Arm, as shown in figure 6 and 7.

The structure of the cassettes which includes a 1.27cm thick plate of iron on the front, used to increase the rate of converting protons to neutrons, and a 0.64cm thick plate of aluminum on the back to support the scintillator bars. The cassettes sizes also vary depending on the size of scintillators that they contain. The veto cassettes contain veto scintillator bars that are 2x11x70 cm^3 (widthxheightxlength), and 2x11x110 cm^3 in size. The veto counters were used to allow us to distinguish between neutrons and charged particles such as protons passing through Neutron Arm. The smaller width of the veto scintillators reduces the possibility of the neutron creating a shower inside the veto counters, but will still allow protons to fire, thus providing the the ability to select out proton and neutron events.

Each veto cassette contains eight short scintillator bars, which are situated closer to the beam line and eight long scintillator bars that are placed farther away from the beam line. The difference in the lengths compensates for the increased counting rate that occurs as the scintillator bars are placed closer to the beam line. The veto cassettes are placed in the first two planes of the Neutron Arm where each plane contains six cassettes.

In front of the first veto plane there is a veto wall made out of lead. The sole purpose of this wall is to reduce the rate at which the veto detectors will fire due to noise and spurious events. Although this does decrease our overall statistics, the veto wall makes it possible to use the veto detectors to identify charged particles. Without this veto wall the rate in the veto plane would be much higher, causing an increased dead time in each of the bars.

After the veto planes, there is a 1.27cm thick layer of iron and 2.54cm thick of lead used as a converter for neutrons. The next four planes in the Neutron Arm which have the naming convention N1, N2, N3, and N4 contain cassettes that have Carnegie Mellon University (CMU) bars and have dimensions of 5x11x180 cm^3. Each of the planes N1 through N4 has five CMU cassettes where each cassette has five scintillator bars. However, in planes N1 and N3 there exists a sixth cassette which are Glasgow cassettes and contain five scintillator bars with dimensions of 10x20x180 cm^3. These cassettes sit at the top of the last CMU cassette in the N1 and N3 plane.

Following the N4 plane, planes N5, N6, and N7 each contain four University of Virginia (UVA) cassettes, of which contain ten scintillator bars with dimensions 10x20x160 cm^3. The planes N5 through N7 also have a Glasgow cassette at the top of the last UVA cassette, which are the same ones that sit on top of planes N1 and N3. A diagram of the side view and a front view of one of the planes of the Neutron Arm is shown in figures 6 and 7. Figures of the other planes in the Neutron Arm can be found in the appendix.

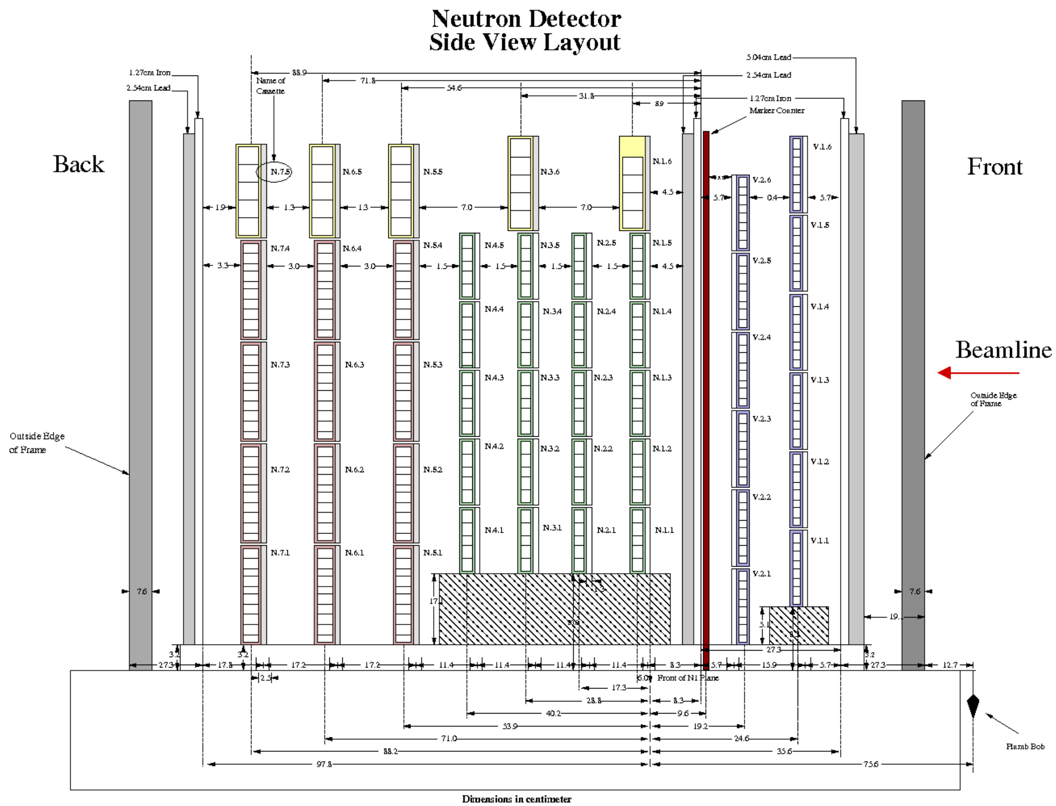

Figure 6: The side view of the Neutron Arm includes 2 veto planes (V1 and V2), 1 plane of marker counter, 7 planes of neutron detectors made up of CMU(N1-N4),UVA(N5-N7) and Glasgow(N1.6,N3.6,N5.5,N6.5,N7.5), and 3 planes of lead mounted on iron. Included in the drawing is the measurement from the center of the different planes to the center the N1 plane. The diagram is exaggerated for clarity purposes

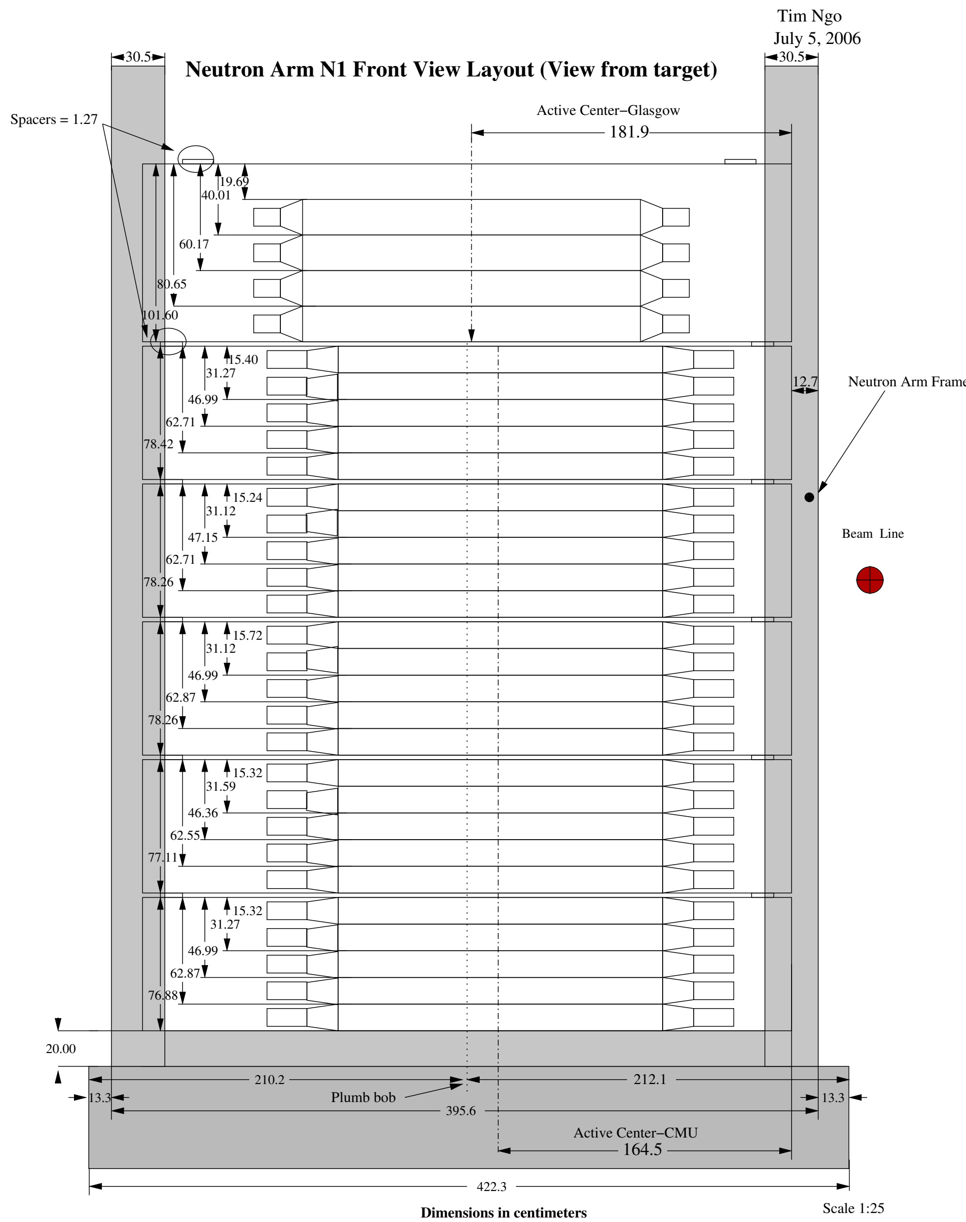

Figure 7: N1 Plane

4.3 FIDUCIAL AND FOIL MARKERS

During the experimental run fiducial and foil markers were used by the survey team in order to keep track of the location of the Neutron Arm. Two survey reports were done for the experiment, one before experimental data and the other after experimental data was taken. The original survey reports can be found in figure 98 through figure 103 in the appendix. Since the position of the plumb bob labeled CTR#, where # represents the kinematic period, in the first set of report was not included in the second, the relative distances from the fiducial to the plumb bob and the foil to the plumb bob found from the first report was applied to the second survey report to obtain the position of the plumb bob.

Knowing the coordinates of the plumb bob allows us to understand where the different planes of the Neutron Arm are in relation to the target. Refer to figure 8 for clarification of the position of the fiducial and foil markers in relation to the plumb bob. To find the position of the plumb bob in the hall, just subtract relative plumb bob position values in figure 8 from the fiducial values in the survey.

Also obtained from using the fiducial and foil marker data is the angle of the Neutron Arm with respect to the beam line. This angle is found to be 30 degrees, and is also shown in figure 8. In table 1 are the coordinates of the plumb bob for each of the kinematic runs and its distance from the target. The value that appears in the drawings figure 104 and figure 105 namely 12.00, 9.26, and 6.51 meters are the distance from the target to the center of the Neutron Arm Detector.

HABH* – Fudicial Marker

BHF* – Foil Marker

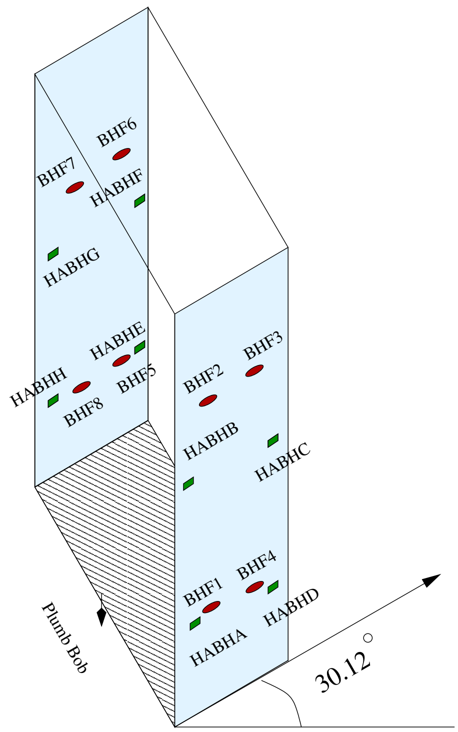

Relative Distance of Fudicial and Foil to Plumb Bob

	Z(mm)	X(mm)	Y(mm)
HABHA	1345	−1597	1171
HABHB	1341	−1597	3413
HABHC	2578	−880	3410
HABHD	2569	−880	1171
HABHE	518	2655	1183
HABHF	515	2648	3424
HABHG	−707	1937	3425
HABHH	−711	1932	1182

Beam Line +Z

Figure 8: The Fiducial and Foil Marker Positions

Survey Position #	Kinematic #	Z(mm)	X(mm)	Y(mm)	Plum bob to target(mm)	Θ_{plm}
Survey A1040						
1	2a	9649.9	5155.3	2510.0	10940.6	28.11°
2	3	9889.7	4736.9	2509.8	10965.6	25.59°
3	1 and 4	6682.7	4803.9	2512.9	8230.2	35.71°
Survey A1068						
1	2a	9650.3	5159.9	2512.6	10943.1	28.13°
2	3	9887.4	4743.4	2511.9	10966.3	25.63°
3	1 and 4	6678.3	4806.3	2514.6	8228.0	35.74°
4	2b	9447.4	5509.2	2512.8	10936.4	30.25°

Table 1: The position of the Plumb bob for the 4 kinematic runs and its distance from the target.

4.4 NEUTRON ARM POSITION

During the experiment the Neutron Arm was placed on rails so that it could be moved to different positions for different kinematics. The diagram in figure 9 shows the Neutron Arm and its relation to one of the rails and the center of the target. The rail we refer to here is the one closest to the beam line and running 30° to it. The center of this rail is used to measure to the center of the detector. The diagram only used the position of the fiducial markers that were higher along in the Y position in relation to the center of the target.

A drawing of the rails and their dimensions is found in figures 104, 105, and 106 in the appendix and was provided by Robbie Hicks. In these drawings the distance is given from the target to the center of the detector and not the plumb bob. The data points were taken by the survey team and reported in document DT A1068, figure 102.

4.4.1 CALIBRATION PERIOD

During the calibration period the position of the center of the detector was 3.070 meters away from the rail closest to the beam, at a nominal angle of 35.1 degrees and 6.51 meters away from the target center. The plumb bob was 5.501 meters away from center of the target. The survey team only provided the positions of the foil for this position and no fiducial measurements. The detector was in this position during the commissioning of the experiment which lasted from 02/24/06 to 03/04/06.

4.4.2 KINEMATIC PERIOD 1

For kinematic position 1 the center of the Neutron Arm was at 3.303 meters away from the rail closest to the beam line at a nominal angle of 35.1 degrees and 12.000 meters away from the target. The distance to the plumb bob from the target center was 10.943 meters. For this kinematic period the beam energy was 1.519 GeV, and the run lasted from 03/05/06 to 03/08/06.

4.4.3 KINEMATIC PERIOD 2

The Neutron Arm initially was in the nominal position where the center of the detector was 2.109 meters away from the rail closest to the beam line at a nominal angle of 28.3 degrees and 12.000 meters away from the center of the target. The plumb bob was 10.943 meters away from the target.

However, since the center of the detector bar does not coincide with the center of the Neutron Arm it had to be moved into the correct position. The majority of the data was taken with the position of the center of the detector at 2.515 meters away from the rail closest to the beam line at a nominal angle of 30.2 degrees and 12.00 meters away from the center of the target. The position of the plumb bob was 10.966 meters away from the center of the target. This position was also referred to as kinematic period 2b. The beam energy for this period was 2.641 GeV, and the data was collected from 03/09/06 to 03/21/06, and once again from 04/17/06 to 04/24/06.

4.4.4 KINEMATIC PERIOD 3

Kinematic position 3 ran with the highest beam energy at 3.290 GeV, and would give us the highest Q^2 on the neutron to date. The position of the center of the detector was 1.266 meters away from the rail closest to the beam line at a nominal angle of 30.25 degrees, and 12.000 meters from the target. The position of the plumb bob was 10.936 meters away from the center of the target. Data was collected for this data point from 03/24/06 to 04/17/06, then again after switching back from kinematic period 2, from 04/24/06 to 05/03/06.

4.4.5 KINEMATIC PERIOD 4

The purpose of this kinematic position was to get more data that were similar to kinematic position 1, since kinematic position 1 had only three days of data taking, and settings such as, the high voltage system, and wiring pertaining to the Neutron Arm were still being tweaked. The data collected in this run would have the Neutron Detector in a very stable setting. In kinematic position 4 the center of the detector was 3.303 meters away from the rail closest to the beam line at a nominal angle of 35.1, and 9.26 meters away from the center of the target. The position of the plumb bob, 8.228 meters away from the center of the target. The beam energy for this kinematic period was 2.079 GeV. Data was collected from 05/03/06 to 05/12/06.

	To Center of ND					To Plumb Bob
Position Name	Date	Beam Energy(GeV)	Distance from Target(m)	Theta (degrees)	Distance to Rail (m)	Distance from Target(m)
Calib	02/24/06-03/04/06	N/A	6.51	35.1	3.070	5.501
Kin 1	03/05/06-03/08/06	1.519	12.00	35.1	3.303	10.943
Kin 2	03/09/06-03/21/06	2.641	12.00	28.3	2.109	10.943
	04/17/06-04/24/06					
Kin 3	03/24/06-04/17/06	3.290	12.00	30.3	1.266	10.936
	04/24/06-05/03/06					
Kin 4	05/03/06-05/12/06	2.079	9.26	35.1	3.303	8.228

Table 2: Kinematic Position

Track and ND Position Layout using fiducial markers provided in survey document DTM #A1068
Top View with target center as origin.
Dimensions are in centimeters unless noted otherwise.
+Y Position is not dipicted here

	Kinematic 2a		Kinematic 3		Kinematic 1a		Kinematic 2b	
Fudicial Position	Position 1		Position 2		Position 3		Position 4	
	z	x	z	x	z	x	z	x
HABHB	1100.1	356.6	1123.9	314.9	802.0	321.2	1079.6	391.4
HABHC	1223.7	428.4	1247.5	386.9	925.9	392.6	1203.3	463.1
HABHF	1015.7	708.4	1039.2	738.7	718.9	745.4	995.7	815.4
HABHG	893.5	709.1	917.0	667.3	596.5	674.4	873.4	744.2

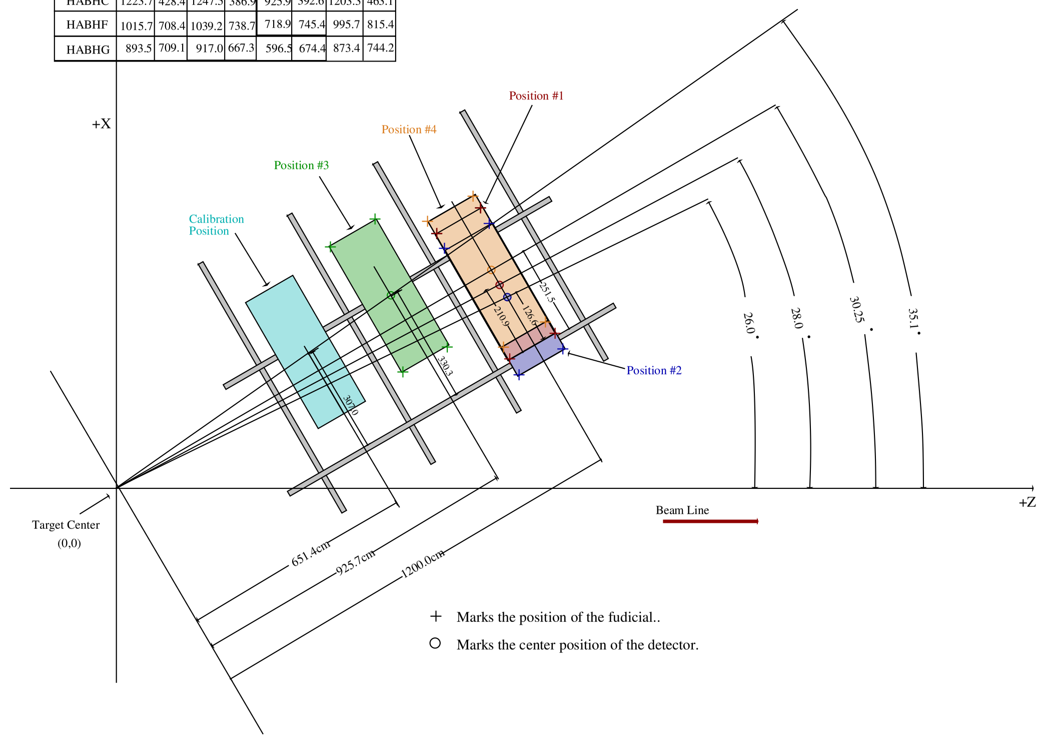

Figure 9: Neutron Arm position relative to Target Center.

4.5 MARKER COUNTER

Marker Counters were used as a device to help calibrate the Neutron Arm along the face of the different planes. The four Marker Counters were placed in front of the N1 plane and ran lengthwise vertically. Each Marker Counter consisted of organic plastic scintillators with the dimensions of 2.54x2.54x304.8cm^3 . The Marker Counters ran vertically so that we could use them to obtain the propagation velocity of light in the scintillator bars in the N1 to N7 planes. Since the absolute positions of these counters were known they were also used to calibrate the horizontal position of the scintillator bars in the N1 to N7 planes. Figure 10 shows the Marker counters relative to the N1 plane.

The angle between the Marker counter and the beam line changed as the Neutron Arm was moved during each of the kinematic runs. The position of the Neutron Arm was obtained from the survey team using DT A1068. In Table 3 Θ_{plm} refers to the angle between the position of the plumb bob to the beam line. The distance between the plumb bob and the front of the N1 plane is 73.7cm. $\Delta\Theta_m$ is the angle between the different Marker Counters to the plumb bob, and Θ_m is the angle between the different Marker Counters to the beam line. Θ_{frm} refers to the angle between the Neutron Arm center and the beam line, which reflects the fact that the plumb bob is off center by 0.953cm. Θ_{frm_nom} is the nominal angle between the Neutron Arm and the beam line given in the drawings by Robby Hicks, figure 104, and a report on the Marker bars by Dimitri Nikolenko [13]. The angles were obtained by using the survey data which provided the location of the plumb bob. Refer to Fig 11 for the descriptions of the variables used. The angles provided in Table 3 were obtained as follows:

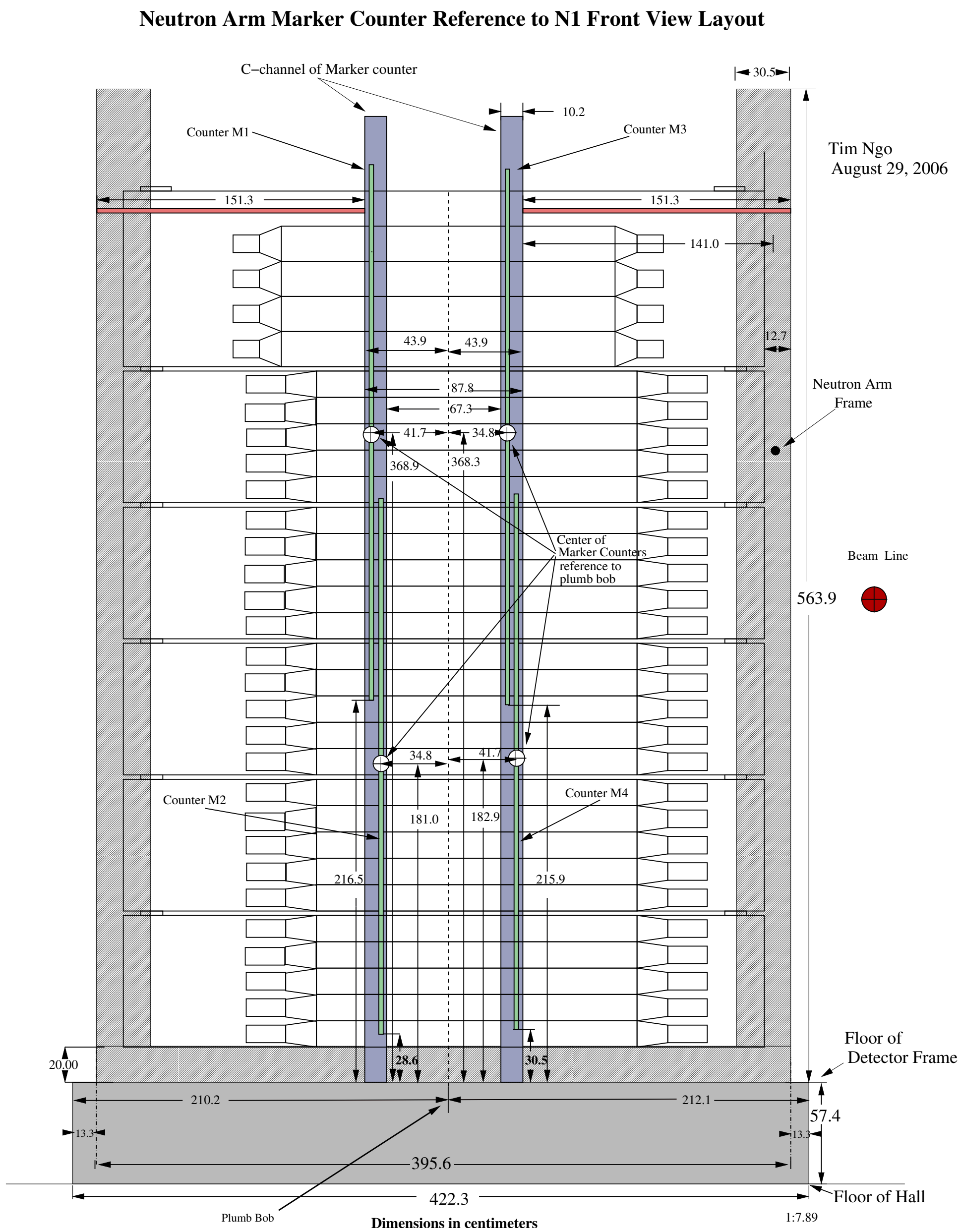

Figure 10: A majority of the dimensions for the Marker counters were provided in a report by Dimitri Nikolenko

$$
\begin{aligned}
\Theta_{plm} &= \tan^{-1}\left(\frac{x_{plm}}{z_{plm}}\right) && (14)\\
r_{plm} &= \sqrt{x_{plm}^2 + z_{plm}^2} && (15)\\
r &= r_{plm} + r_{mark} && (16)\\
\Delta\Theta_{m1} &= \tan^{-1}\left(\frac{x_{m1}}{r}\right) && (17)\\
\Theta_{m1} &= \Theta_{ctr} + \Delta\Theta_{m1} && (18)\\
&= \tan^{-1}\left(\frac{x_{plm}}{z_{plm}}\right) + \tan^{-1}\left(\frac{x_{m1}}{r}\right) && (19)
\end{aligned}
$$

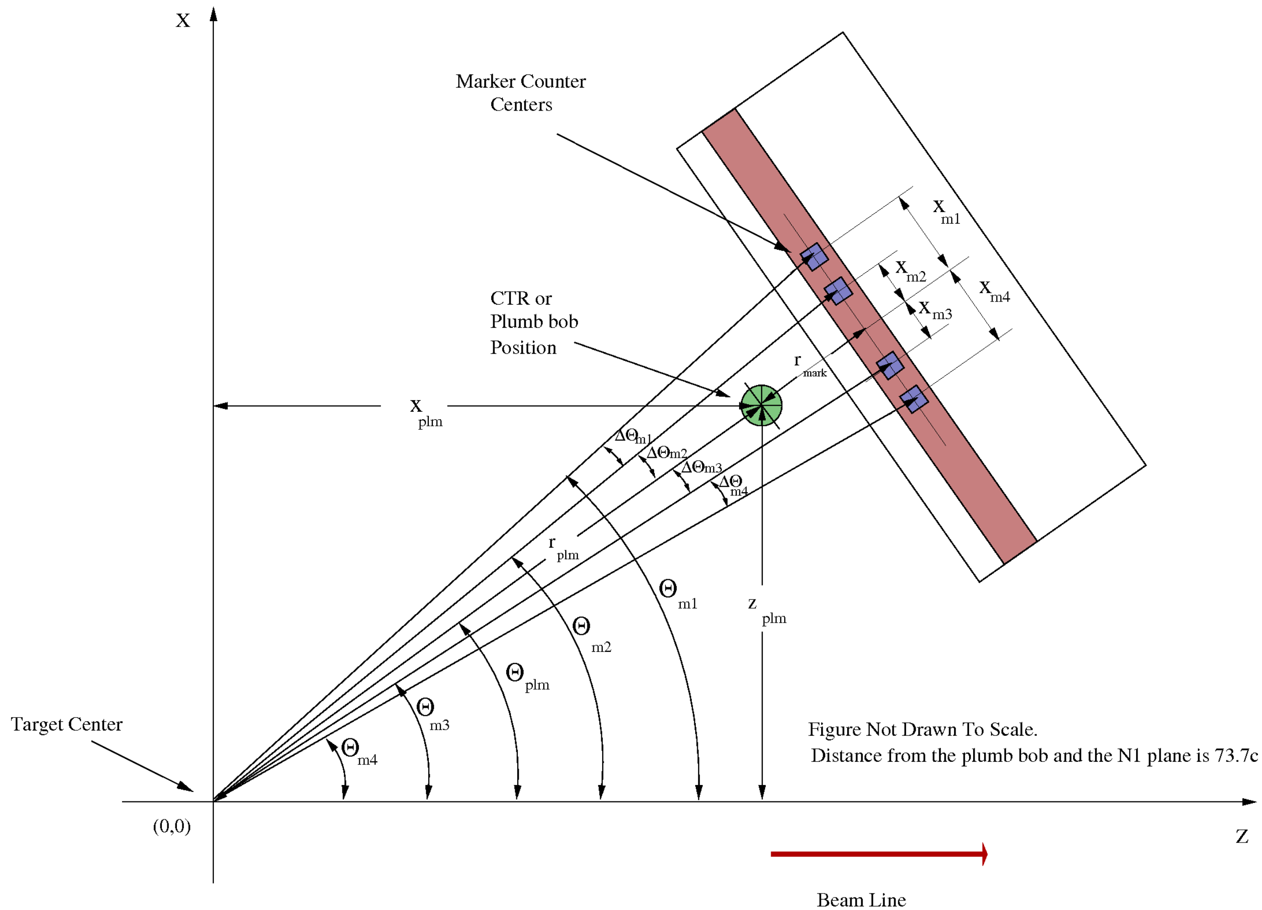

Figure 11: Diagram showing the angle of the Marker Counter in relation to the beam line.

Survey Labeled Position		Position 3	Position 1	Position 4	Position 2	Position 3
Θ	Calibration	Kinematic 1	Kinematic 2a	Kinematic 2b	Kinematic 3	Kinematic 4
Θ_{frm_nom}	35.1°	35.1°	28.0°	30.1°	26.0°	35.1°
Θ_{frm}	35.76°	35.40°	27.78°	29.90°	25.28°	35.40°
Θ_{plm}	36.11°	35.74°	28.13°	30.25°	25.63°	35.74°
$\Delta\Theta_{M1}$	3.89°	2.69°	2.06°	2.06°	2.06°	2.69°
$\Delta\Theta_{M2}$	3.24°	2.25°	1.72°	1.72°	1.72°	2.25°
$\Delta\Theta_{M3}$	-3.24°	-2.25°	-1.72°	-1.72°	-1.72°	-2.25°
$\Delta\Theta_{M4}$	-3.89°	-2.69°	-2.06°	-2.06°	-2.06°	-2.69°
Θ_{M1}	39.99°	38.44°	30.20°	32.31°	27.69°	38.44°
Θ_{M2}	39.35°	37.99°	29.85°	31.97°	27.35°	37.99°
Θ_{M3}	32.86°	33.50°	26.41°	28.53°	23.91°	33.50°
Θ_{M4}	32.22°	33.05°	26.07°	28.18°	23.57°	33.05°

Table 3: Angle between Marker Counter and Beam Line. An error of $\pm$3mm in the measurement results in difference of $\pm 0.01°$. Θ_{plm} refers the the angle between the position of the plumb bob to the beam line, $\Delta\Theta_m$ is the angle between the different Marker Counters to the plumb bob, and Θ_m is the angle between the different Marker Counters to the beam line. Θ_{frame} refers to the angle between the Neutron Arm center and the beam line, which reflects the fact that the plumb bob is off center by .953cm. Θ_{frm_nom} is the nominal angle between the Neutron Arm and the beam line.

5 OTHER APPARATUS OF THE G_E^n EXPERIMENT

This section provides a brief overview of the two other components used during the G_E^n experiment, BigBite and the neutron target.

5.1 BIGBITE

To detect the scattered electrons the experiment employs the use of the BigBite spectrometer detector package, which consists of a large dipole magnet producing a field of up to 1.2 Tesla, three multiple-wire drift chambers (MWDC), a scintillator plane, and two lead-glass calorimeter planes. The use of BigBite allows us to reconstruct tracks and momentum of the scattered electron to a high degree of precision. The high degree of precision in BigBite then allows us to place tight kinematic cuts on the electron vertex. The current configuration allows for a solid angle acceptance of 75msr and a momentum resolution of approximately 1-2% sigma.

BigBite was moved once during the experiment between the first and second kinematic points on 03/09/06, which is between runs 2782 and 2783. Prior to 03/09/06 BigBite was 2.26 meters from the target and at an angle of 56.26° away from the beam line. After 03/09/06 BigBite was 2.26 meters from the target at and angle of 51.20° from the beam line.

The MWDCs allow us to reconstruct the track of the electron through the detector. The MWDCs are made up of 20% Au-80% Be sense wires to minimize sagging as they are strung across the detector. The sense wires have a voltage placed across them. The rest of the volume of the detector is filled with a gas mixture of 50% argon-50% ethane kept at slightly above atmospheric pressure. In between the sense wires are copper wires used for electrostatic field shaping so that the field lines run roughly parallel and horizontal in the region of drift, and thus point from the field wire to the signal wire. The parallel field lines are due to the constant E-field which produces a constant drift velocity.

As a charged particle, e.g. electron, passes through the MWDC it ionizes the gas mixture. Due to the potential difference across the sense wires and the ground planes, the ions accelerate towards the wire generating an electrical signal, which is then read out by a time-to-digital converter. This time can then be converted into a distance across several planes. As the electron passes through the MWDC there is a small dead time involved with the detector due to the ionization of the gas mixture. Thus the gas mixture has to allow for a quick response to the electron and at the same time be able to have a fast recovery time to minimize the dead time. The MWDCs in BigBite have been found to have a dead time of 150μs.

In the BigBite detector package there are 3 MWDCs which are placed right after the dipole magnet. The first and last MWDC consist of six internal planes of wires that are arranged in a horizontal, $+30°$, and $-30°$ pattern and are placed 1cm apart, see figure 12 for clarification. These planes are named U, U′, X, X′, V, and V′ respectively, where the primed planes are shifted up 0.5cm relative to the unprimed planes. Table 4 shows the number of wires used in the different arrangement in the different planes. The second MWDC is much the same as the first and last MWDC except that it only has three internal planes U, X, and V and does not contain any primed planes. Each of the drift chambers are placed approximately 35cm apart from each other.

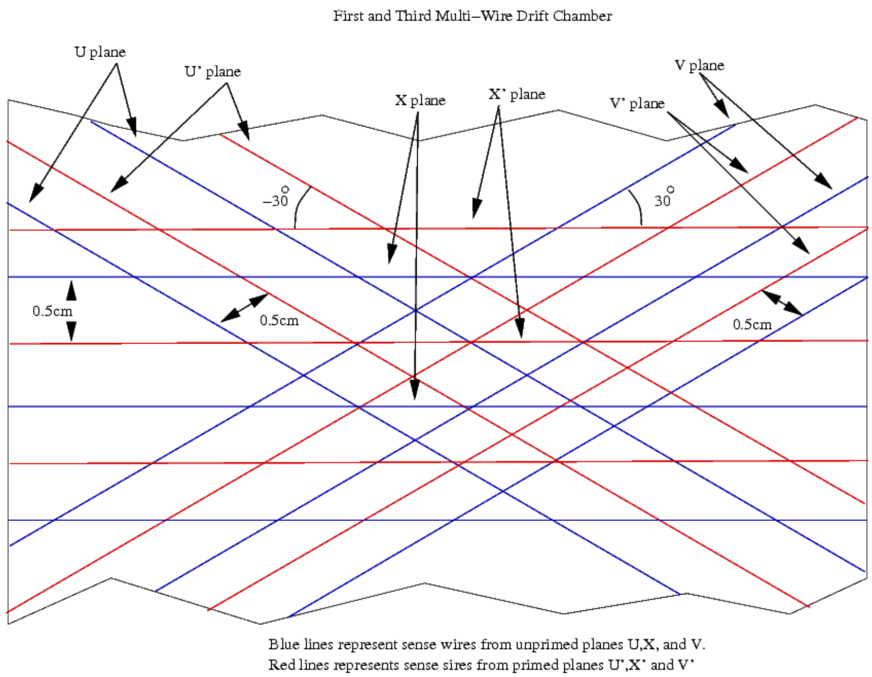

Figure 12: Diagram of first and third MWDC planes

The scintillator and lead-glass calorimeters are placed right after the MWDC and are used to trigger the detector and measure the energy of the electron passing through the MWDC and approximately give the general location of the electron. The scintillator plane is made up of 13 scintillator bars that are 14x60x4cm^3 and are connected to PMTs at both ends, much in the same way as in the Neutron Arm. The scintillator plane serves as a trigger for coincident events in both the Neutron Arm and BigBite. The lead-glass calorimeter consists of a pre-shower and shower counters. The preshower counter contains 54 lead-glass bars of dimensions 8.5x34x8.5cm^3 arranged in a 2x27 array. The shower counter contains 189 lead-glass bars with dimensions of 8.5x8.5x34cm^3 arranged in a 7x27 array.

As an electron enters the calorimeter it begins to radiate through bremsstrahlung

Chamber	Plane Pattern	# of wires	Wire Spacing(cm)	Height(m)	Width(m)	Z Pos.(m)
1	UU′XX′VV′	142	1.0	1.40	0.35	0.00
2	UXV	200	1.0	2.00	0.50	0.36
3	UU′XX′VV′	200	1.0	2.00	0.50	0.71

Table 4: BigBite Layout.

radiation. Bremsstrahlung radiation is electromagnetic radiation arising from scattering of the electron in the electric field of a heavy Z nucleus, e.g. the lead in the calorimeter. The radiation produces a photon, which in turn produces electron-positron pairs, which can then produce more photons thus creating an avalanche or shower effect. The shower will increase until the electrons/positrons can no longer radiate via bremsstrahlung, then energy loss is due mainly to ionization in the lead. The light collected from scintillation of the electron is then readout and digitized by a PMT. The arrangement of the pre-shower and shower counters is used to identifiy the scattered electrons in BigBite and to eliminate spurious tracks and noise that occurs in the MWDCs thus cutting down background electrons, and enhancing the MWDC's ability to recreate electron tracks.

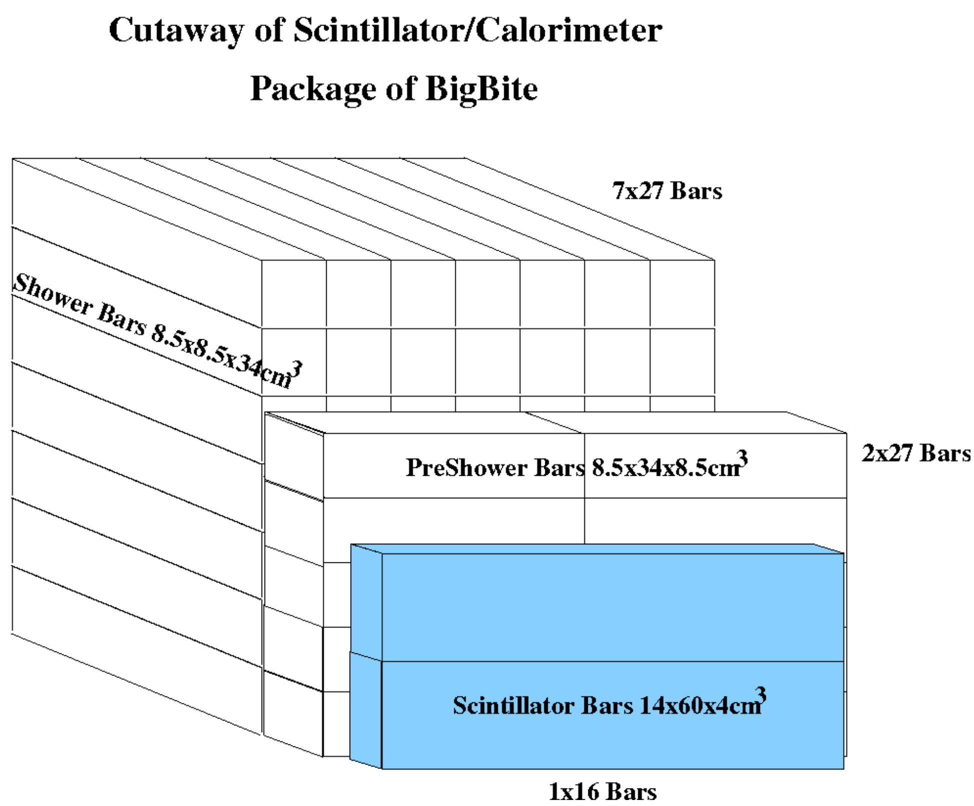

Figure 13: Diagram of Calorimeter package of BigBite.

Plane	x(cm)	y(cm)	z(cm)	Arrangement
Scintillator	14.0	60.0	4.0	1x13
Pre Shower	8.5	34.0	8.5	2x27
Shower	8.5	8.5	34.0	7x27

Table 5: Calorimeter Layout

As stated before, one of the difficulties in measuring the form factor of the neutron is the fact that there are no free neutron targets with sufficient luminosity. As a substitute for the lack of a free neutron target, we use ^{3}He, since at sufficient energy transfer the neutron is considered almost free. In polarizing the target we use the fact that the spin of an electron can be imparted to the nucleus of the ^{3}He. The neutron of the ^{3}He contains roughly 90% of the nuclear spin, since the proton spins will cancel each other out 90% of the time, giving us a quasi-free polarized neutron target.

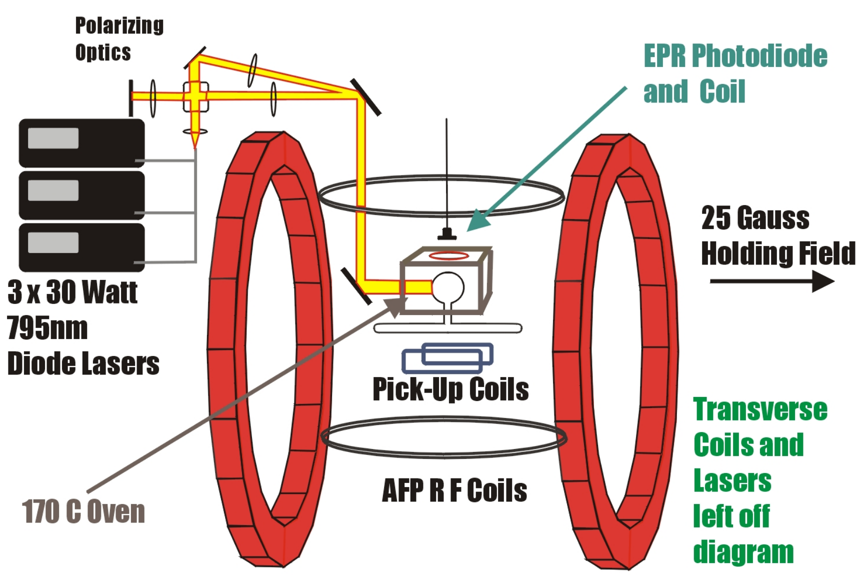

Figure 14: Target Cell Diagram courtesy of Aidan Kelleher

The polarization of the ^{3}He target is based on the technique of spin-exchange optical pumping (SEOP). In the G_E^n experiment, an alkali-metal mixture of rubidium (Rb) and potassium (K) was placed in a magnetic field and heated to 250C in order to obtain enough Rb vapor to polarize the ^{3}He cell. Once the Rb is in its vapor form it can be polarized by optical pumping using circularly polarized light from a laser, which excites the $5S_{1/2} \rightarrow 5P_{1/2}$ transition in the Rb. In a magnetic field, the outer electron of a Rb atom can be in one of two states, either aligned or anti-aligned with the magnetic field. To get the all of the electrons of Rb to the state that we want, say aligned with the magnetic field, we shine circularly polarized light of a particular frequency onto the vapor and excite the atoms in the state that we do not want, the anti-aligned state. Due to the presence of the N_2 the electron can decay into either an aligned or anti-aligned state, see figure 15 for further clarifications. Repeatedly exciting only the states of the electron that we do not want and allowing them to decay into a state that we do want allows us quickly to polarize all the electrons into a state we want. The polarized Rb atoms then collide with the ^{3}He atoms, transferring their spin to the ^{3}He nuclei through the hyperfine interaction. From the polarization chart figure 16 of the polarization of the target it can be seen that polarizations of up to 50% were achieved with the ^{3}He target.

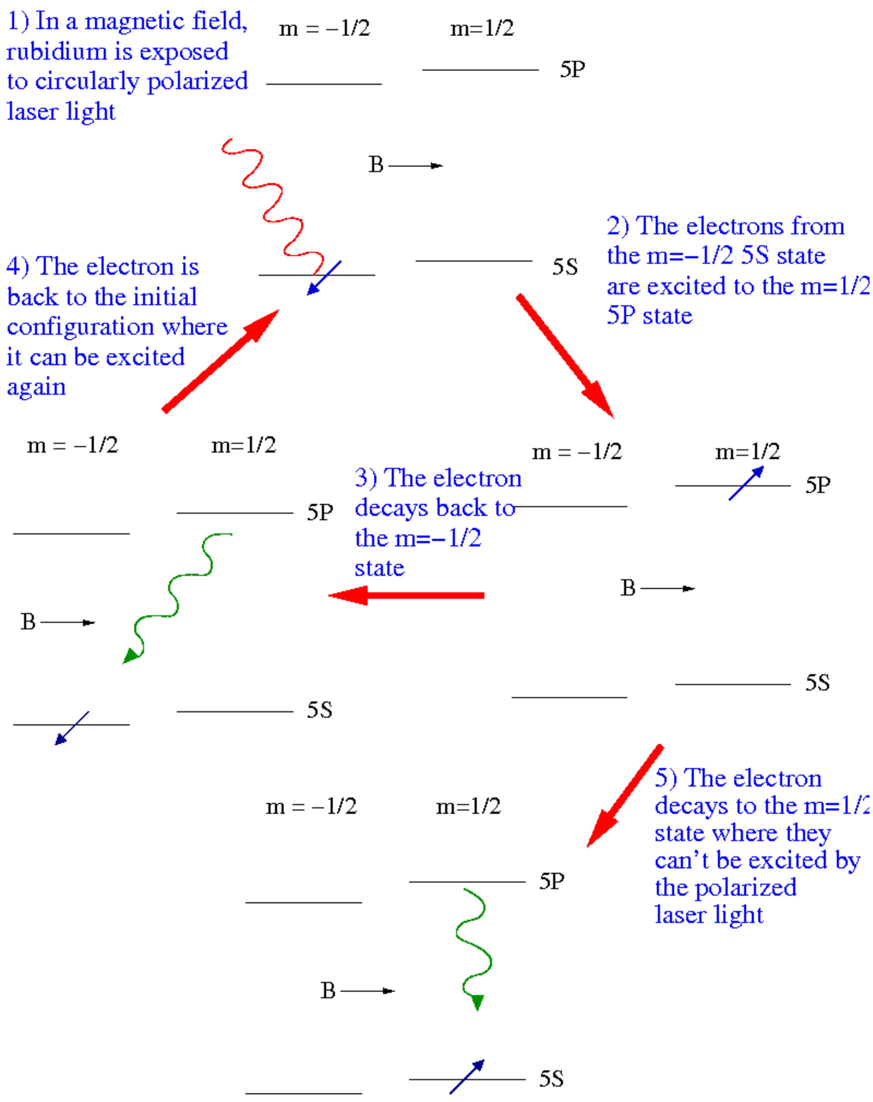

Figure 15: Level diagram for transition states of target, courtesy of Aidan Kelleher

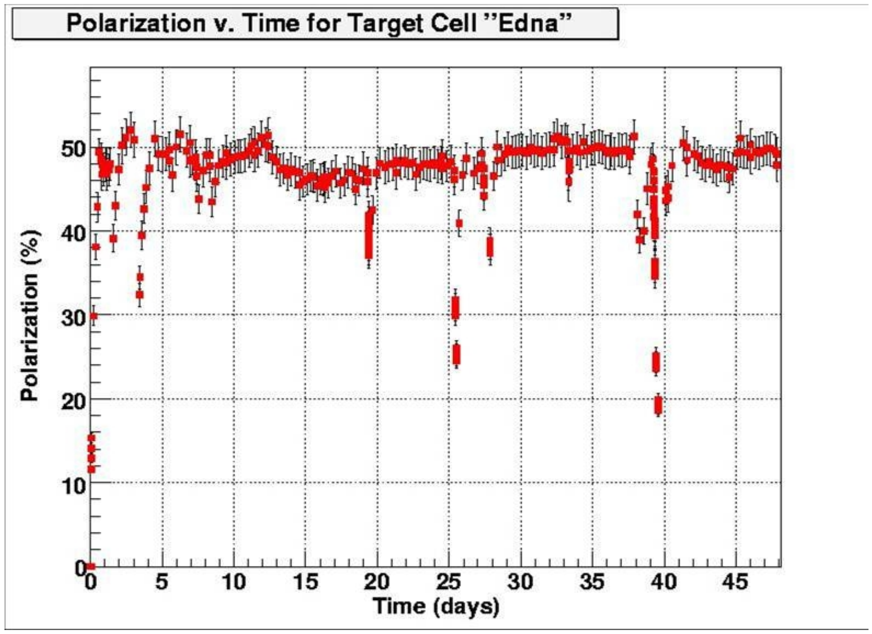

Figure 16: Target Cell Edna used for kinematics 3 and 4, courtesy of Aidan Kelleher

To measure the amount of target polarization we use two methods of polarimetry, adiabatic fast passage nuclear magnetic resonance (AFP NMR), where AFP is a method of flipping the spin of the polarized ^{3}He gas, and electron paramagnetic resonance (EPR). In AFP NMR an external magnetic field is applied at the Larmor frequency of the ^{3}He. We then sweep the magnetic field of the target through this resonant field. At resonance, the nuclei spins flip over and produce an EMF signal that is proportional to the polarization of the ^{3}He gas. The spin reversal has to be performed slowly enough so that it is adiabatic and fast enough that the spins do not have time to relax. The method of EPR on the other hand uses light from the target cells' Rb as a precise magnetometer to measure the small changes in the magnitude of the magnetic field due to the polarized ^{3}He. Since the small shift due to the magnetization of the ^{3}He depends on the direction of the ^{3}He spin we can isolate this shift by changing the direction of the spins while keeping everything constant using the AFP technique. We then can measure the change in the frequency emitted from the Rb before the flip and after the flip of the spin. The change can then be related to the polarization of the ^{3}He by equation 20 [14]

$$\Delta\nu_{EPR} = \frac{8\pi}{3}\frac{d\nu_{EPR}(F,M)}{dB}\kappa_0\mu_{He}P_{He}. \tag{20}$$

6 EVENT DISPLAY

Use of the event display, which I created, allows one to look at individual events to see how the particles propagate through the different detectors. These event displays, although only providing low statistics since each event has to be inspected visually, were instrumental in allowing me to see the types of cut that could be placed on various types of events, whether it be cosmic muons, protons or neutrons. Figures 17, 18, and 19 are examples of the event displays created to evaluate different events in a run. Here I used event 1455 in run 4425, for example.

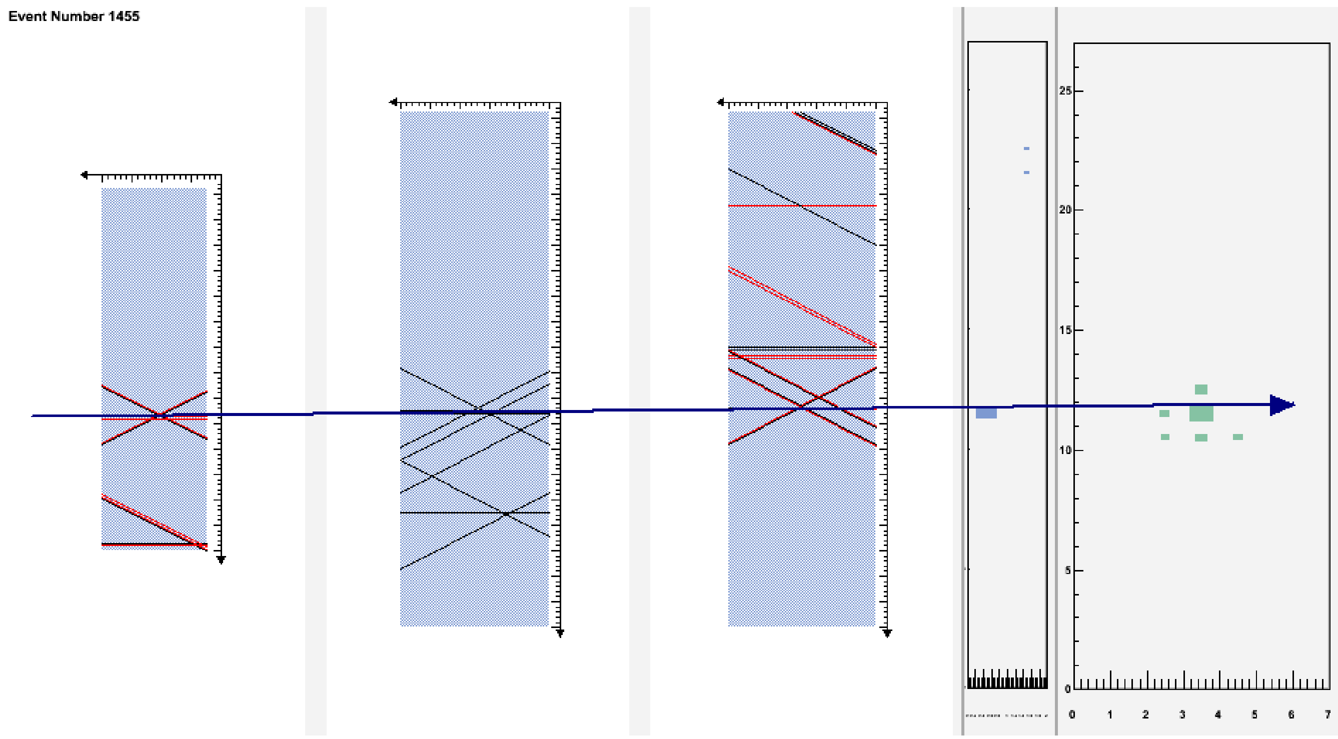

Figure 17: Event display of BigBite shown with the three planes of MWDC, pre-shower, and shower counters

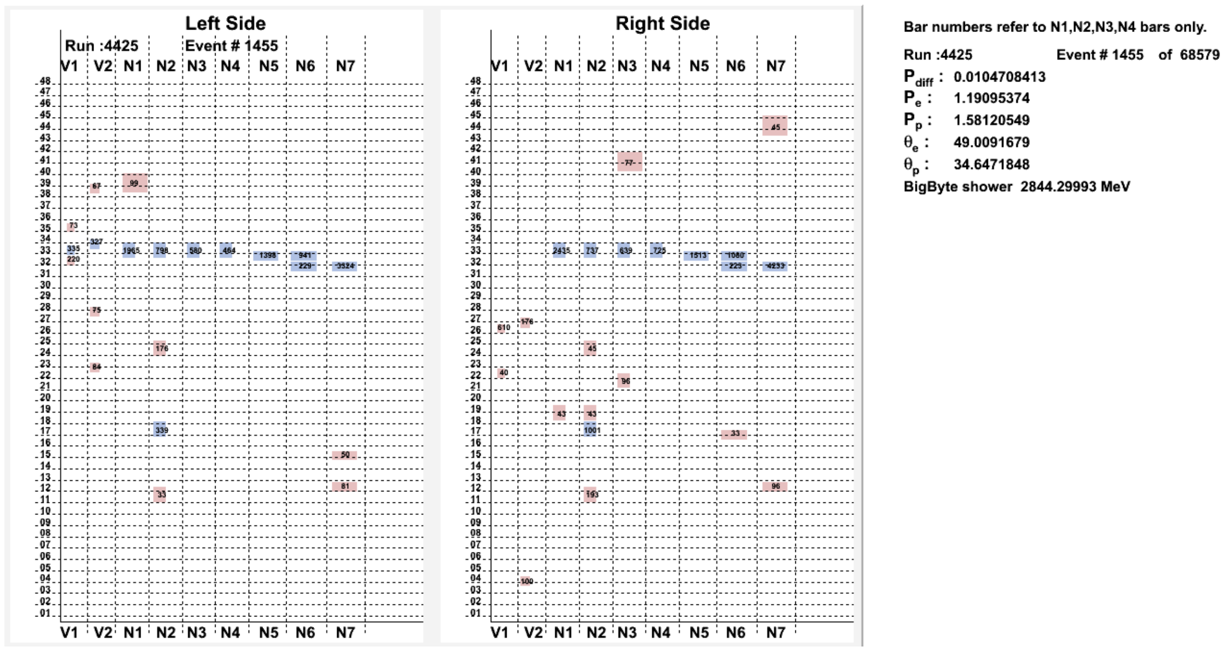

Figure 18: Event display of the Neutron Arm shown with statistics screen. The y-axis represents bar numbers of the V1 plane and the x-axis represents the planes of the Neutron Arm.

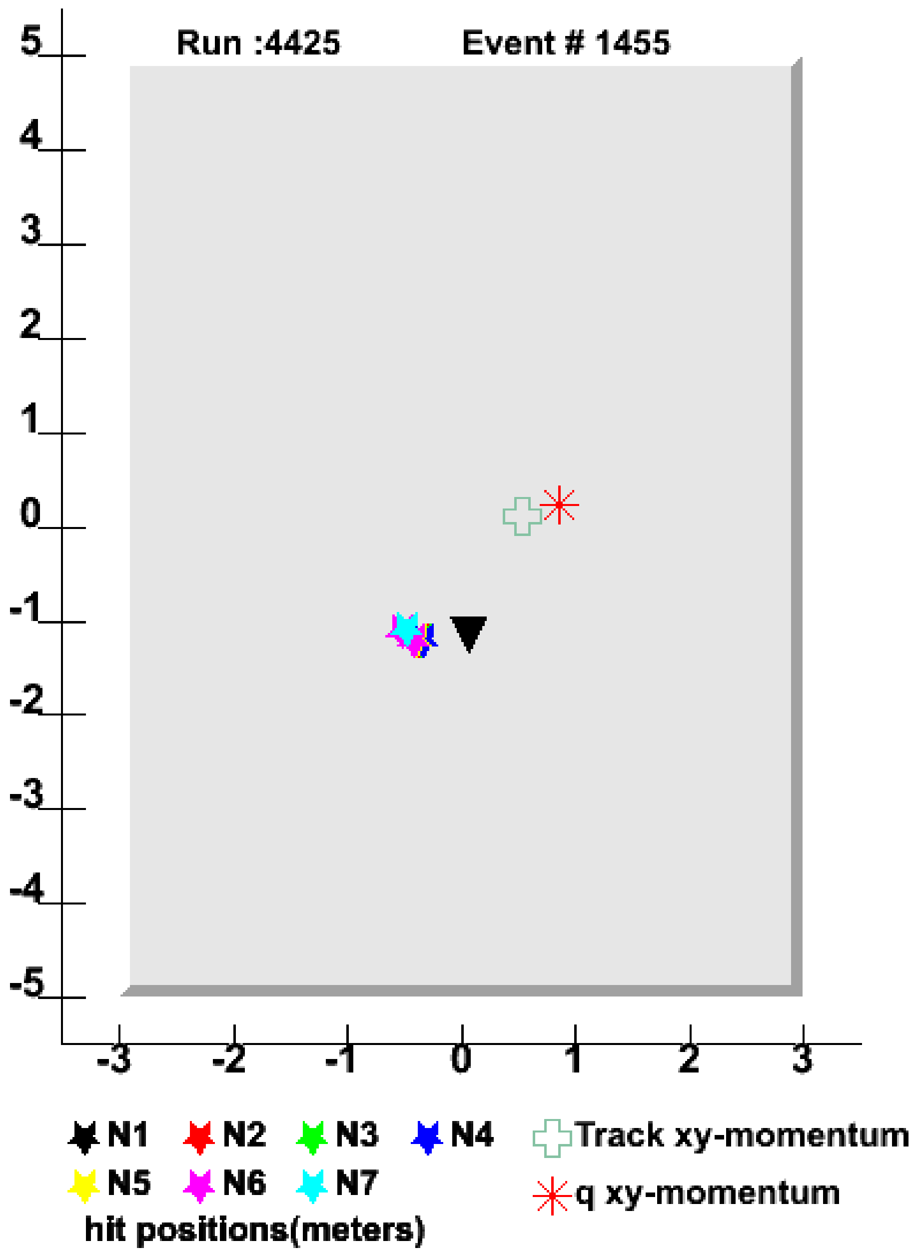

Figure 19: Event display of the showing front view of the Neutron Arm

7 ENERGY CALIBRATION

Energy calibrations of the Neutron Arm were done using cosmic data during the experimental run and will allow us to associate the ADC channel output from the PMT to an energy value. The benefit of using cosmic muons is that they can be considered as minimum ionizing particles(MIP), and thus will leave a constant amount of energy per unit length as they pass through matter. For the scintillator bars that were used in the Neutron Arm cosmic muons will deposit about 2 MeV of energy per centimeter of scintillator that they pass through. Typically a muon will pass through the top of the detector stack and propagate through multiple bars in one plane.

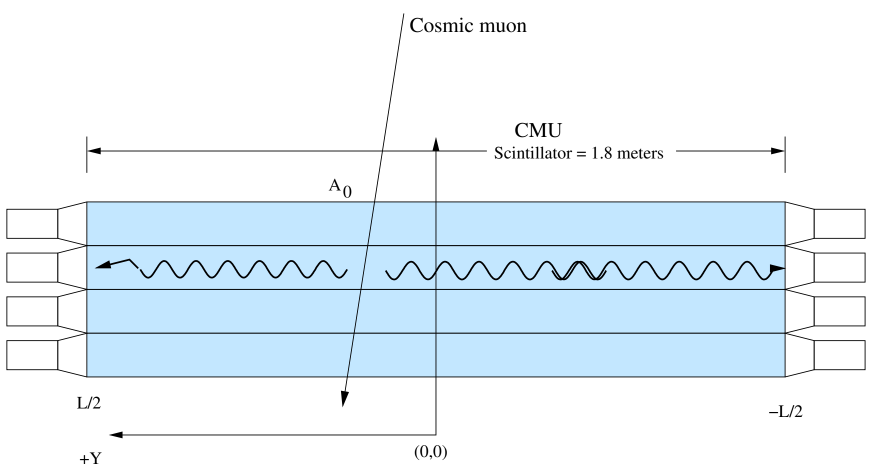

Figure 20: Scintillator bar in N1 plane

7.1 EVENT SELECTION CRITERIA FOR COSMICS

To calibrate using cosmic muons, cuts are placed on events so that we are sure that the events are cosmic muons and that they propagate in a straight line going through any plane of the Neutron Arm. Cuts placed on cosmic data were such that five or more bars were hit in consecutive order, both left and right PMTs fired, and through cuts on the y-position so that the muon is going vertically from top to bottom of the detector. In any of these events, say if seven bars were hit in the N1 plane, the first and last bar hit are not used in the statistics, since we can not be sure of the track position using a previous bar and a bar after. Bars at the very top and bottom of the detector will generally have larger errors since we will not be able to check where the event is coming from. Refer to figure 21 for further clarification.

7.2 ATTENUATION FACTOR

Once we have a hit we then look to the PMT signal. The effect of the attenuation on the incident signal in general is described in equations 21 and 22. A_L and A_R are the amplitudes outputted by the left and right PMTs, A_0 is the incident amplitude, G_L and G_R are the gain factors for the PMTs and Γ is the attenuation length. The gain factors will divide out to give us an energy value.

$$A_L = G_L A_0 exp\left(-\frac{\frac{L}{2} - y}{\Gamma}\right) \tag{21}$$

$$A_R = G_R A_0 exp\left(-\frac{L/2 + y}{\Gamma}\right) \tag{22}$$

Dividing the two equations we have:

$$\frac{A_L}{A_R} = \frac{G_L}{G_R} exp\left(\frac{2y}{\Gamma}\right) \tag{23}$$

$$\frac{2y}{\Gamma} = ln\left(\frac{A_L}{A_R}\right) - ln\left(\frac{G_L}{G_R}\right) \tag{24}$$

The plots here reflect that the attenuation length is 2/slope for bars 13 and 14 in the N1 plane. The gain ratio is then obtained from the y-intercept.

In figure 24 plots the attenuation factor of all the bars using cosmics run 4490. A

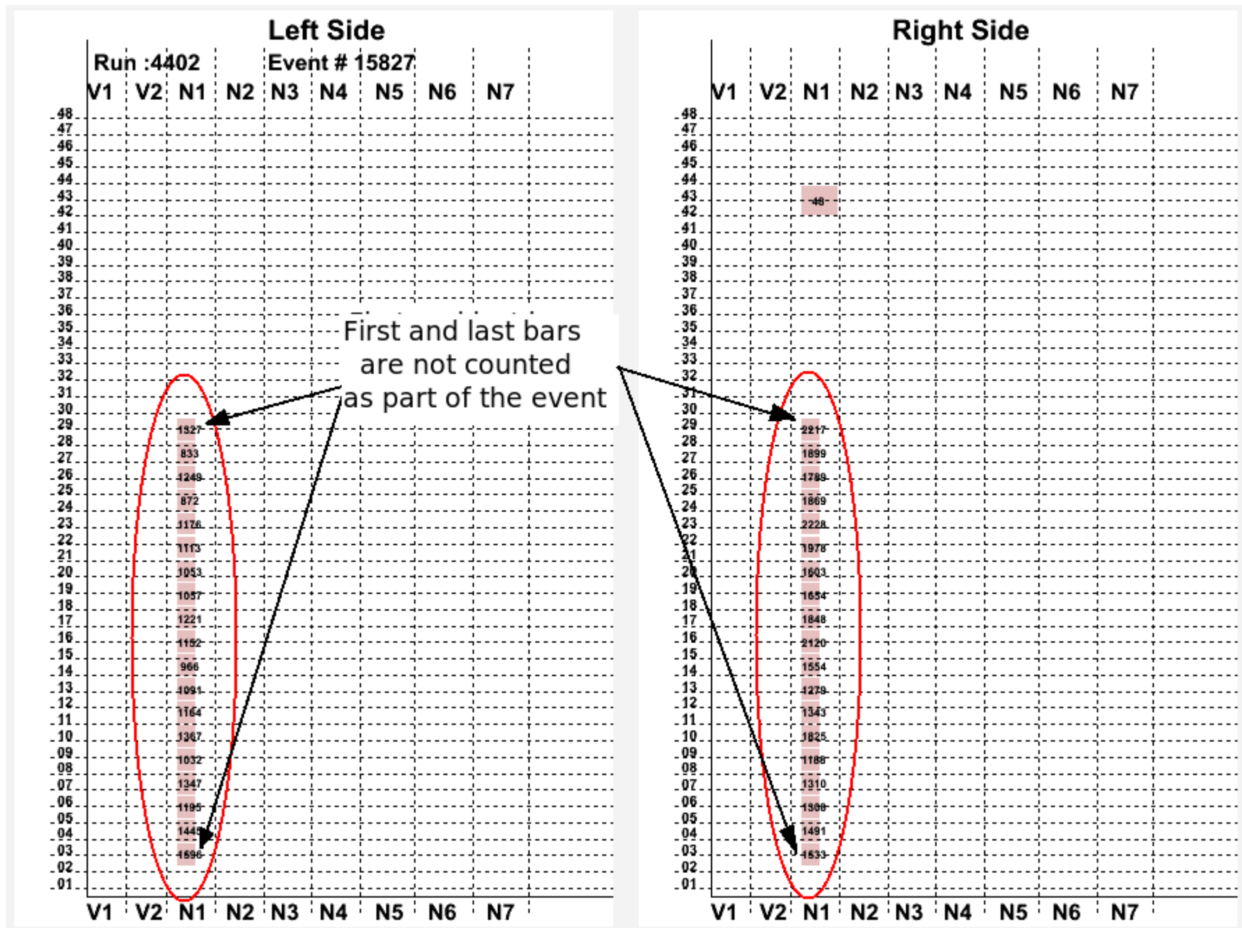

Figure 21: Event Display of a Cosmic Track. The y-axis represents bar numbers of the V1 plane and the x-axis represents the planes of the Neutron Arm.

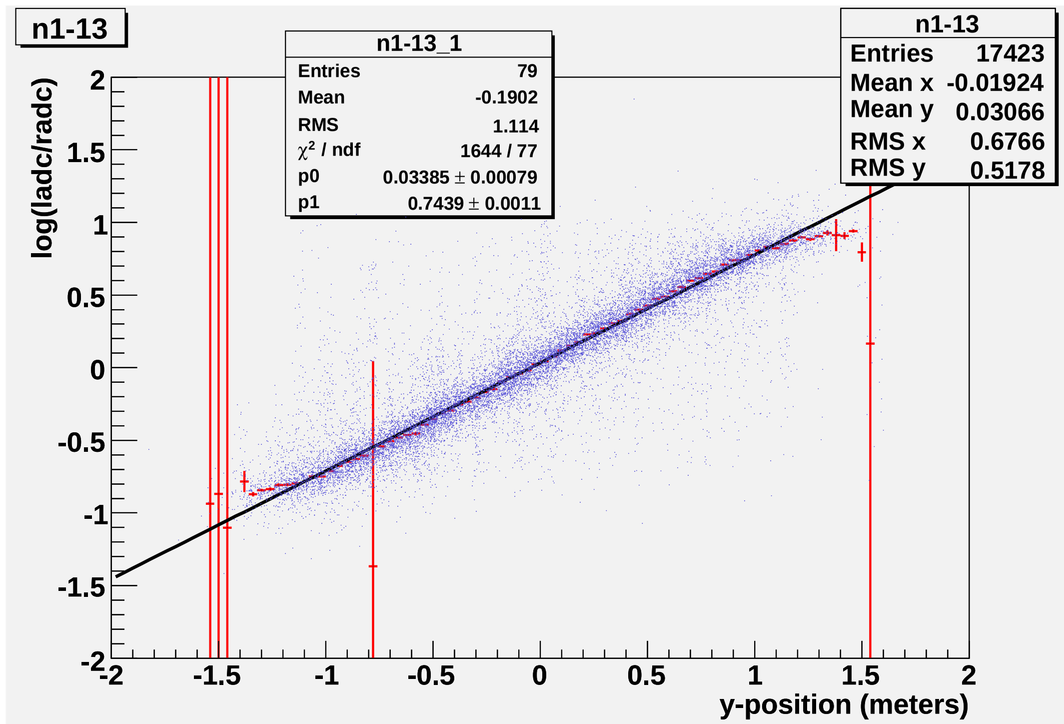

Figure 22: A plot of $ln\left(\frac{A_L}{A_R}\right)$ vs. y-position

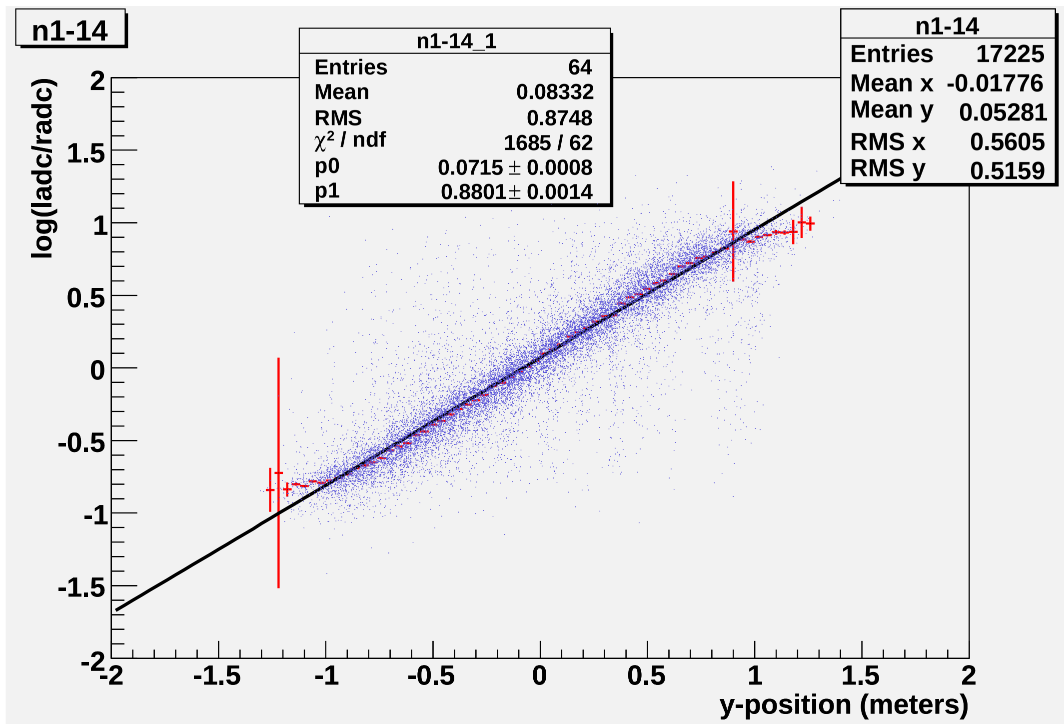

Figure 23: A plot of $ln\left(\frac{A_L}{A_R}\right)$ vs. y-position

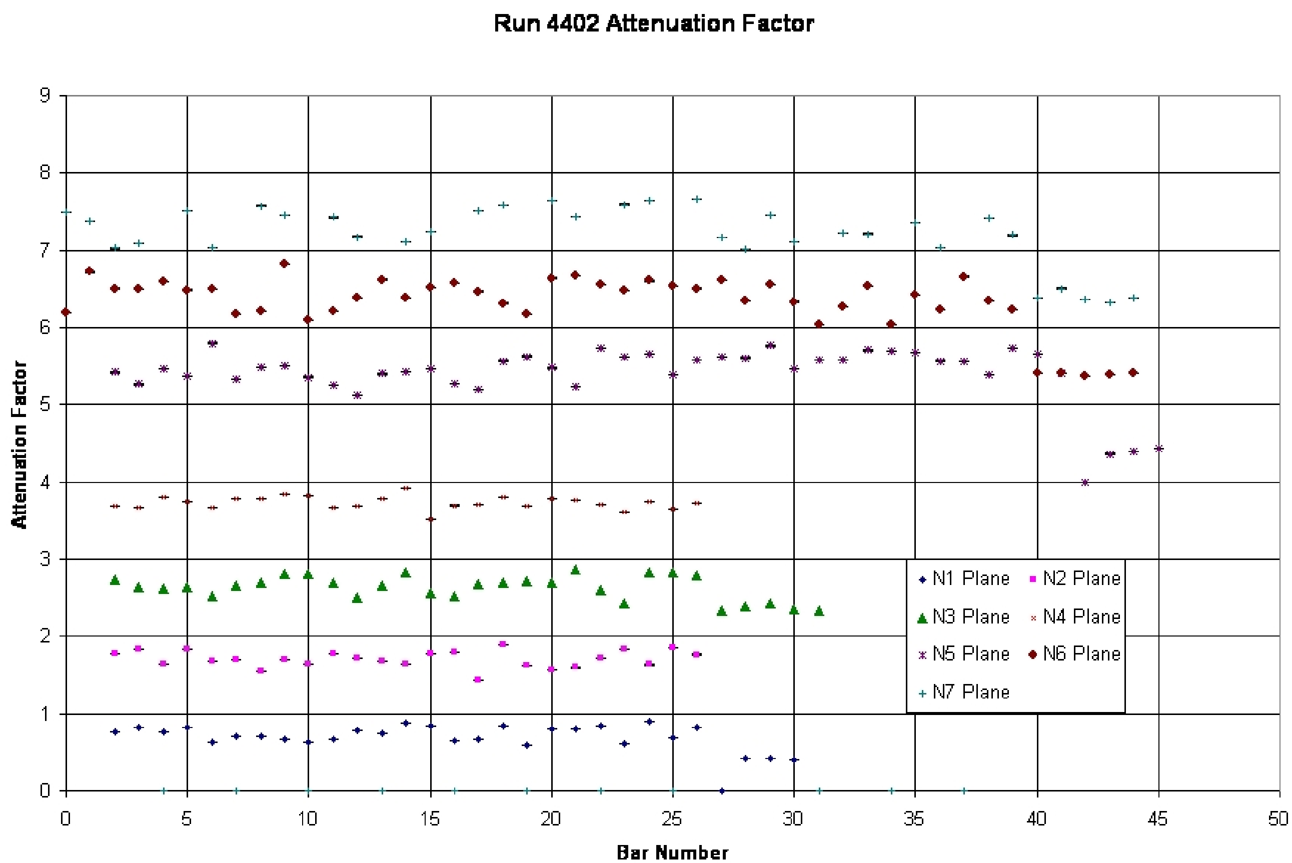

Figure 24: Plot of attenuation factors for all the bars in the Neutron All

constant is added to clarification purposes, for example a constant value of 1 added to all the bars in the N2 plane, a constant value of 2 is added to the bars in plane N3, and so on.

7.3 INCIDENT AMPLITUDE

The plot of the incident amplitude A_0 for a 2 MeV/cm MIP is shown in the figure 25 and 26. Now multiplying equation 21 and equation 22 gives,

$$A_L A_R = G_L G_R A_0^2 exp\left(-\frac{L}{\Gamma}\right) \tag{25}$$

$$A_0\sqrt{G_L G_R} = \frac{\sqrt{A_L A_R}}{exp\left(-\frac{L}{2\Gamma}\right)} \tag{26}$$

Then dividing A_0 through by the length the muon travels through the scintillator, L_{muon}, to remove the dependence of the path the muon takes through the scintillator, and by 2 MeV/cm, the energy the muons deposits per centimeter, gives us a value, A_{unit}, that correlates ADC channels readout by the PMT to and energy value MeV.

$$A_{unit} = \frac{A_0\sqrt{G_L G_R}}{2L_{muon}} \tag{27}$$

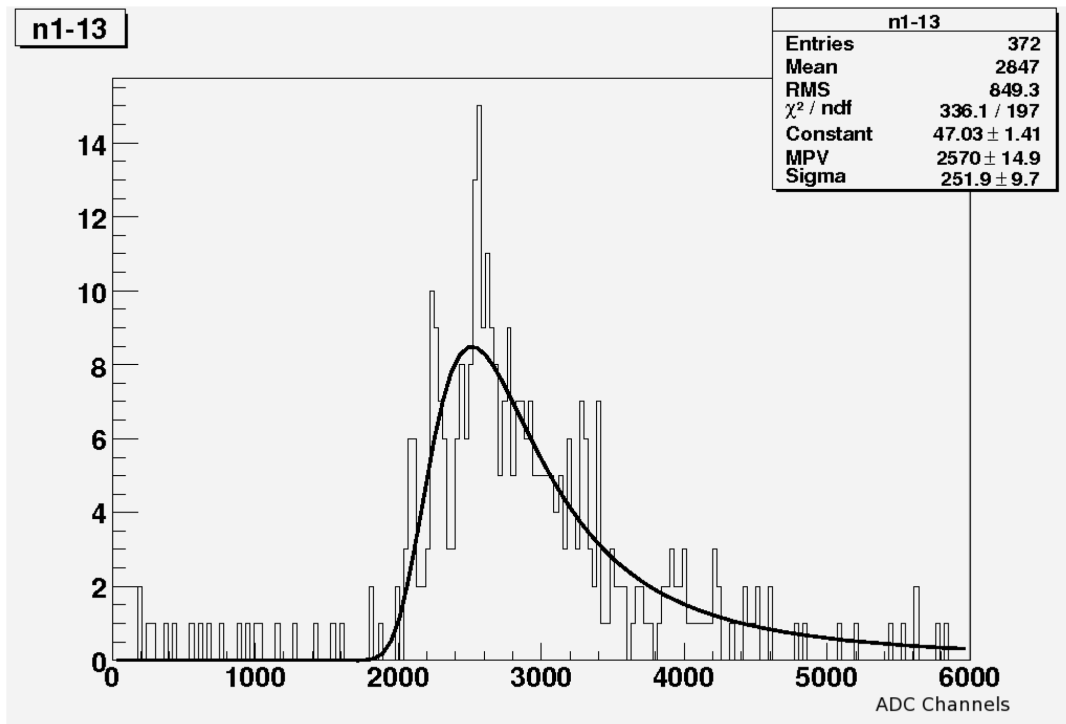

Figure 25: Plot of A_0 for plane N1 bar 13

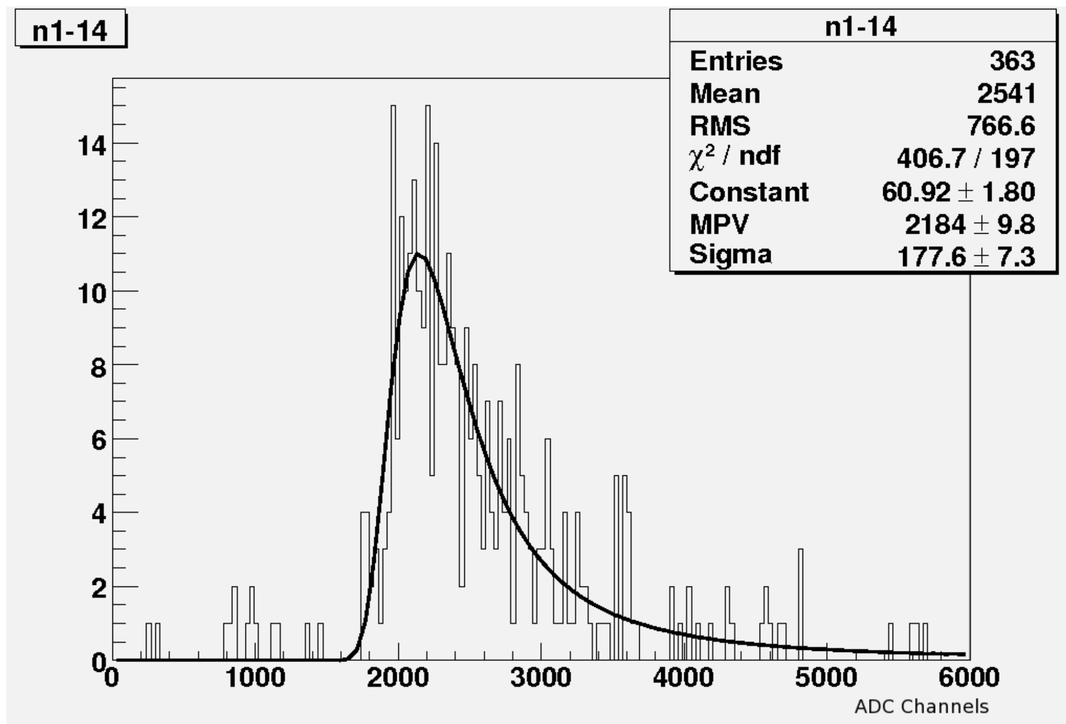

Figure 26: Plot of A_0 for plane N1 bar 14

7.4 PMT STABILITY

By looking at the stability of the scintillators and PMT we ensure the PMTs readouts were not drifting, which would result in different readings at different points of a kinematic run. In figures 27 through 33 the stability of the PMTs is measured by comparing a cosmic run from the beginning of kinematic 4, run 4402, to a cosmic run at the end of kinematic 4, run 4525. The values here represent A_{unit}, or response of the PMT in ADC channels per every one MeV deposited by the cosmic muon. These values for the different bars varies at most by 5% from cosmic runs at the beginning to the end of kinematic 4. Bars at the top and bottom of planes N1 through N7 have larger error bars due to limited statistics. In plane N7 some PMTs were off thus there are fewer points on the plot.

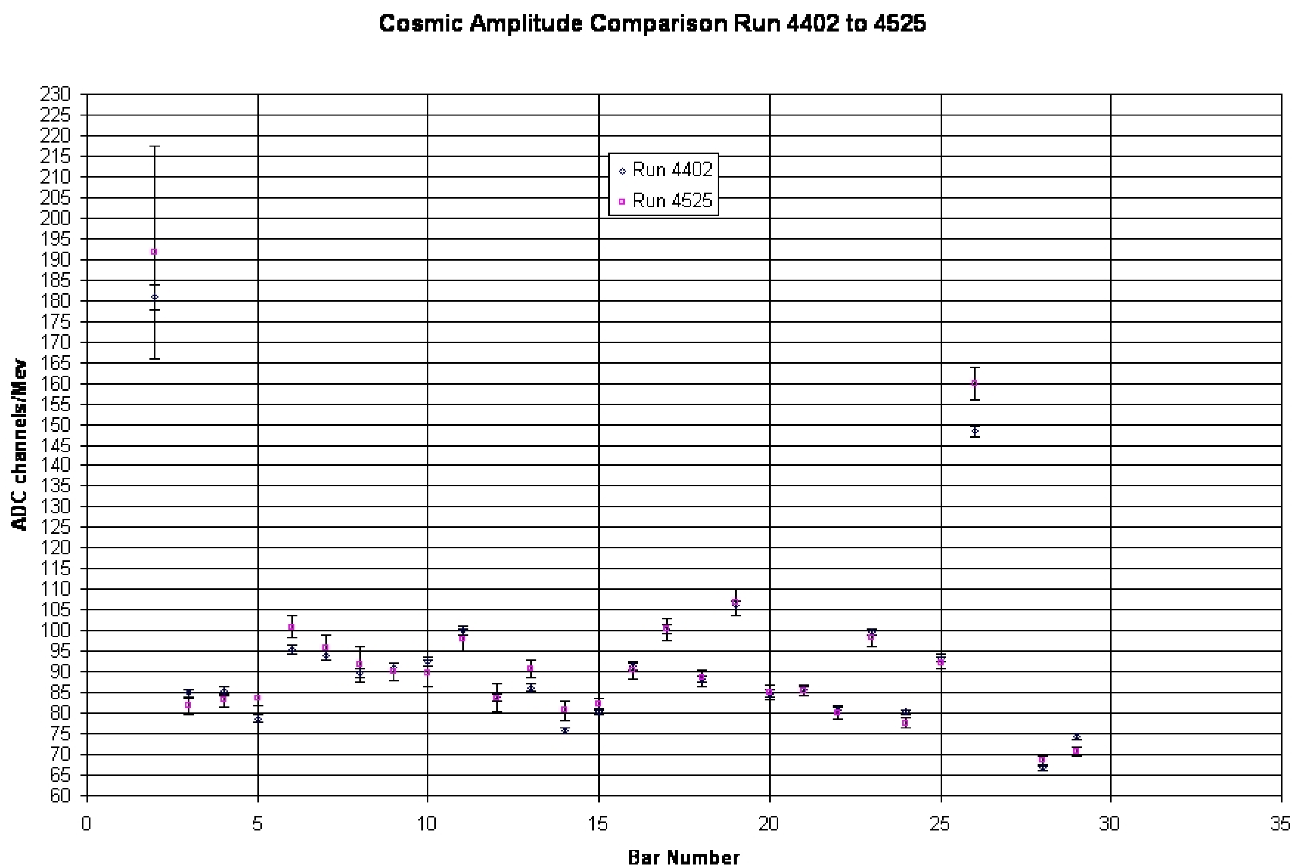

Figure 27: Plane N1 PMT ADC channels/MeV

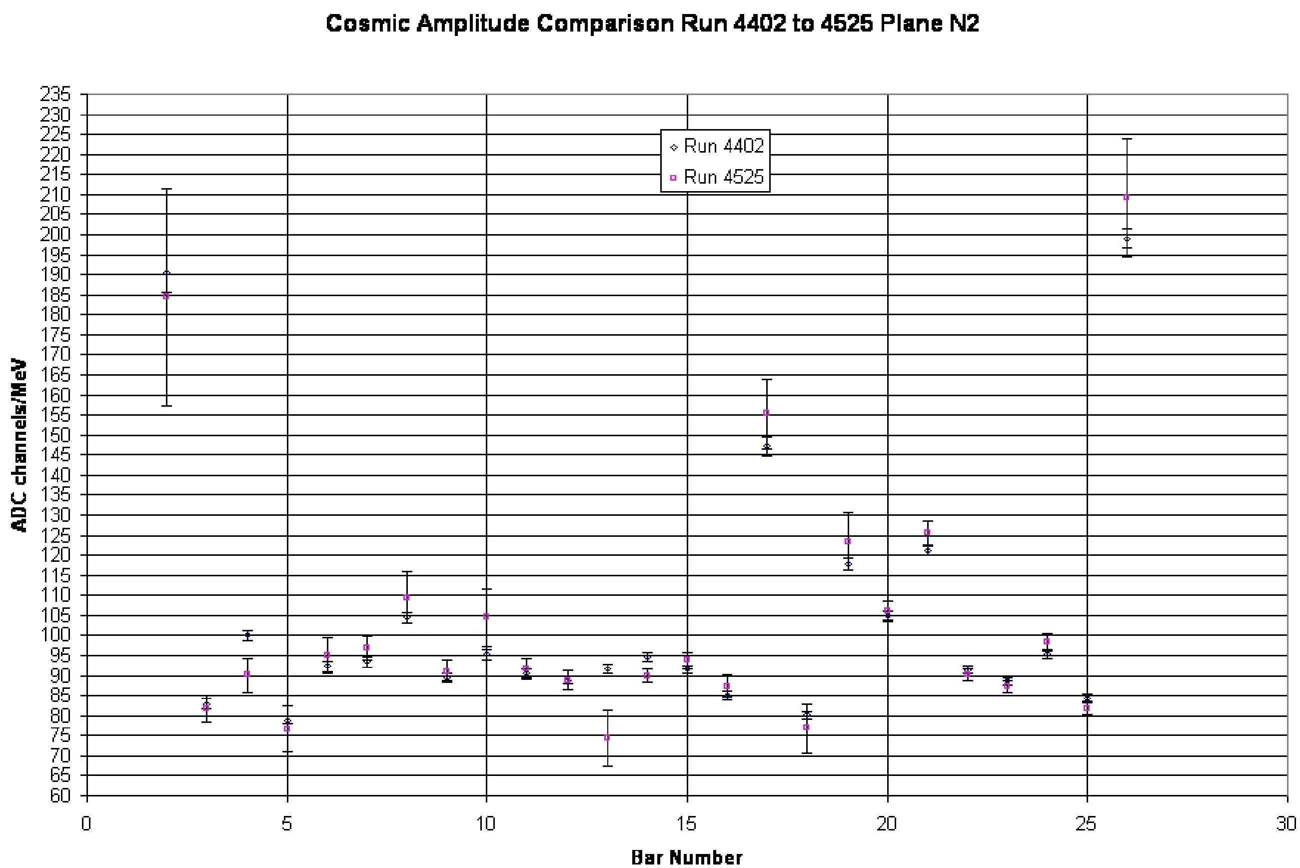

Figure 28: Plane N2 PMT ADC channels/MeV

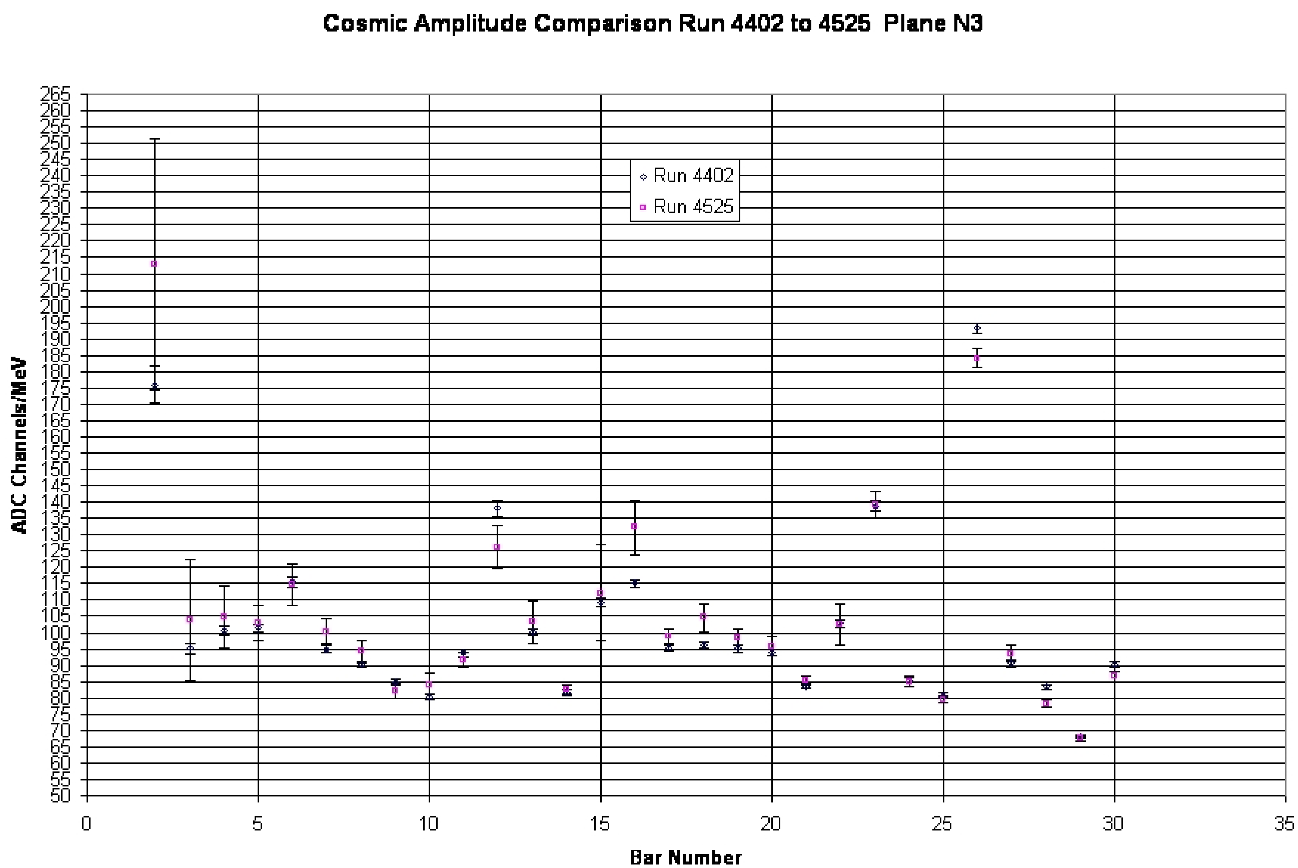

Figure 29: Plane N3 PMT ADC channels/MeV

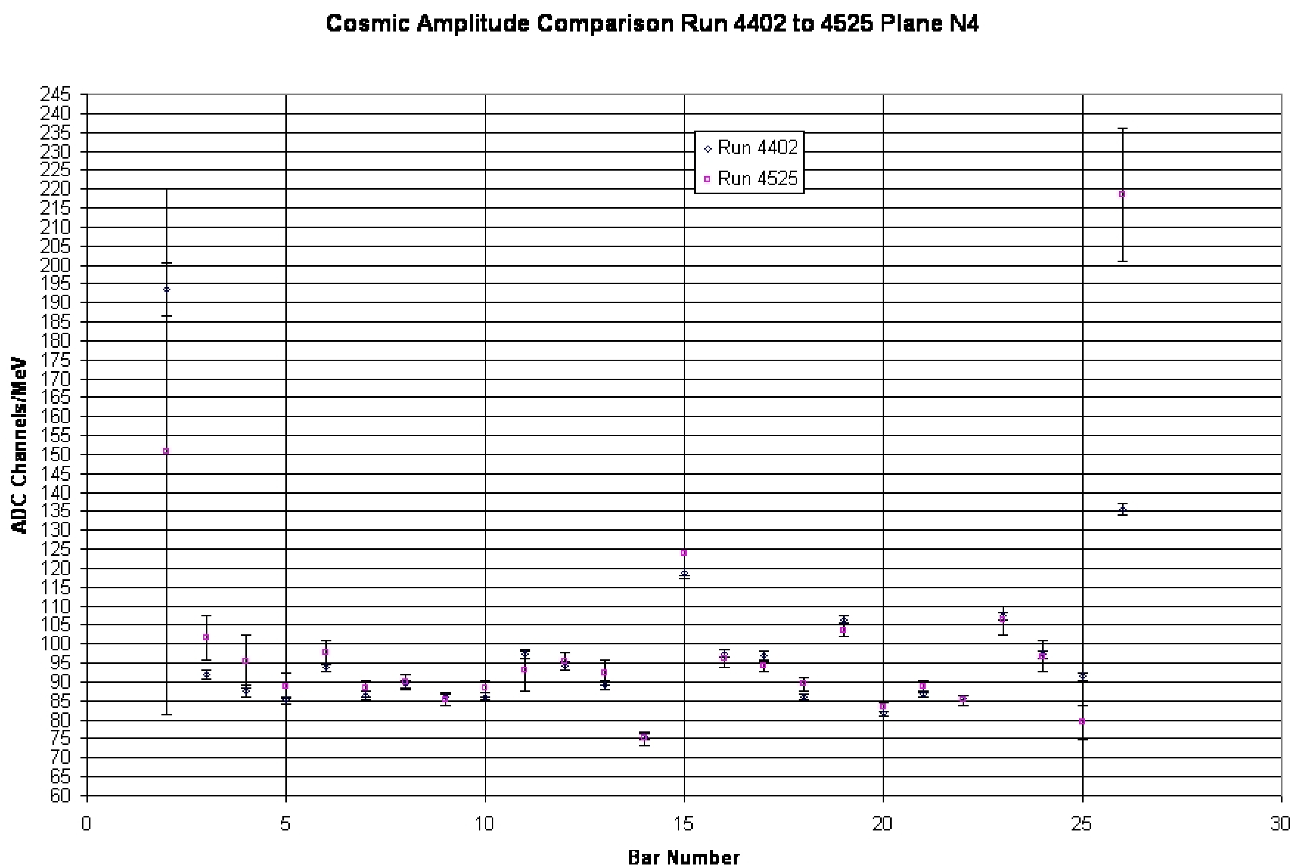

Figure 30: Plane N4 PMT ADC channels/MeV

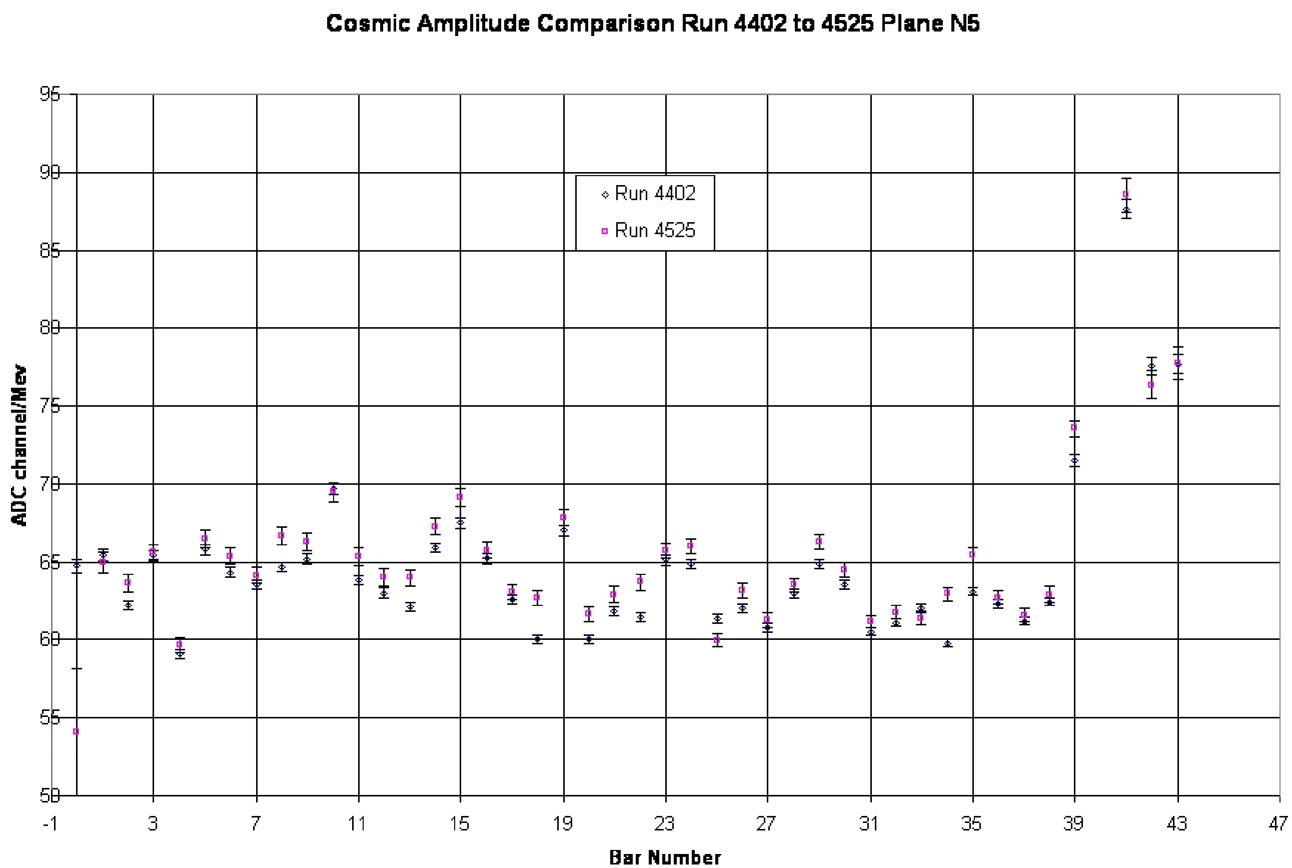

Figure 31: Plane N5 PMT ADC channels/MeV

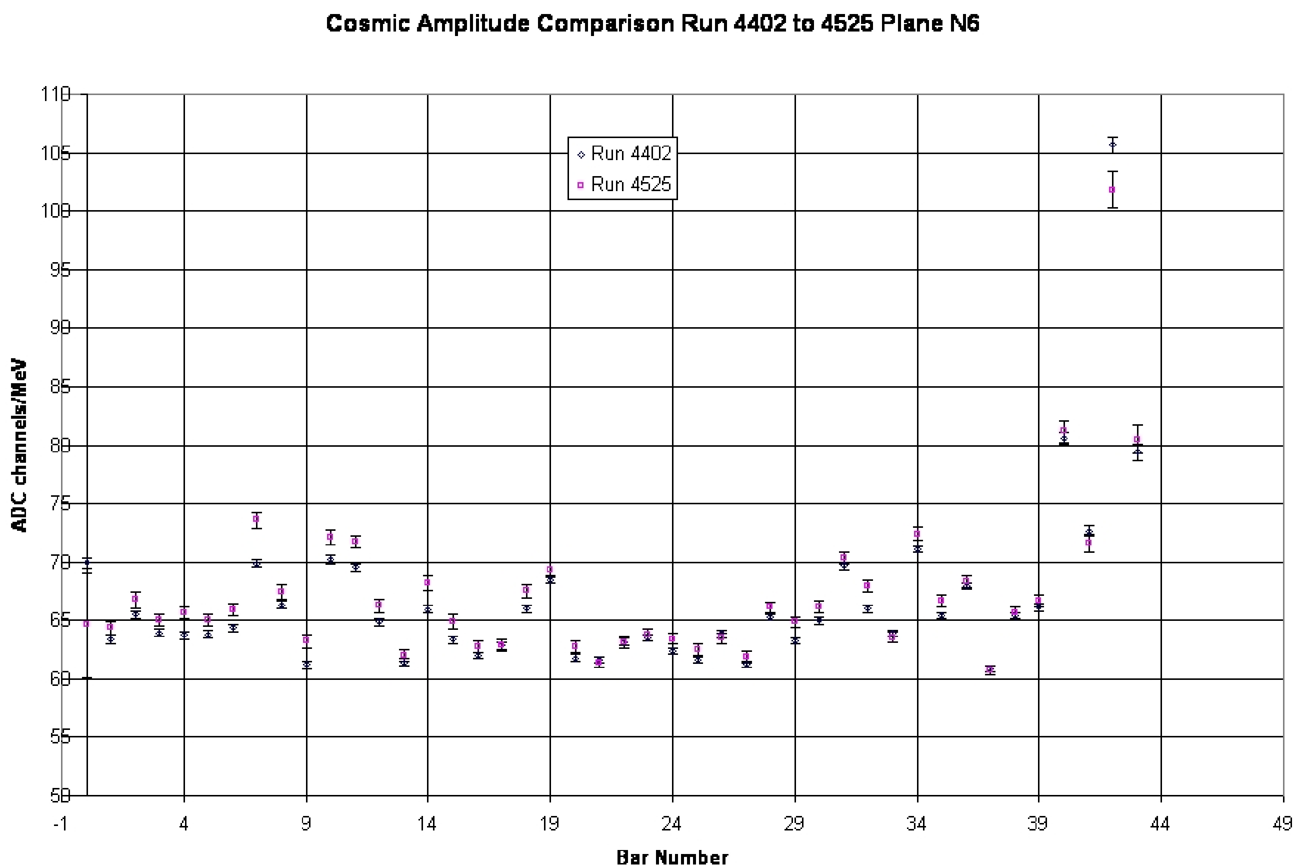

Figure 32: Plane N6 PMT ADC channels/MeV

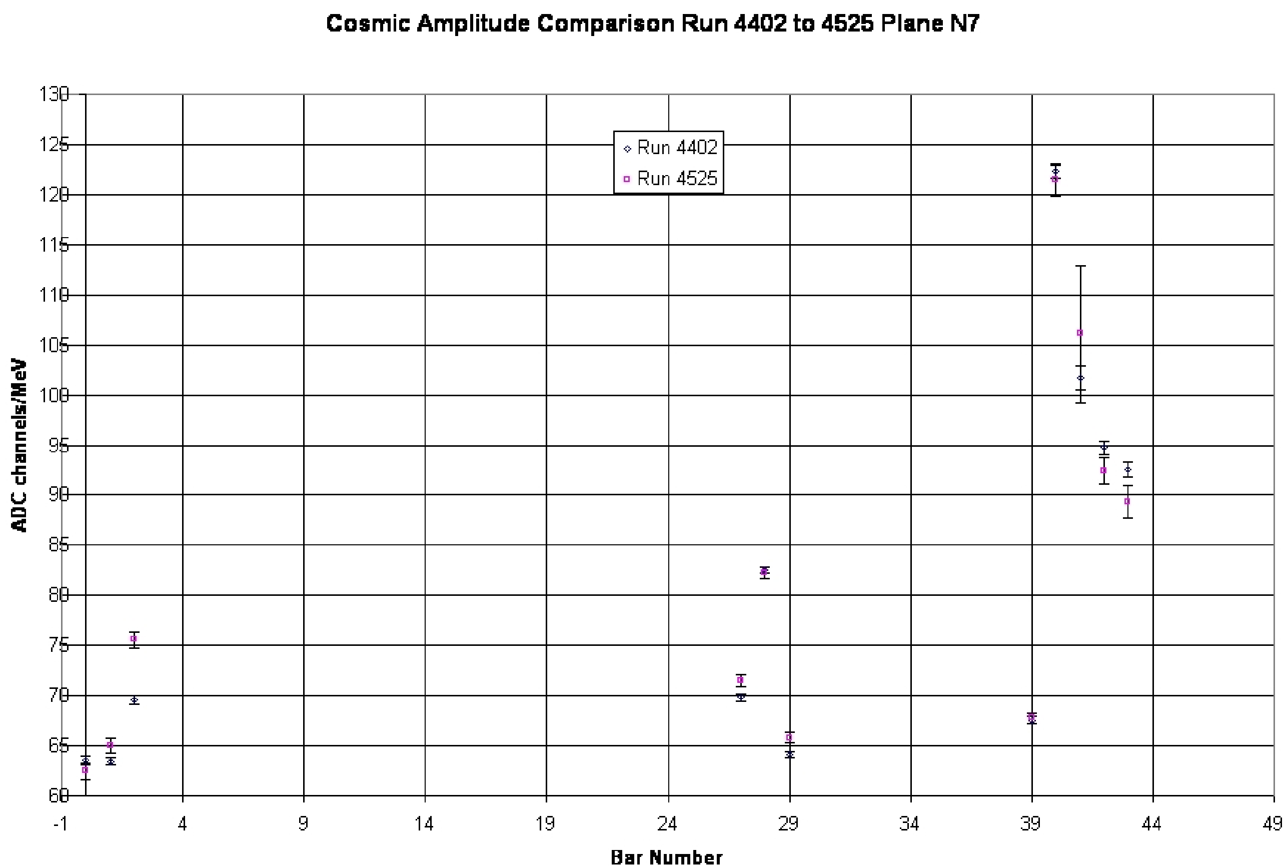

Figure 33: Plane N7 PMT ADC channels/MeV

8 TIMING CALIBRATIONS

Timing calibrations on the Neutron Detector will allow us to understand the time it takes a proton/neutron to propagate to each plane of the detector from the target. This is important since neutrons will not fire the scintillators until they knock out a charged particle in the conversion material. Knowing an expected time a neutron will pass through any plane in the Neutron Arm will allow us to place tighter timing cuts on the neutrons traversing through the Neutron Arm.

Since this will be the first time the Neutron Arm will be used in an experiment at Jefferson Laboratory, a method of obtaining timing calibrations will have to be created. What I present in the following sections is the method that I created in an attempt to calibrate the timing offsets for the Neutron Arm. The technique is to use protons that traverse through at least four planes of the Neutron Arm in a linear fashion, much like what was done with cosmics muons but in the horizontal direction. Although selecting only proton events that have straight and deep penetrating tracks limits the amount of statistics in one run, I chain about five runs together to generate enough statistics in order to calibrate the timing for the Neutron Arm.

8.1 EVENT SELECTION CRITERIA FOR PROTONS

To do a timing calibration we will consider long tracks created by protons since only charged particles will cause the scintillators to fire allowing the event to be recorded. A long track is considered to be any event where the protons will hit at least the first four planes of the Neutron Arm, N1 through N4, and hit the same corresponding scintillator bars in these four planes, i.e. bars 15 in planes N1 through N4 would have to register a hit.

Once we have a hit in the first four planes we then look to see if a veto counter fires in the region where the long track occurred, thus limiting the events to protons.

If there happen to be hits in the N5, N6, and N7 planes, the script then checks to see if the hits are within three scintillator bars of the original track. The scintillator bars in the N5, N6 and N7 plane are not the same size as those in planes N1 through N4, thus we have to allow a gap of three bars to be able to select the continuing track through N5, N6, and N7.

Using these types of events we will be able to record a time that it takes the proton to travel from one plane to another, or intraplane time difference. The diagram in figure 34 depicts what is meant by intraplane time difference. For these events we also will have a time of flight (TOF) from the target to the N1 plane using a coincidence time provided by BigBite's trigger.

8.2 HYDROGEN DATA

Using hydrogen data from kinematic 4 we can place cuts on the momentum of the electron detected by BigBite. The electron momentum detected by BigBite is compared to the calculated momentum of the scattered electron from elastic electron-proton scattering given by,

$$P_{elec_{calc}} = \frac{E_i m_{proton}}{m_{proton} + E_i(1 - cos\theta_{electron})}, \tag{28}$$

where m_{proton} is the mass of the proton, E_i is the energy of the incident electron beam, and $\theta_{electron}$ is the angle of the scattered electron detected in BigBite with respect to the z-direction in BigBite. Subtracting the two momenta we get a value which we refer to as Pdiff which should be zero for elastic events. Also placing cuts on the missing mass around the region of the proton helps to ensure we are selecting only protons. For hydrogen data we place the cut on Pdiff at, Pdiff>-0.04

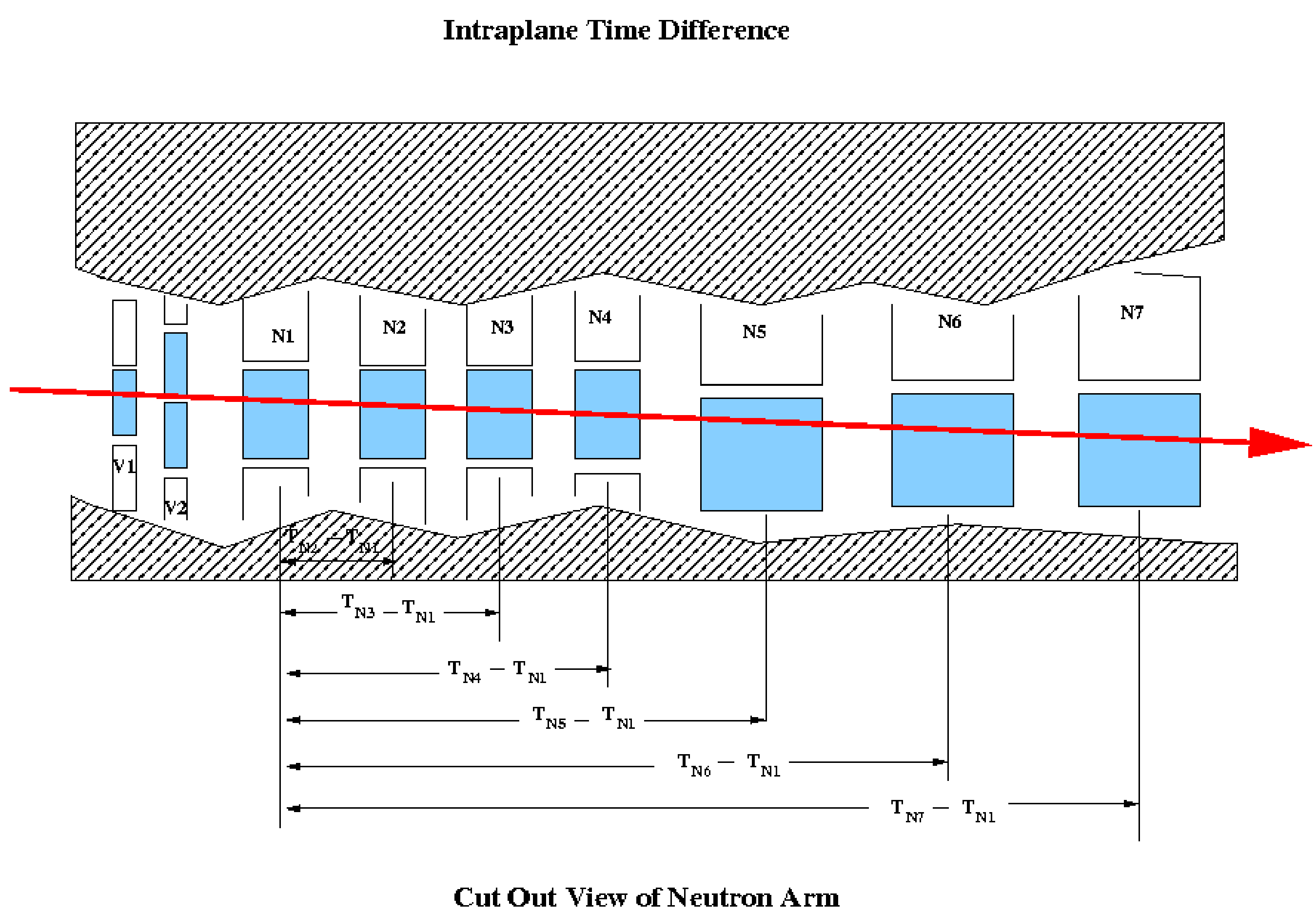

Figure 34: Cutout view of Neutron Arm showing the event selection.

and Pdiff<0.04, as is shown in figure 35.

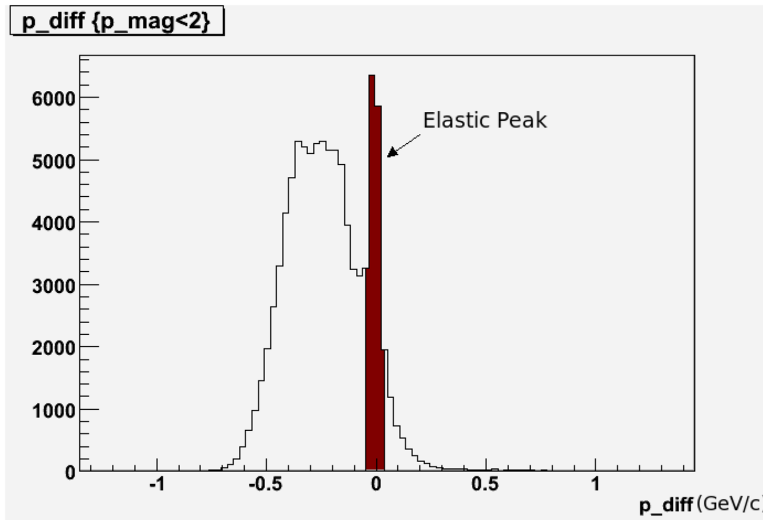

Figure 35: Cut on Pdiff

In a reaction such as (e,e'x), using conservation of energy and momentum, we can use the information of the scattered electron from BigBite and the initial energy of the electron beam and mass of the target to generate a spectrum of the missing energy of 'x'. What is meant by "missing energy of x" is simply the unmeasured energy of x. In the case of an assumed two body final state, that is the outgoing particles are the electron and a single hadron, the energy and momentum conservation laws predict sharp values for the electron's energy which depend upon the mass of the undetected hadron. The missing mass in the case of scattering from a hydrogen target will be the mass of the proton's ground state or excited states. Thus we can identify true elastic scattering events by selecting only those electrons whose energies are consistent with scattering off a proton in its ground state. The resulting plot of the missing mass squared for hydrogen data, W^2 is plotted in figure 36. In general the mass of the nucleon squared is approximately 0.88 GeV^2, here the broad peak with the gaussian fit is .9045 GeV^2

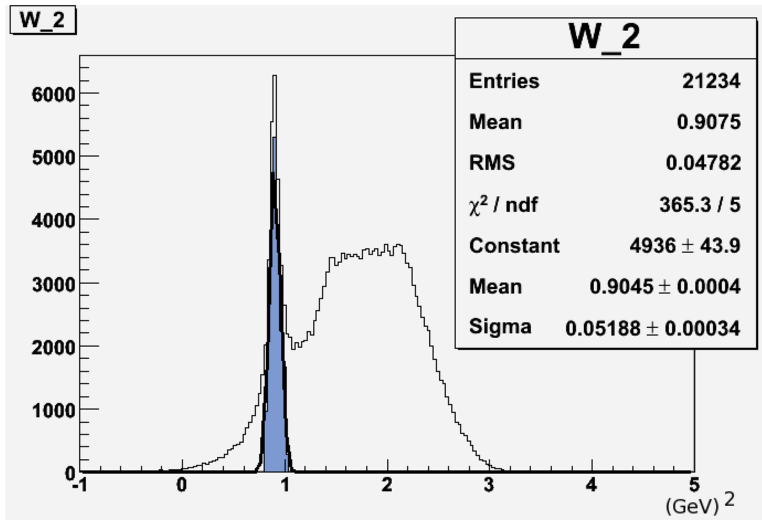

Figure 36: Missing Mass squared.

Using the event display, figure 37, to show the results of the cuts on an event by event basis, ensures that we are selecting a good proton track. The circled boxes are the events that are identified as a good proton hit. The values inside the boxes are the corresponding pedestal subtracted ADC channels of the PMTs. Here we see matching bars being hit in planes N1 through N4 on both the left and the right side of the detector. In plane N5 the bar is shifted due to the different sizes of the scintillator planes being used.

The histograms in figures 38, and 39 show the intraplane time difference for selected scintillator bars in a hydrogen run fitted with a gaussian curve.

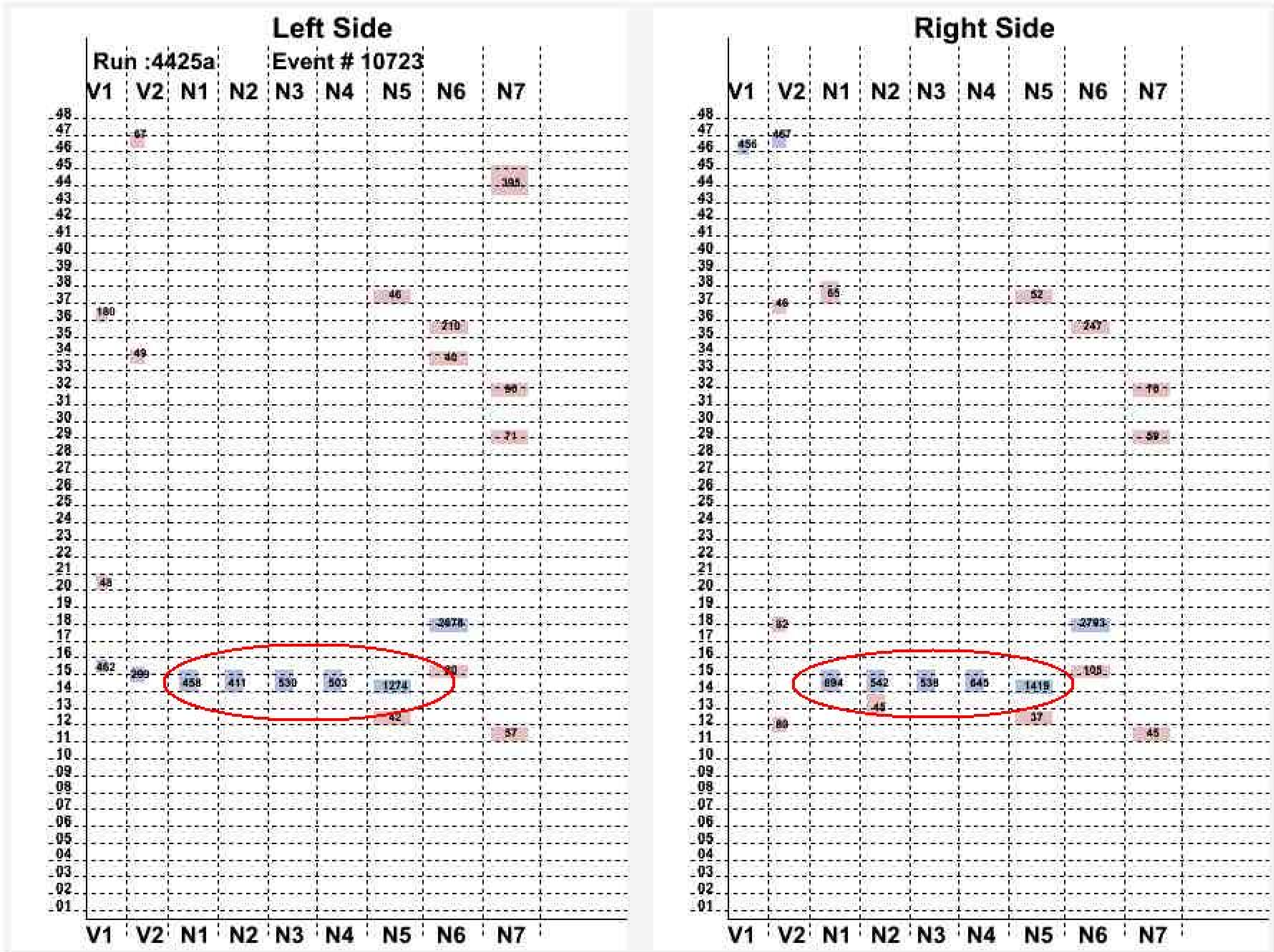

Figure 37: Event display of a good proton track. The y-axis represents bar numbers of the V1 plane and the x-axis represents the planes of the Neutron Arm.

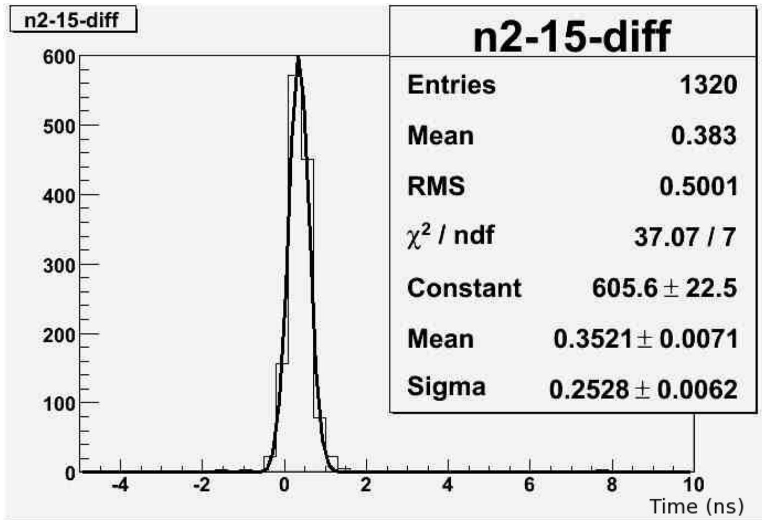

Figure 38: Intraplane time difference of bar 15 in plane N2 and bar 15 of the N1 plane.

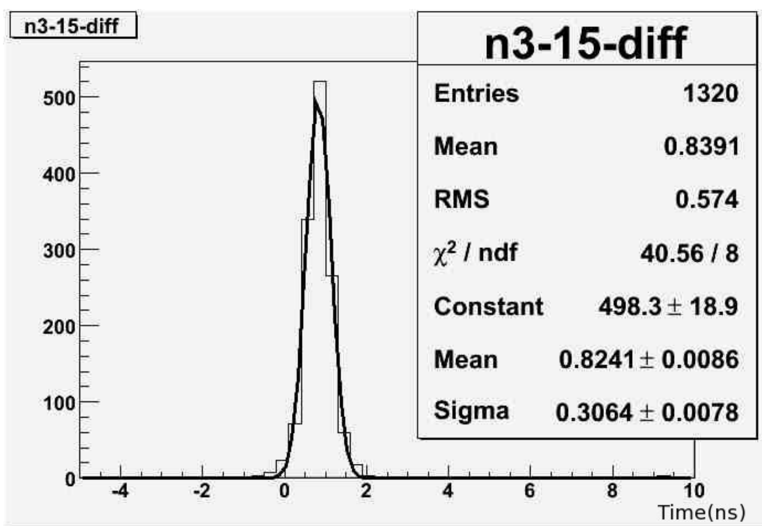

Figure 39: Intraplane time difference of bar 15 in plane N3 and bar 15 of the N1 plane.

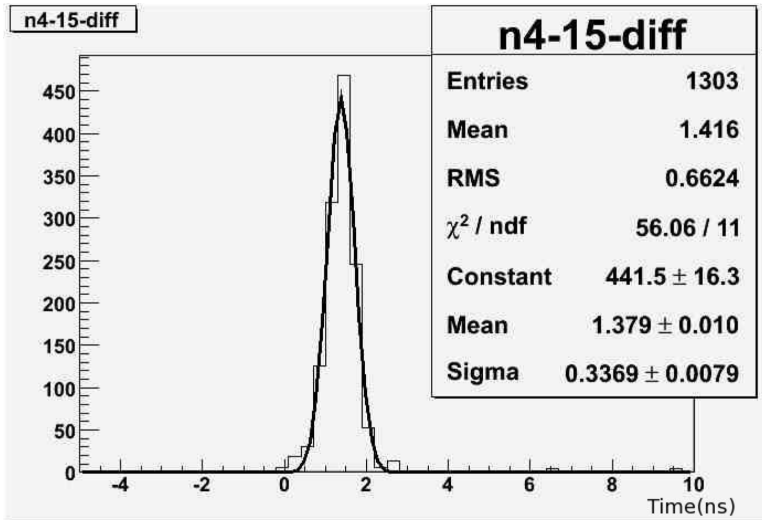

Figure 40: Intraplane time difference of bar 15 in plane N4 and bar 15 of the N1 plane.

The figures 41 and 42 shows the mean values of the gaussian fit along with its associated error for all bars in the Neutron Arm. Figure 41 shows the intraplane differences without any offsets applied.

Applying an offset to the different bars so that the intraplane time differences are set to zero, then adding a constant for clarity purposes, we get a plot depicted in figure 42. Notice that with the offsets added not all of the values fit the horizontal line. This is a statistical effect due to binning yielding a low number of counts. We now apply the offsets obtained from hydrogen data to helium data.

8.3 HELIUM DATA

Using helium data the we no longer have an elastic peak, so we will be selecting around the region of quasi-elastic event as is shown in figure 43.

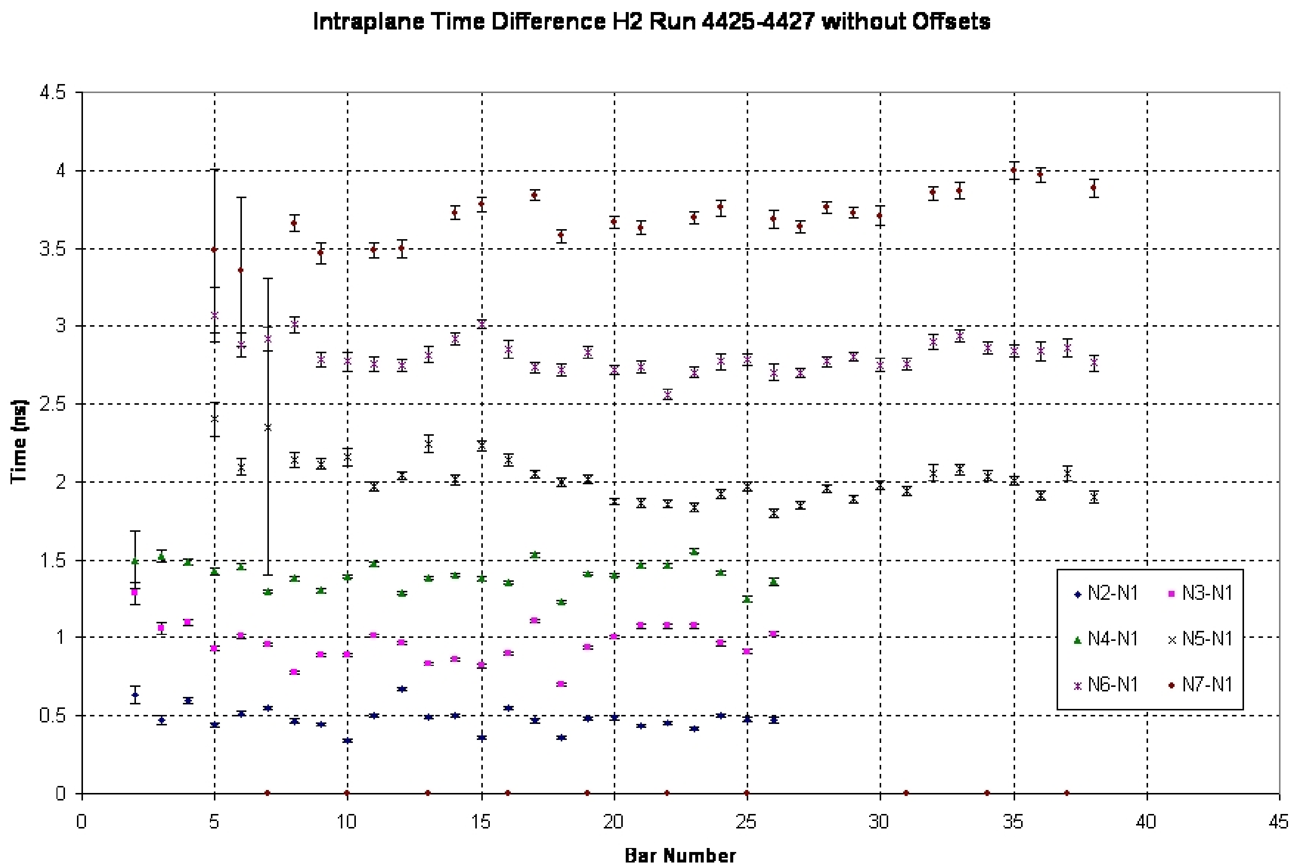

Figure 41: Intraplane time difference with no offset applied.

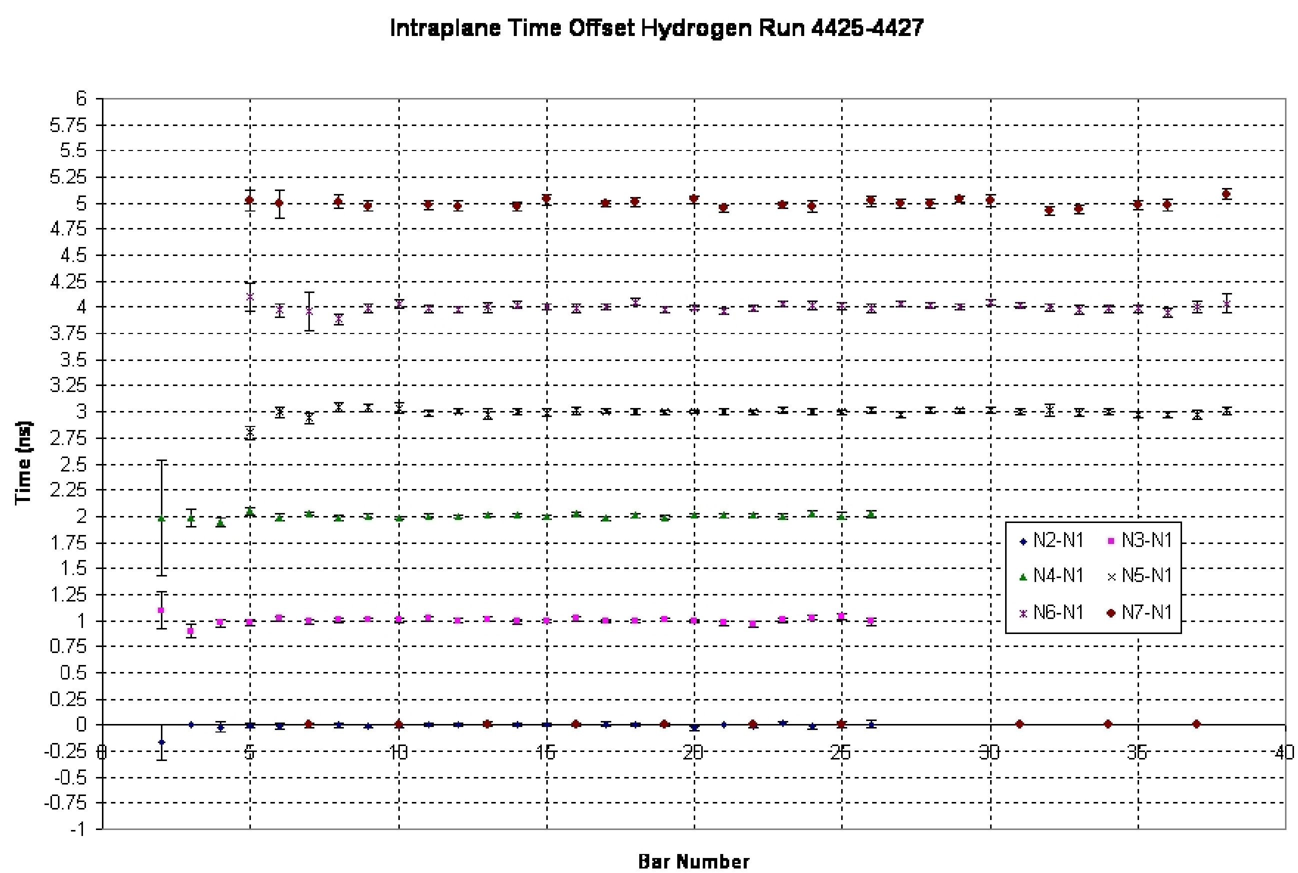

Figure 42: Intraplane time difference with offset applied so that the values are centered at zero, then a constant is added to the values to separate the different planes for clarity purposes.

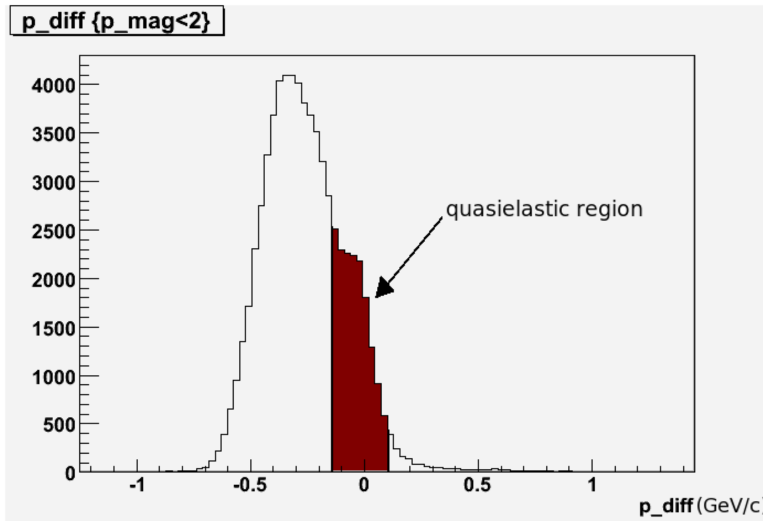

Figure 43: Pdiff plot for helium

Resulting missing mass squared, W^2, for helium data is shown in figure 44. As we can see the missing mass value is larger then we expect due to the wider cut on Pdiff.

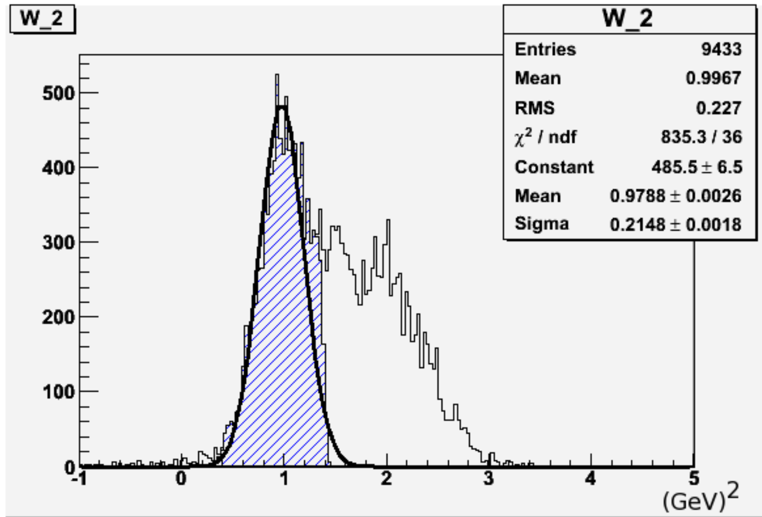

Figure 44: W^2 plot for helium

In order to compare hydrogen data to helium data from kinematic 4, we use offsets obtained from the hydrogen run and apply them to the helium data. The offsets applied to the ^{3}He should line the points on zero of the x-axis, but as we see that some of the values still need further offsets added, more so at the top and bottom of the detectors, see figures 46 through 51.

We now compare other kinematic 4 runs that are closer to the end of the run to see how stable the intraplane time differences are from the beginning of kinematic 4 to the end of kinematic 4.

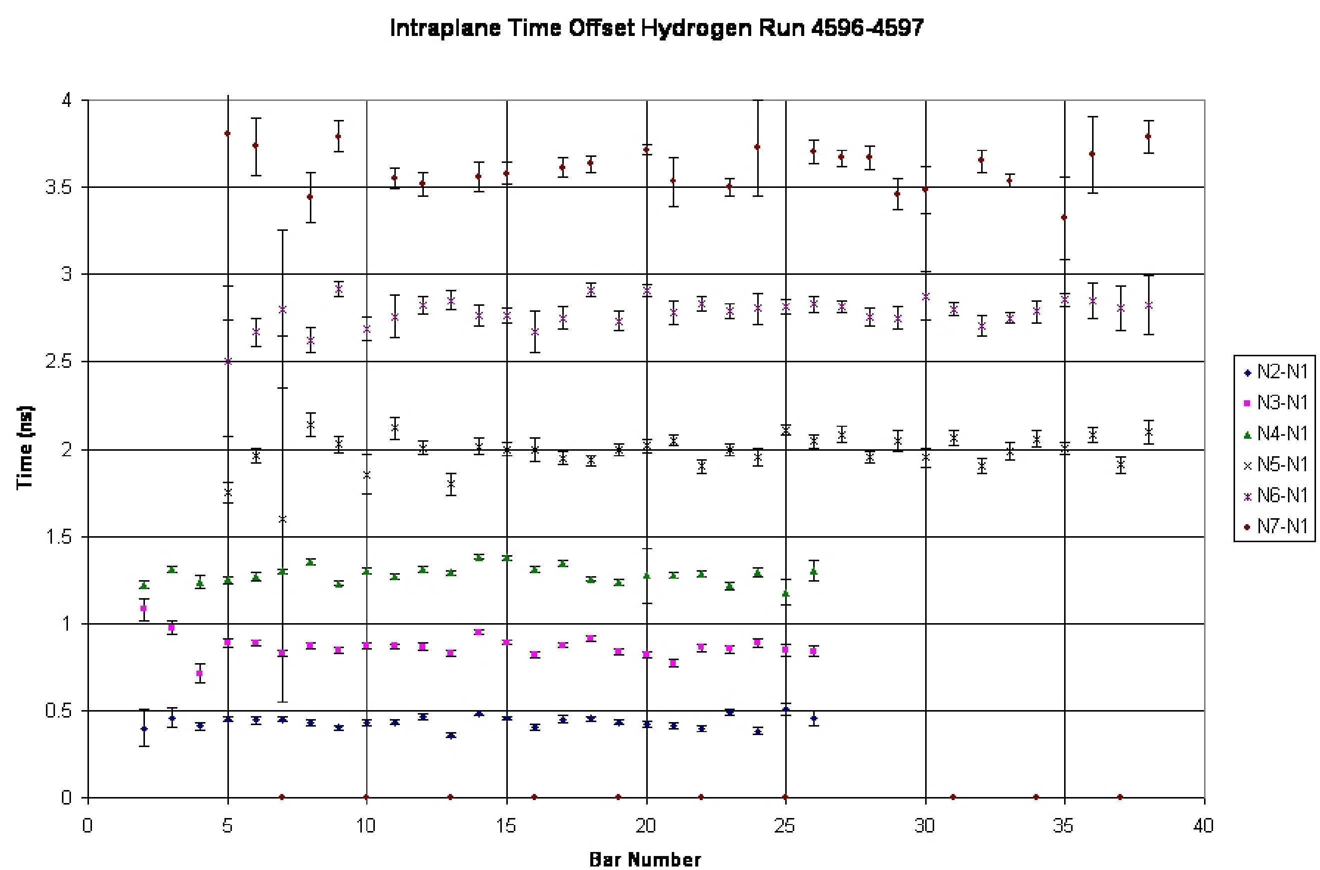

Figure 45: Intraplane time difference with offset applied to ^{3}He data. Constant is added to the values to separate the different planes.

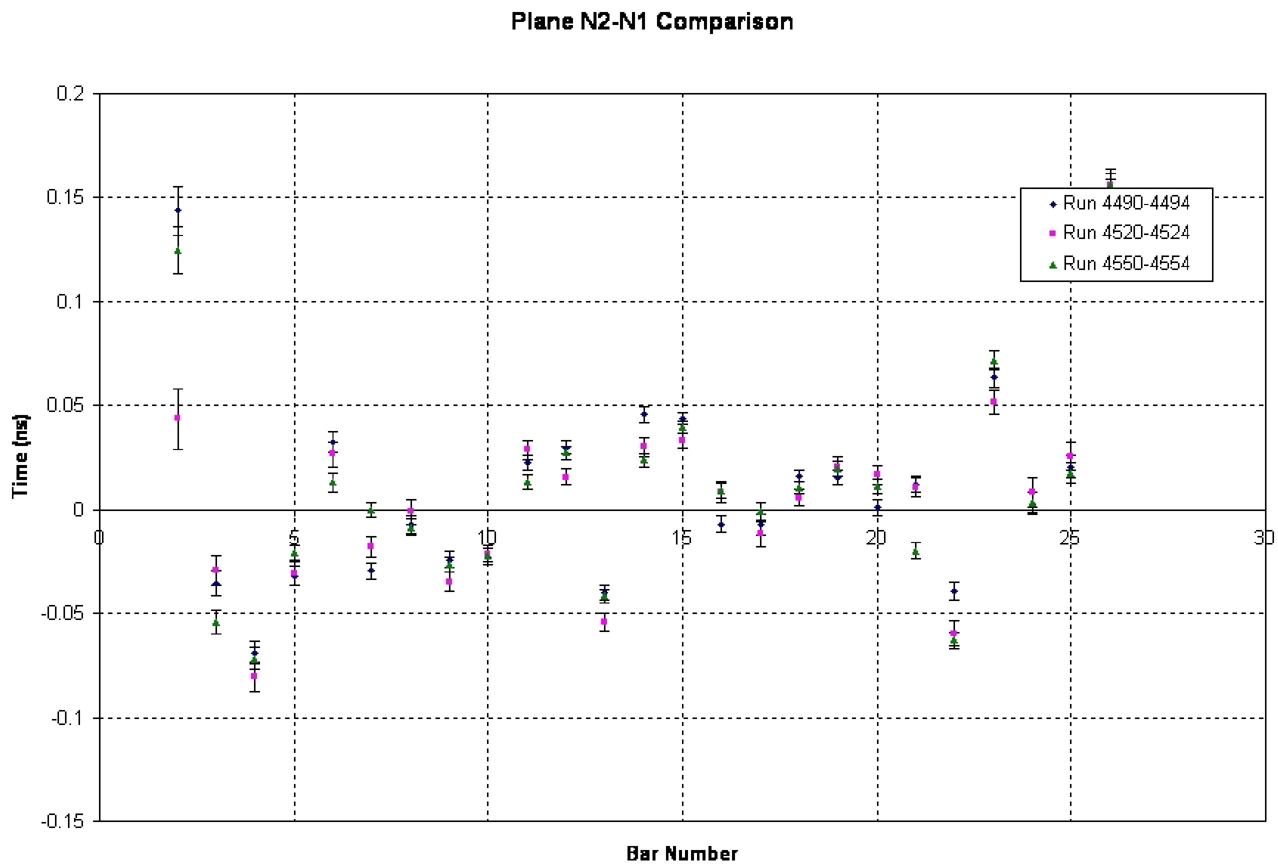

Figure 46: Intraplane time difference N2-N1 plane

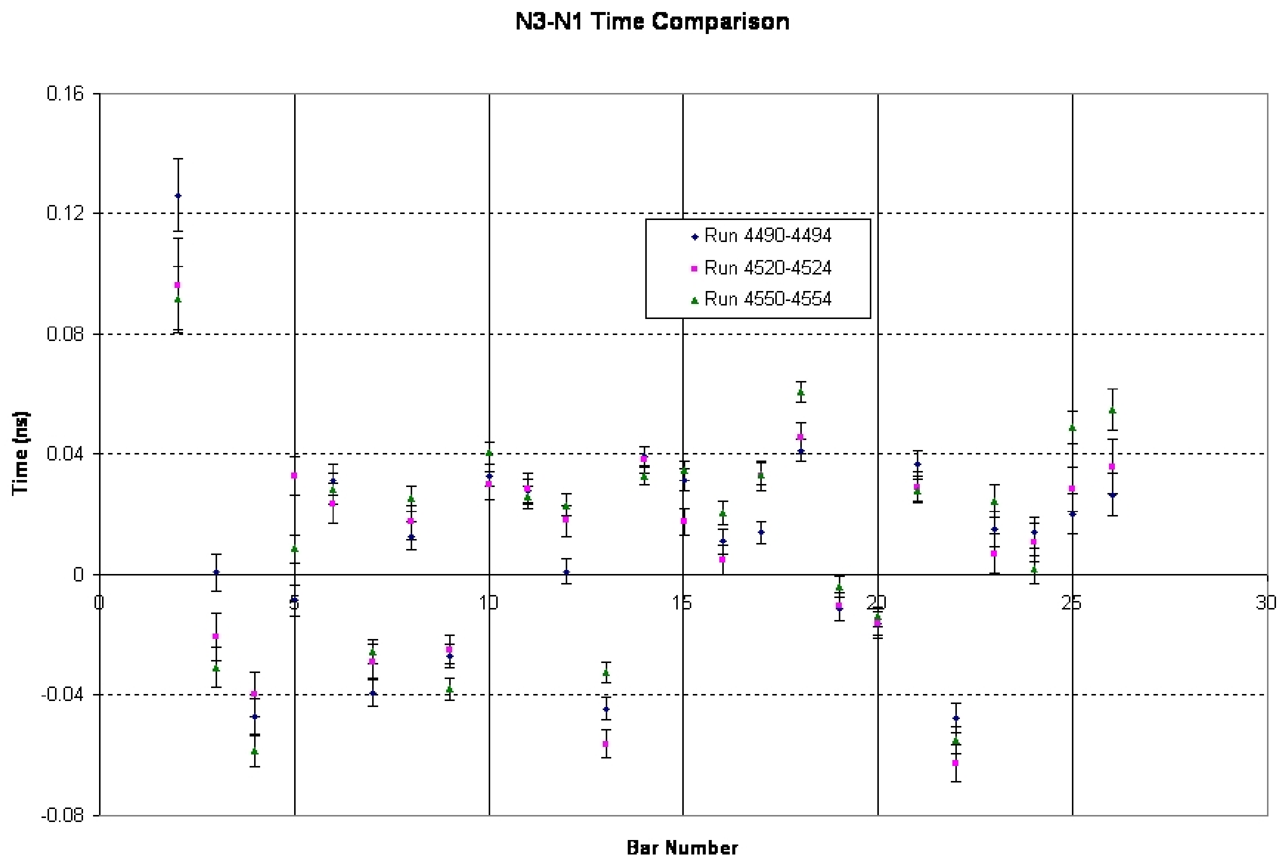

Figure 47: Intraplane time difference N3-N1 plane

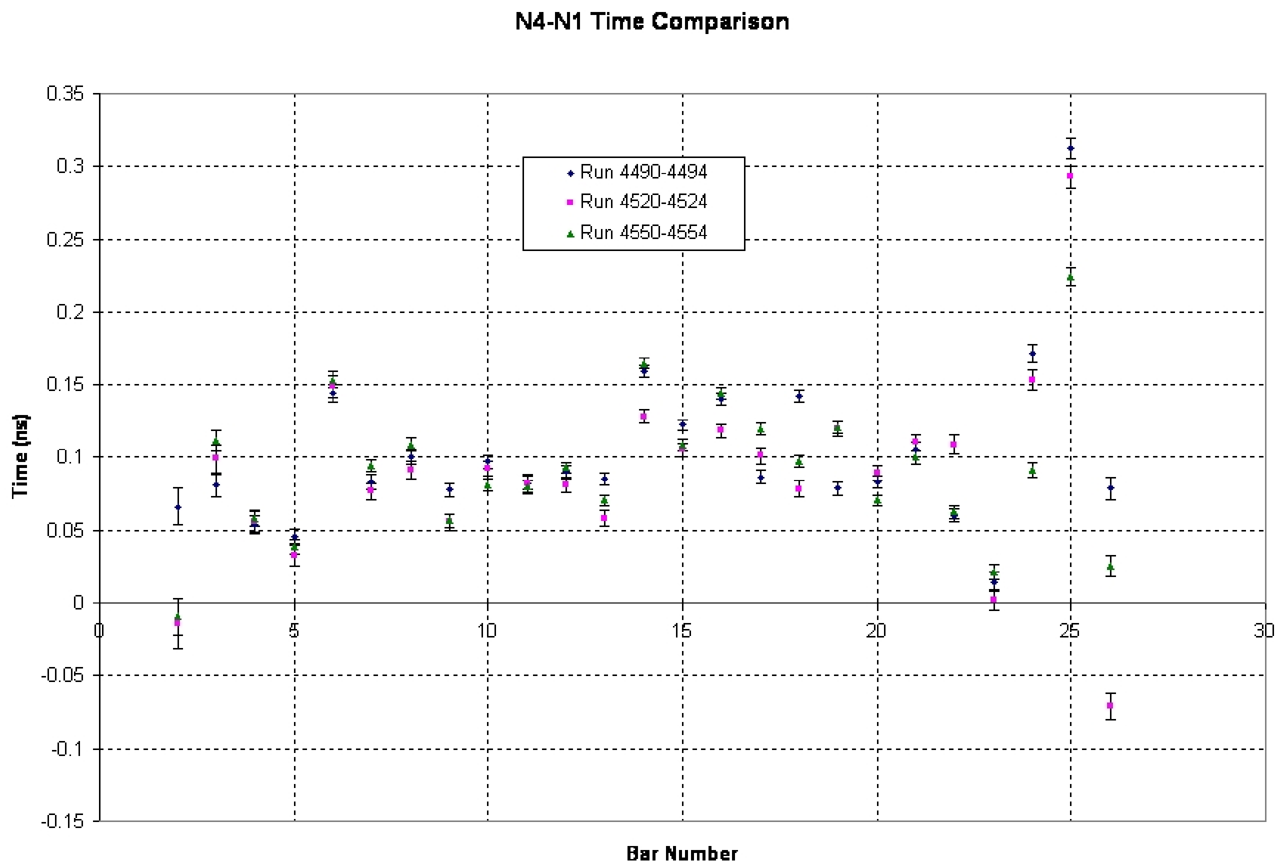

Figure 48: Intraplane time difference N4-N1 plane

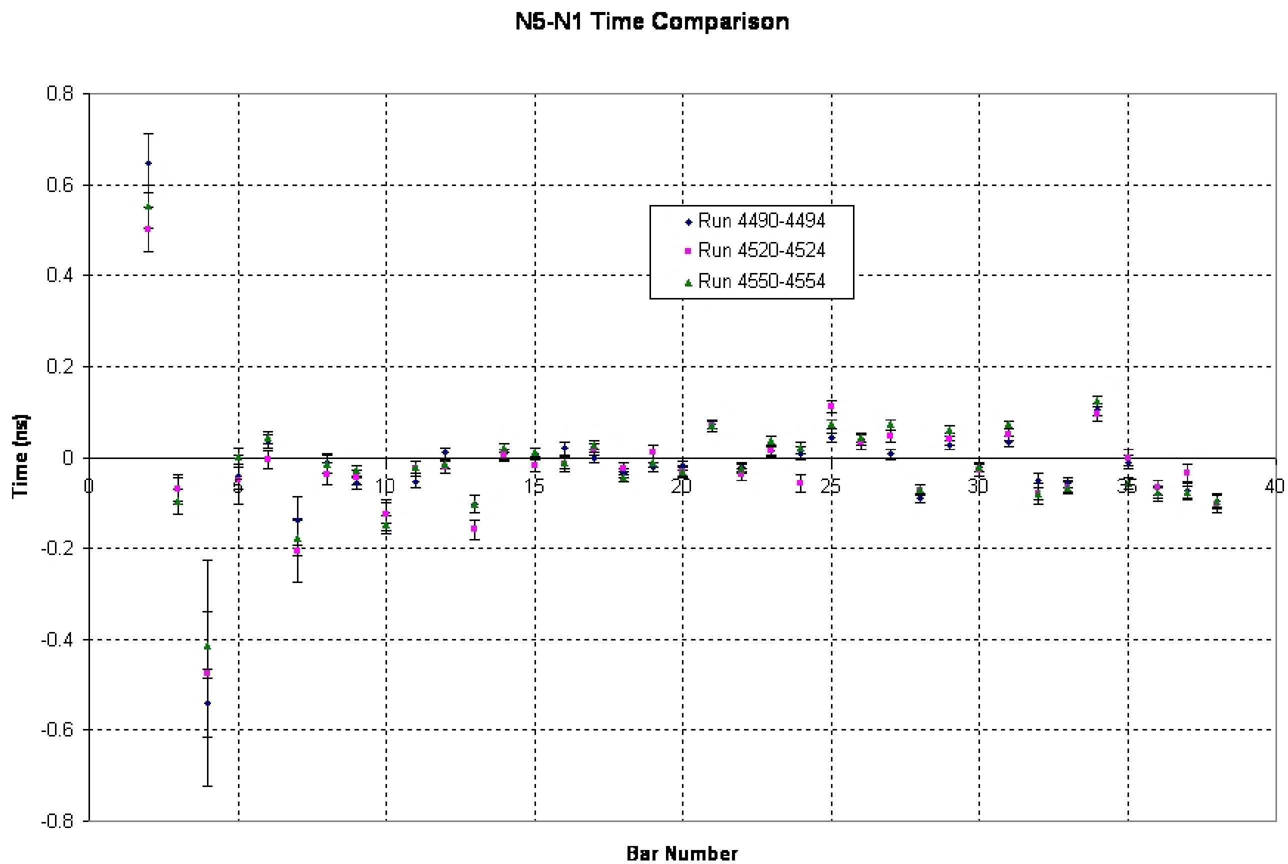

Figure 49: Intraplane time difference N5-N1 plane

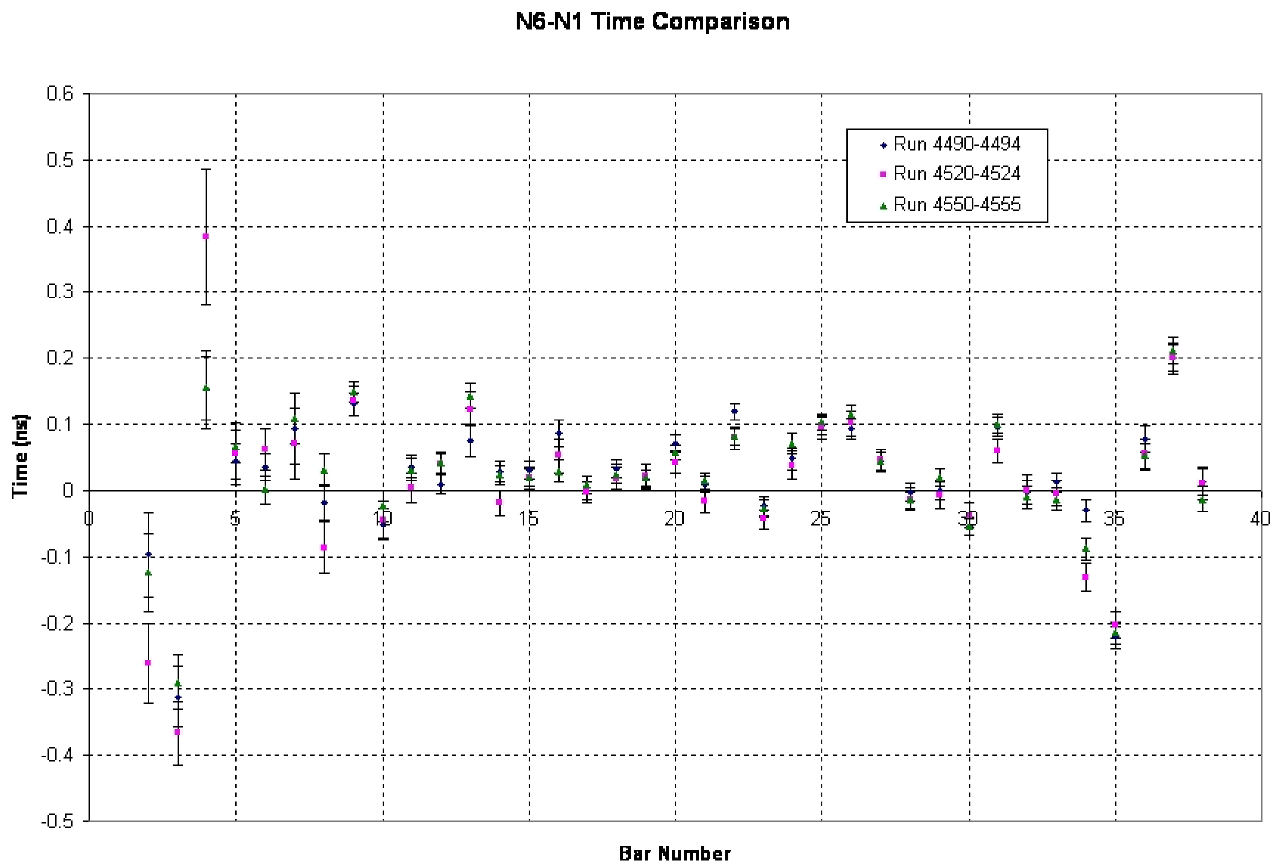

Figure 50: Intraplane time difference N6-N1 plane

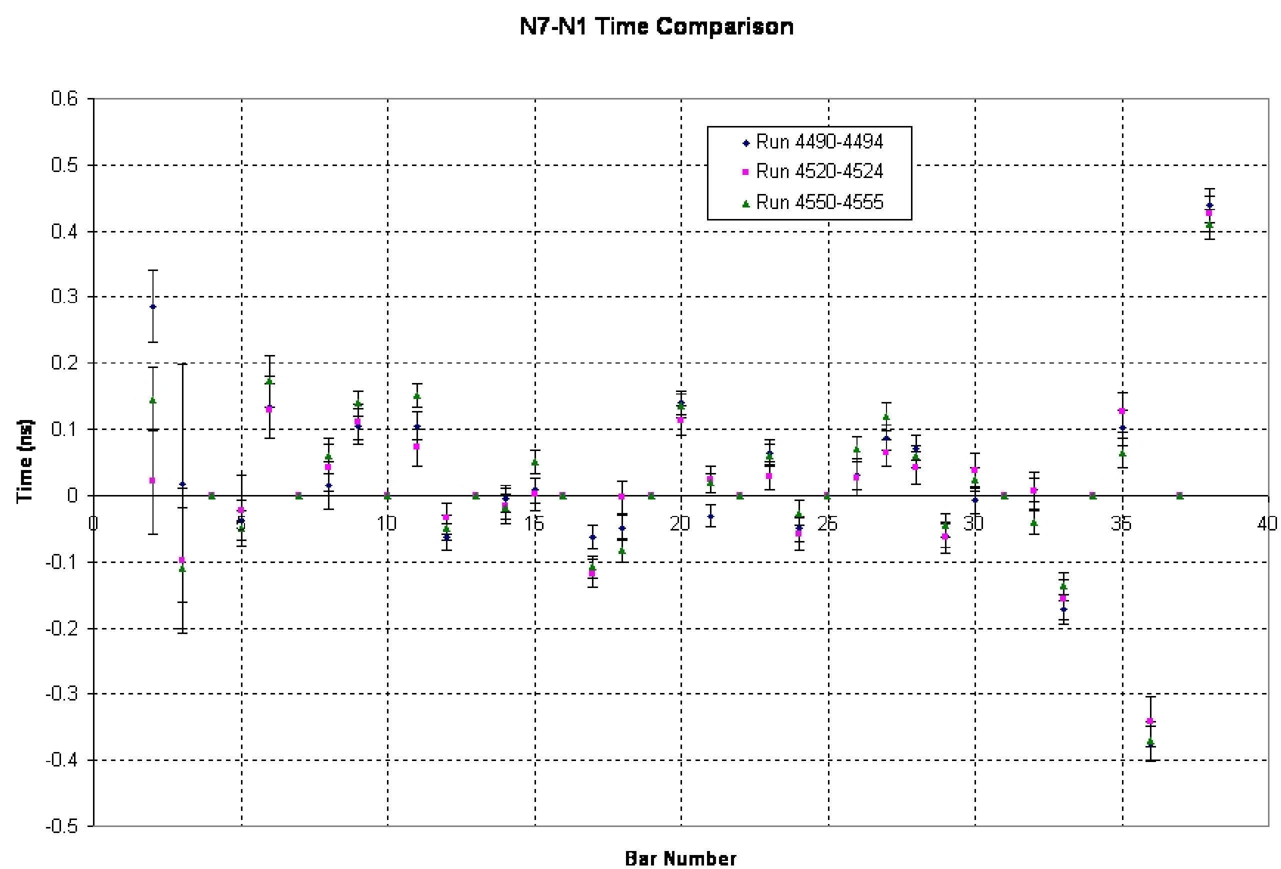

Figure 51: Intraplane time difference N7-N1 plane

Although using offsets obtained from hydrogen data still requires additional offsets to be applied, we see that when comparing all the helium data, there are very little fluctuations. This might be due to the limited statistics that we have when using hydrogen data than with the helium data. This leads us to try to use long tracks in helium data at the beginning of a kinematic run and comparing it to the end of the kinematic run. Applying offsets to helium data from the beginning of kinematic 4, runs 4490-4494, and plotting the gaussian fit with it associated error in figure 52, we see that the points are very well aligned. Using the offsets obtained from runs 4490-4494 and applying them to other helium data at the end to kinematic 4 we can check how stable these offsets are. In figures 53 and 54 we see that the points are also very well aligned much in the same way as figure 52.

In figures 55 through 60 comparing the different helium runs in kinematic 4 plane by plane, we see that the variances that we have across all of the scintillator bars is within 100ps which is about the limit of the resolution of the scintillator bars. This 100ps is well within the 300ps resolution required in the proposal.

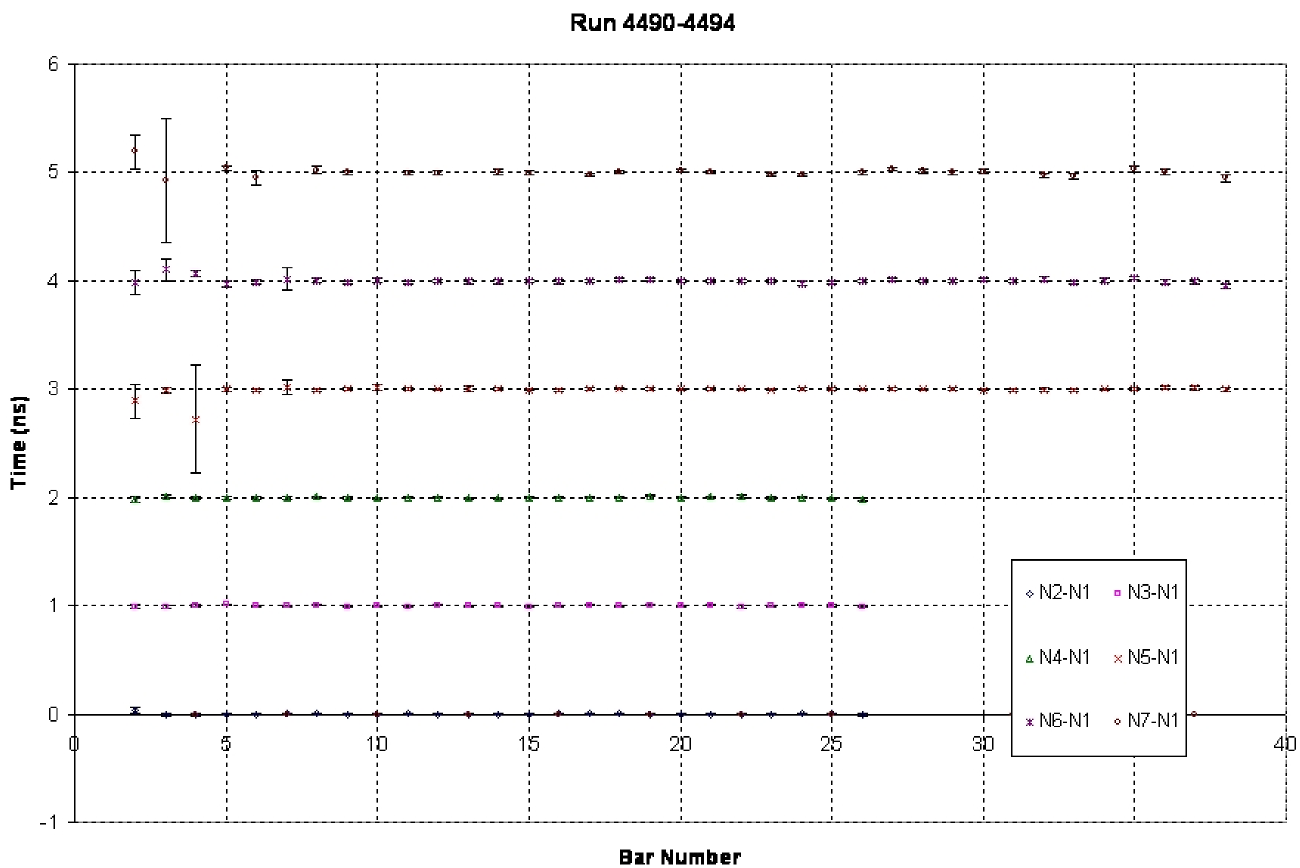

Figure 52: Intraplane time difference with offsets applied to helium data. Constant is added to the values to separate the different planes.

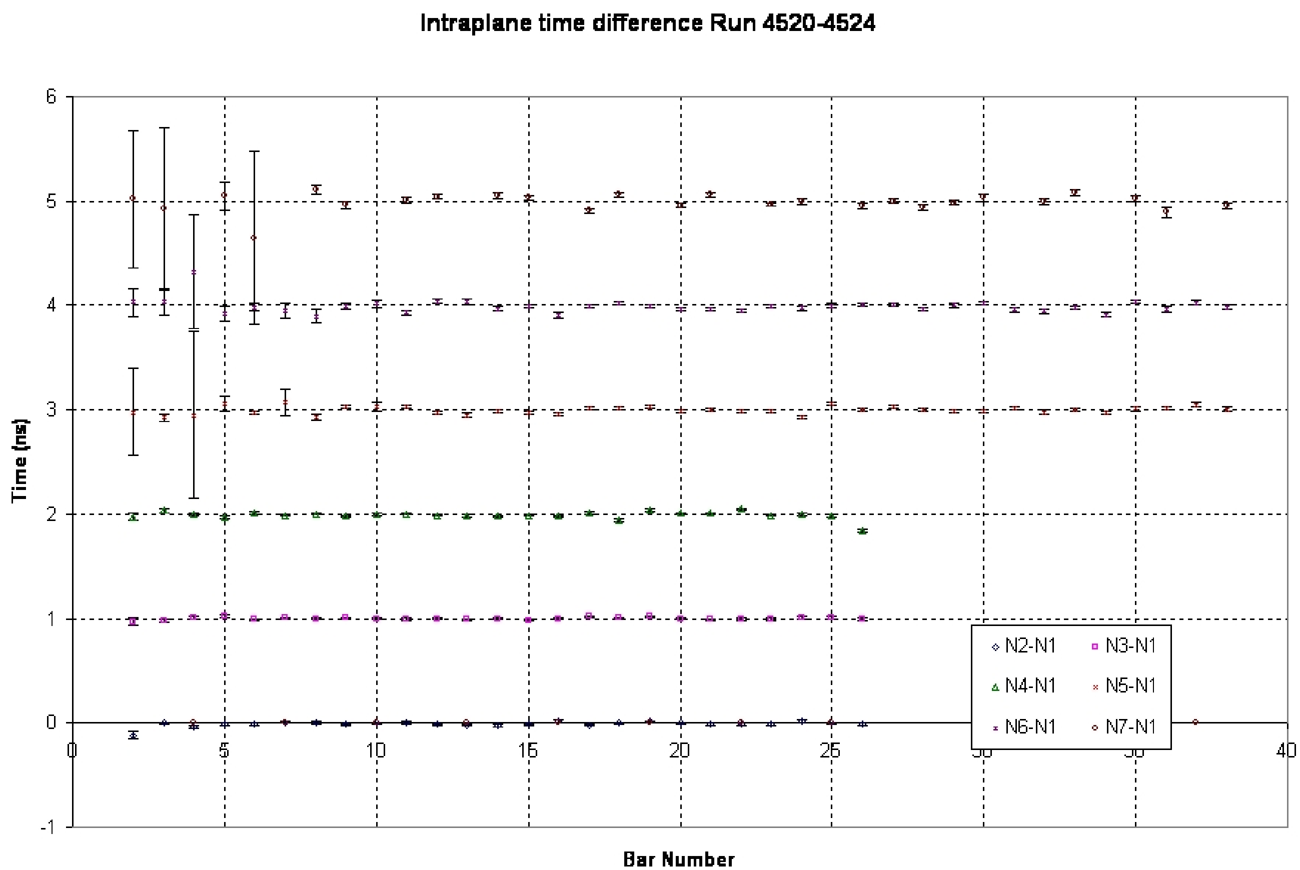

Figure 53: Intraplane time difference with offsets applied to helium data at end of kinematic 4. Constant is added to the values to separate the different planes.

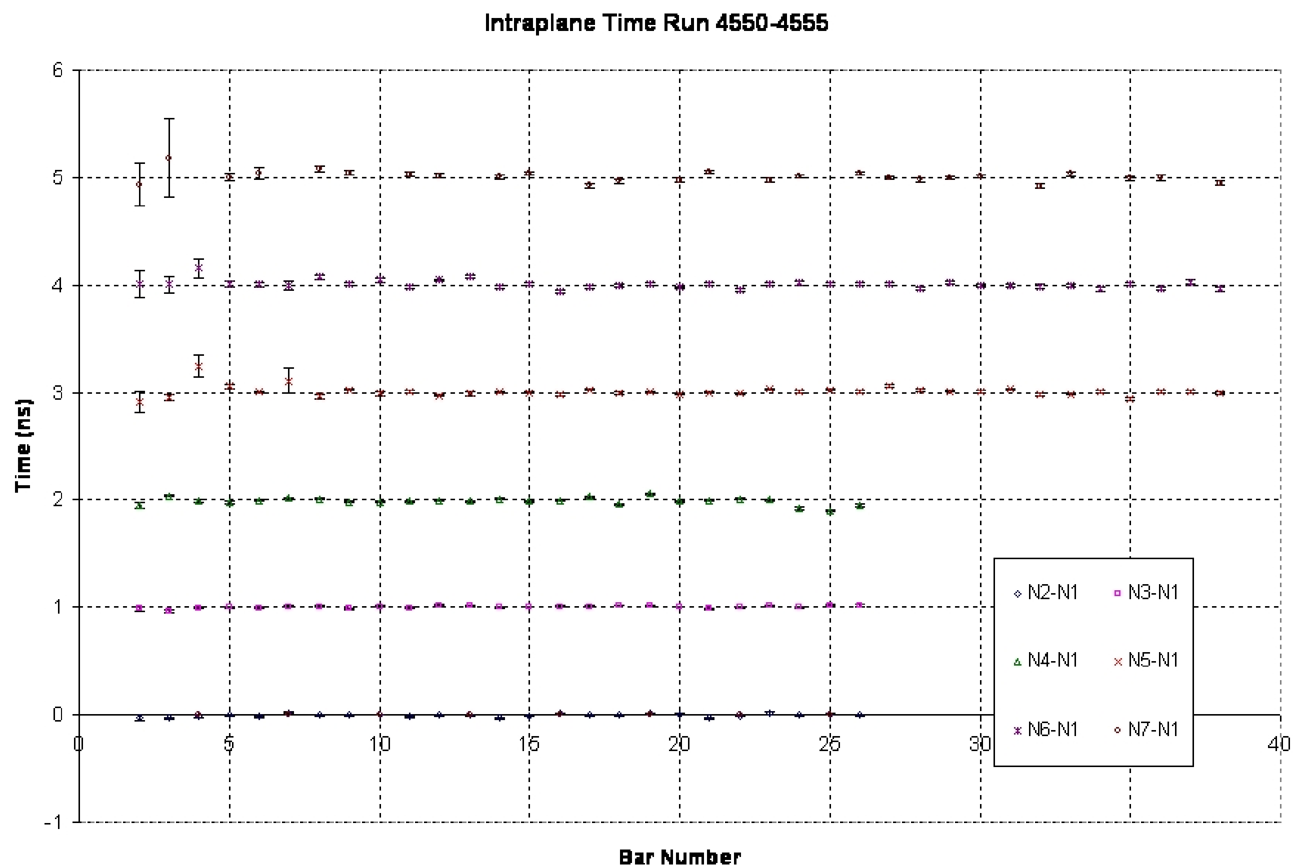

Figure 54: Intraplane time difference with offsets applied to helium data at end of kinematic 4. Constant is added to the values to separate the different planes.

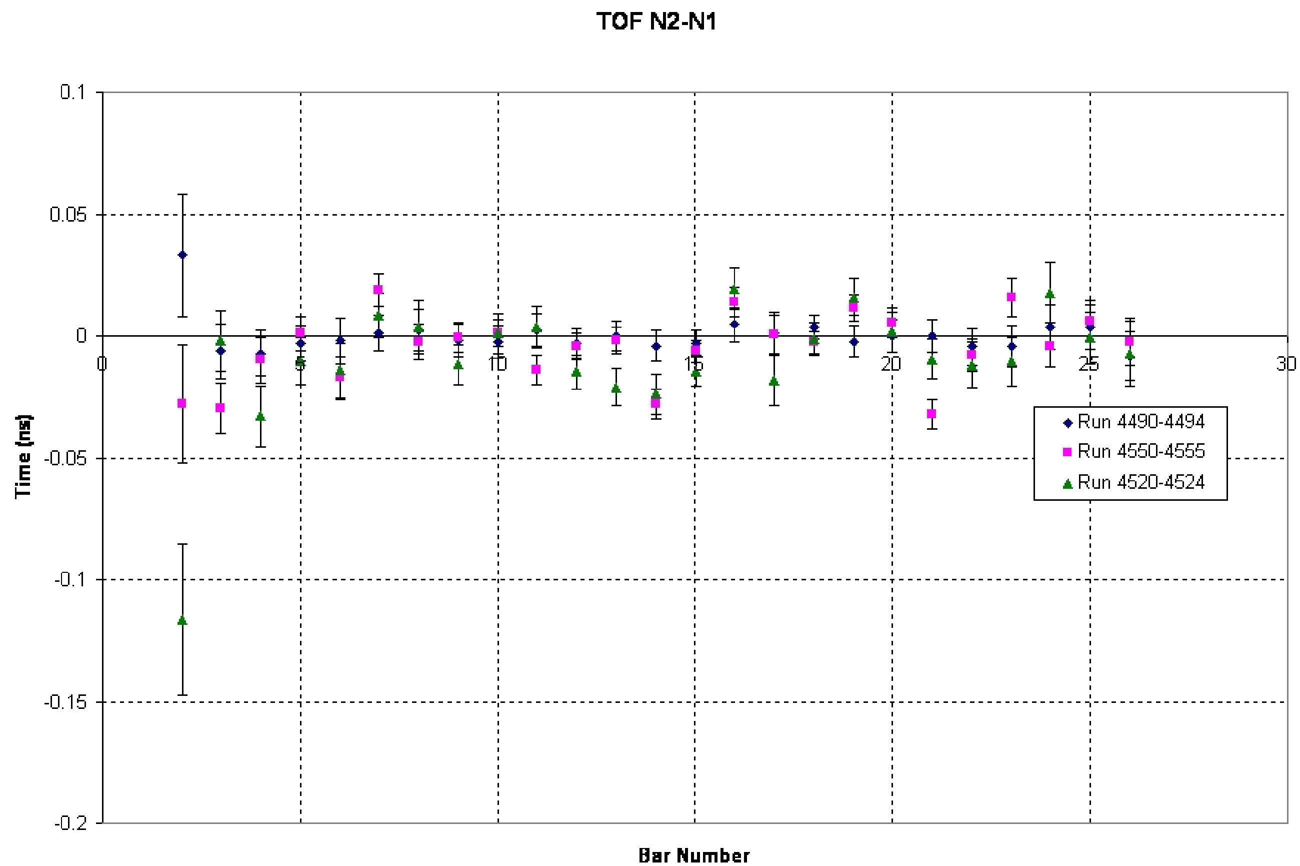

Figure 55: Intraplane time difference N2-N1 plane using helium offset

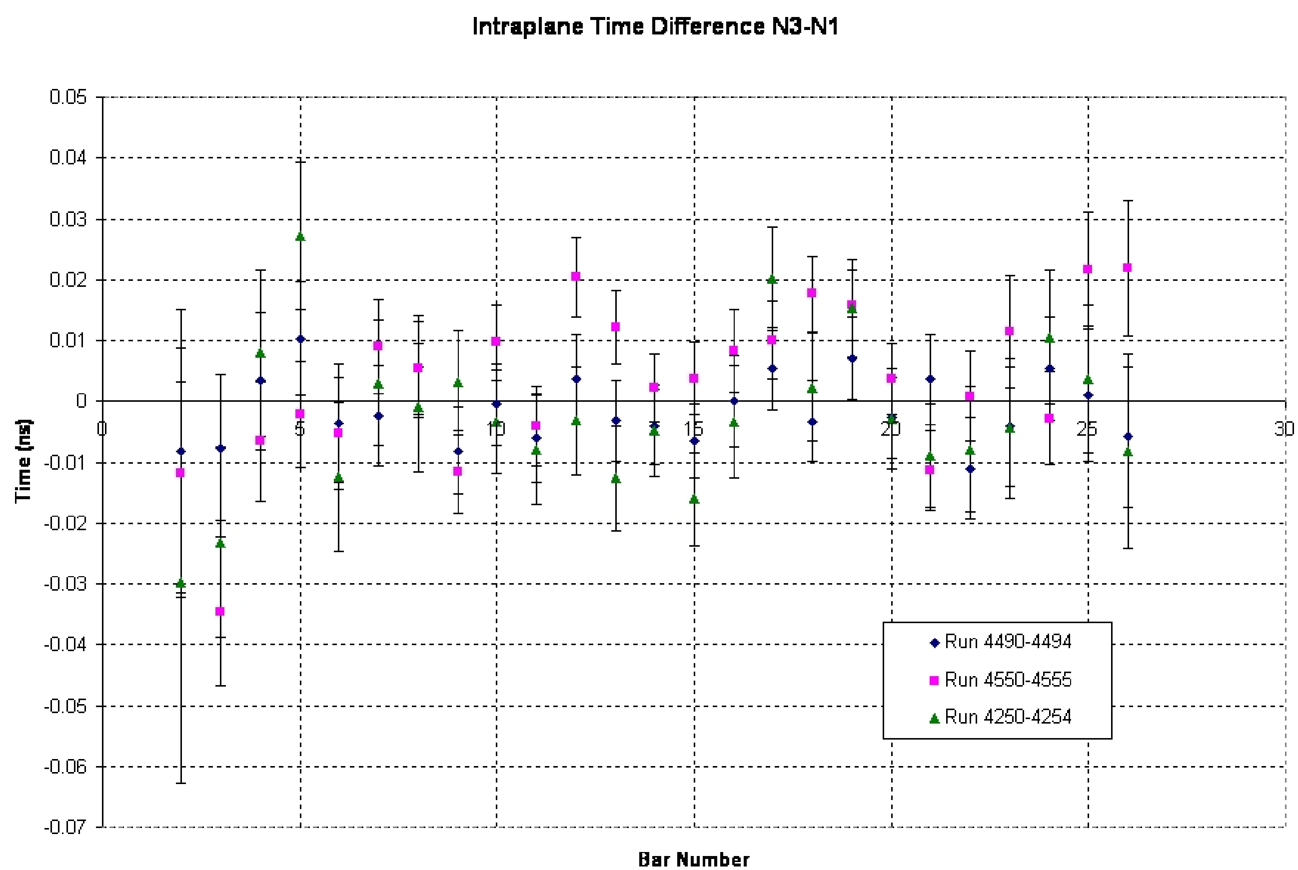

Figure 56: Intraplane time difference N3-N1 plane using helium offset

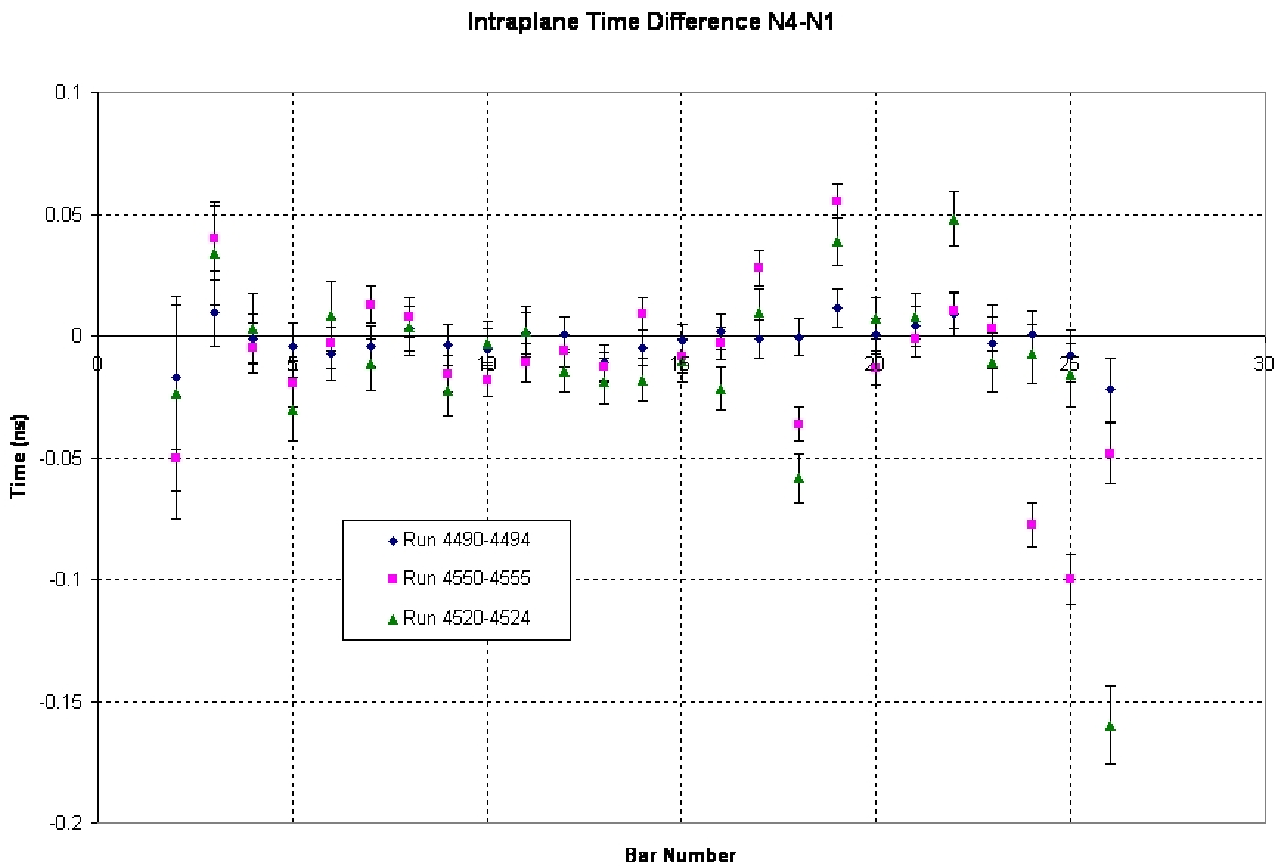

Figure 57: Intraplane time difference N4-N1 plane using helium offset

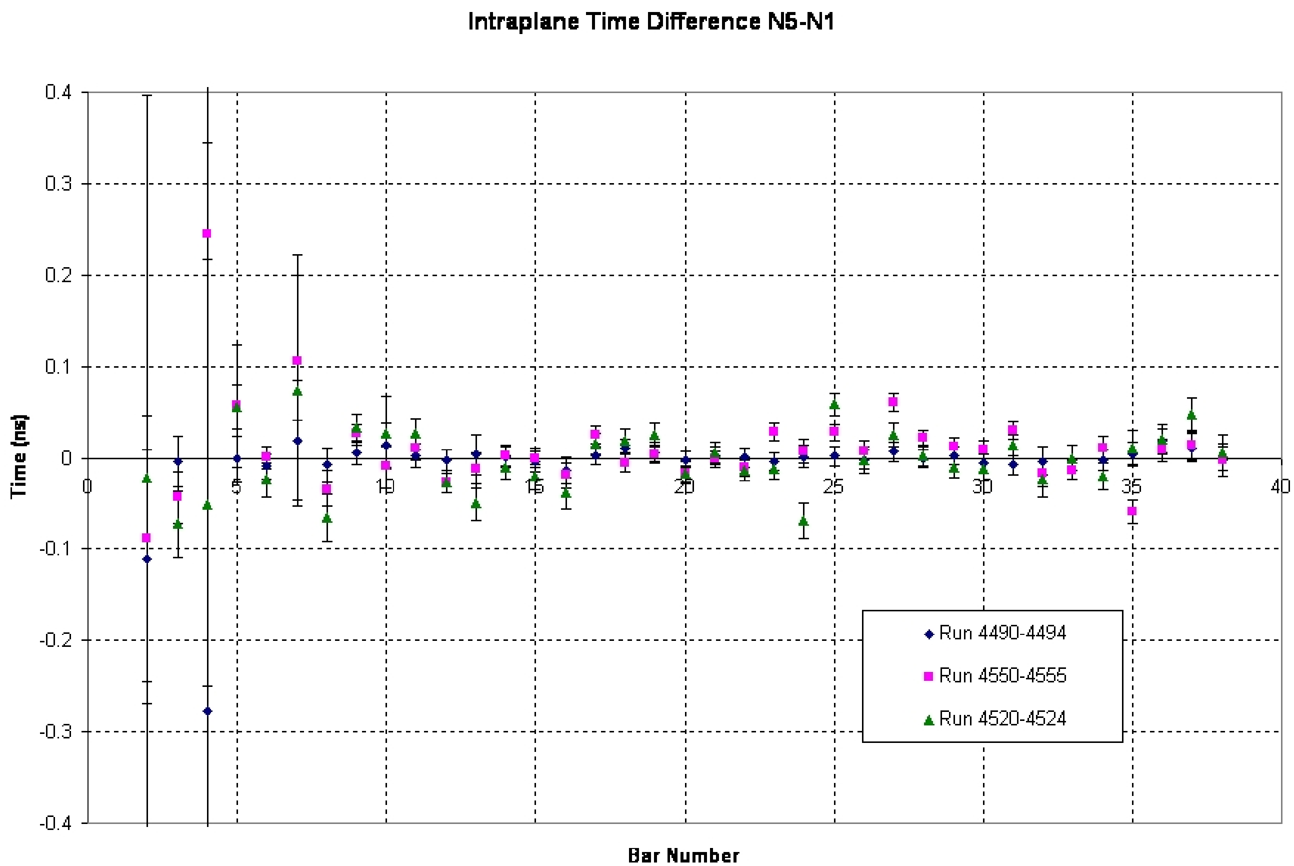

Figure 58: Intraplane time difference N5-N1 plane using helium offset

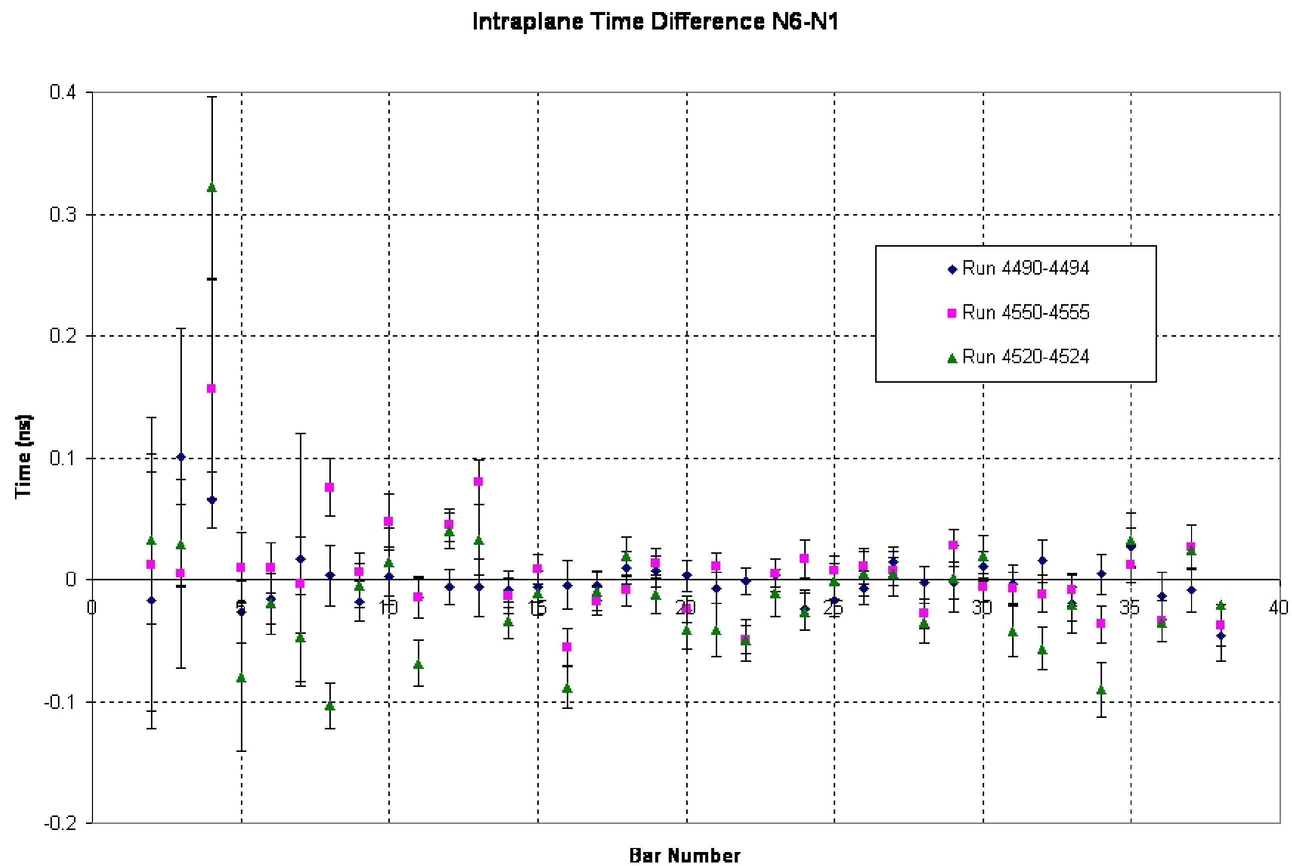

Figure 59: Intraplane time difference N6-N1 plane using helium offset

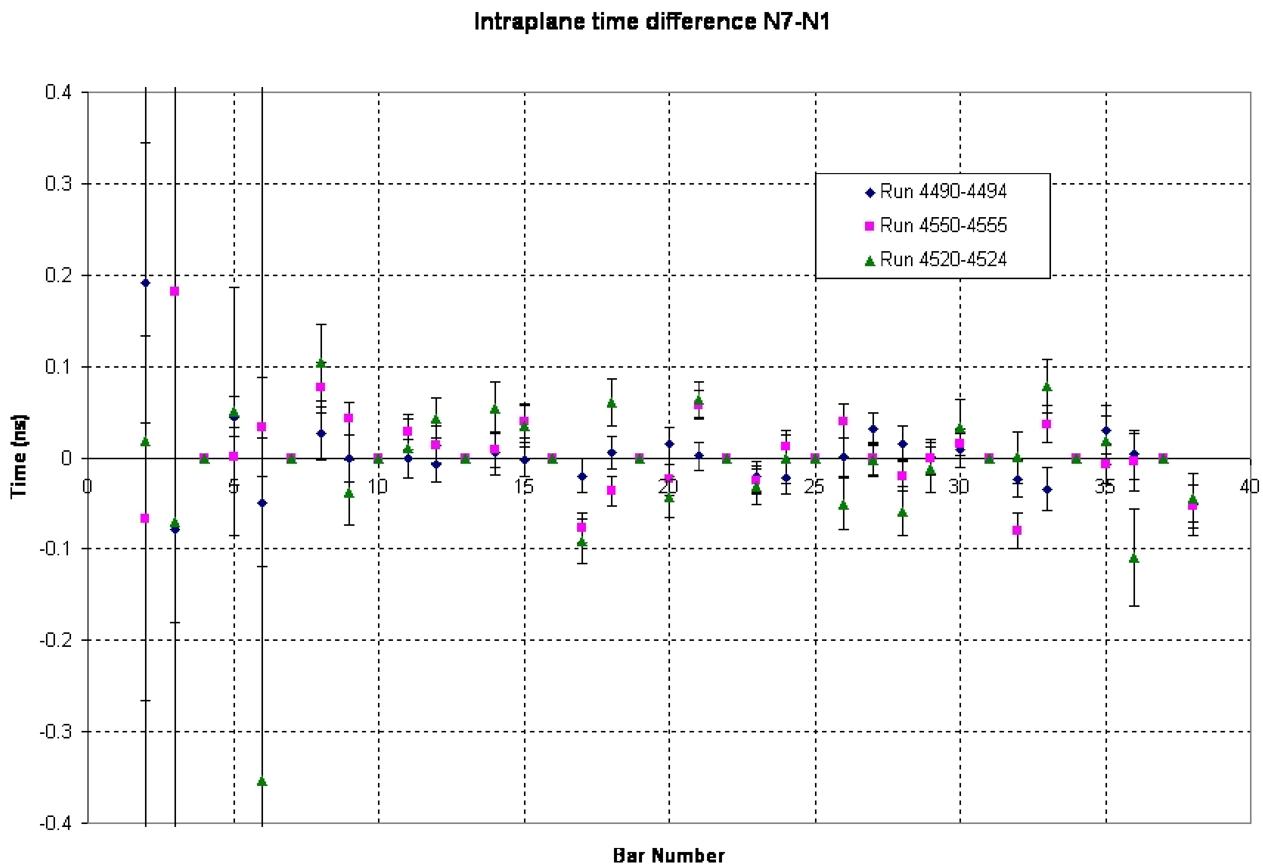

Figure 60: Intraplane time difference N7-N1 plane using helium offset

8.3.1 PMT RESPONSE TO SELECTED PROTON EVENTS

By plotting the response from the PMTs we can determine the energy deposited in each of the bars per proton event in these long tracks. We use the root mean square of the right and left PMT response in this case to generate the following plots. In figures 61 to 64, which represent the CMU scintillator bars, we compare runs at the beginning of kinematic 4 to those at the end. The variations are generally only about 5% unless it is a bar at the top or bottom of the detectors, which can vary about 10%. Figures 65 to 67 which represent the UVA scinitillator bars show a little bit more variation, about 15% at the top and bottom of the detector due to being planes at the back of the Neutron Arm. However, the bars at the center of the detector again only varied as much as 5%.

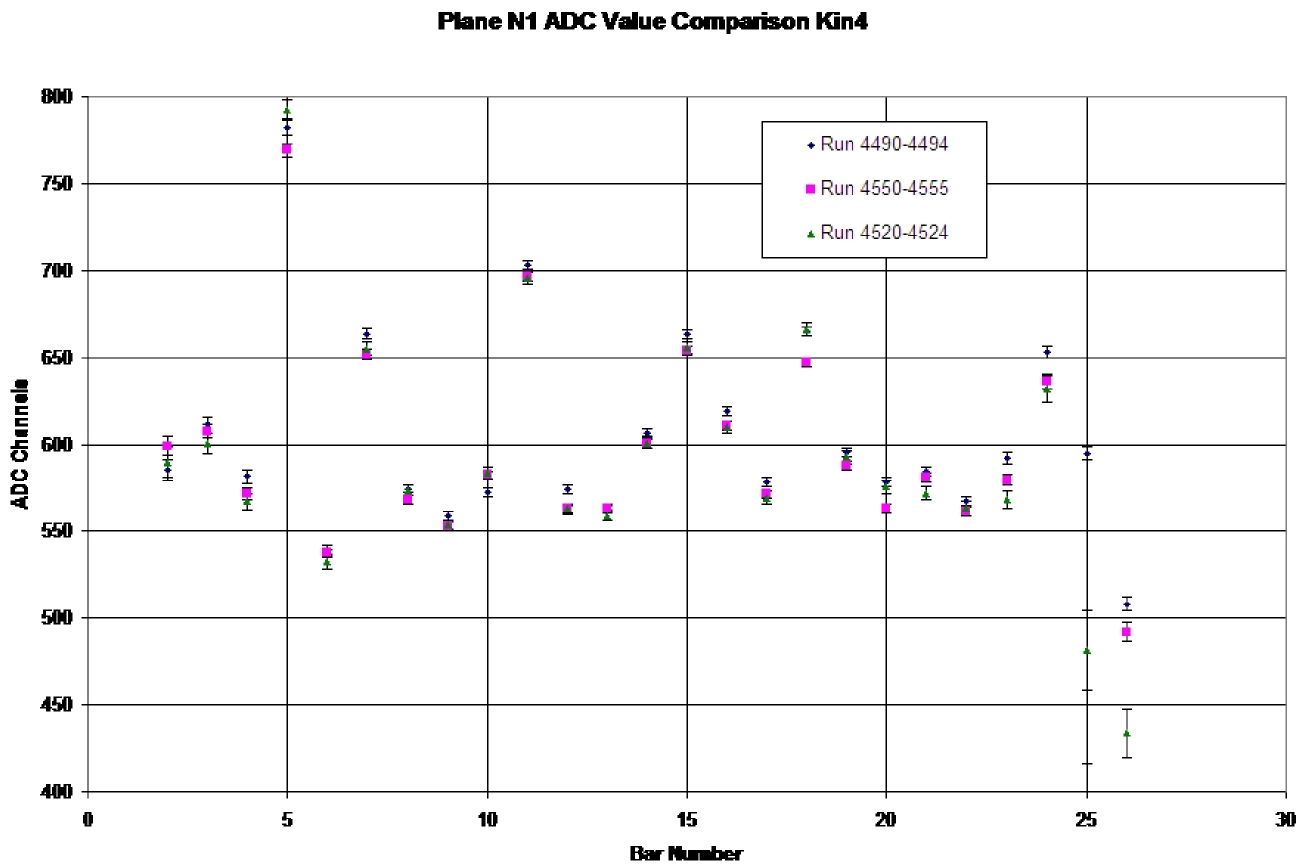

Figure 61: ADC channel response of Protons in N1 plane

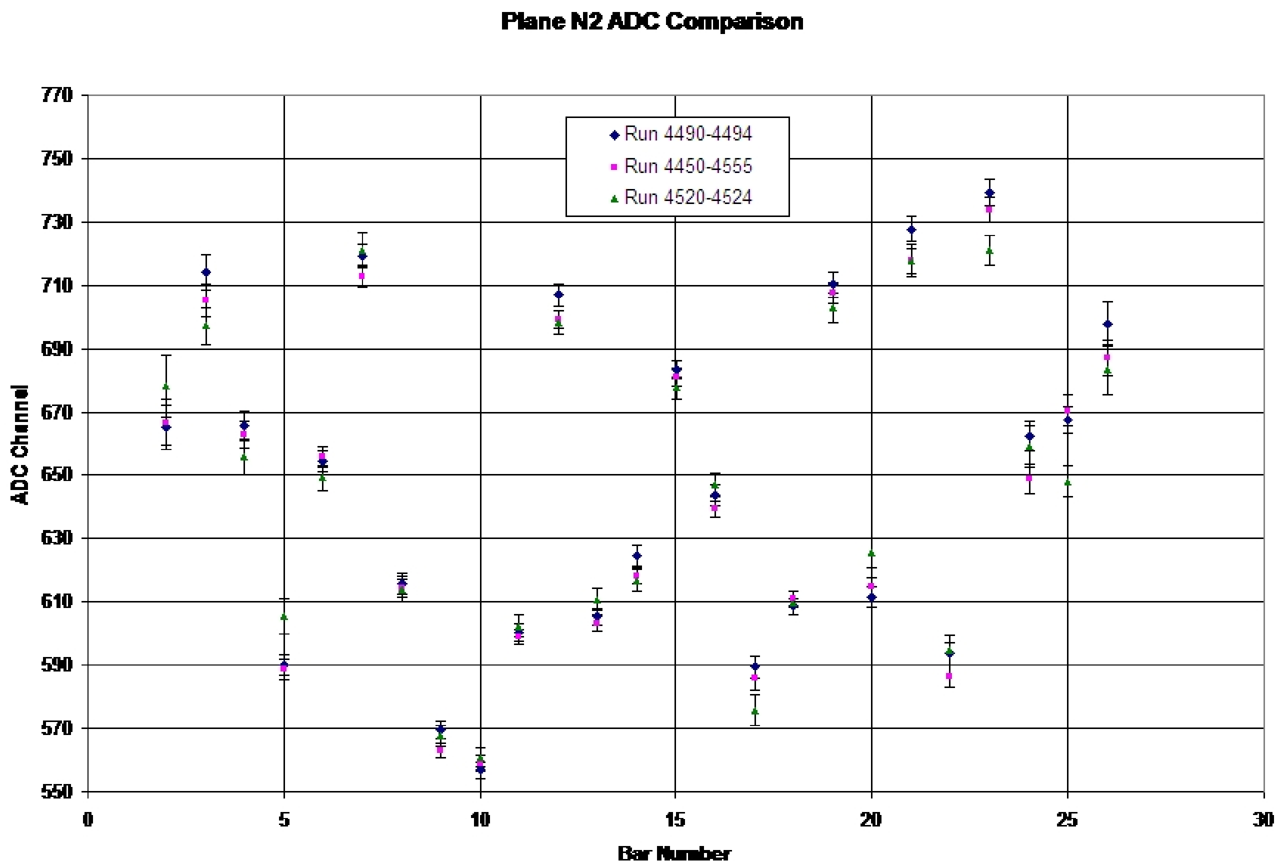

Figure 62: ADC channel response of Protons in N2 plane

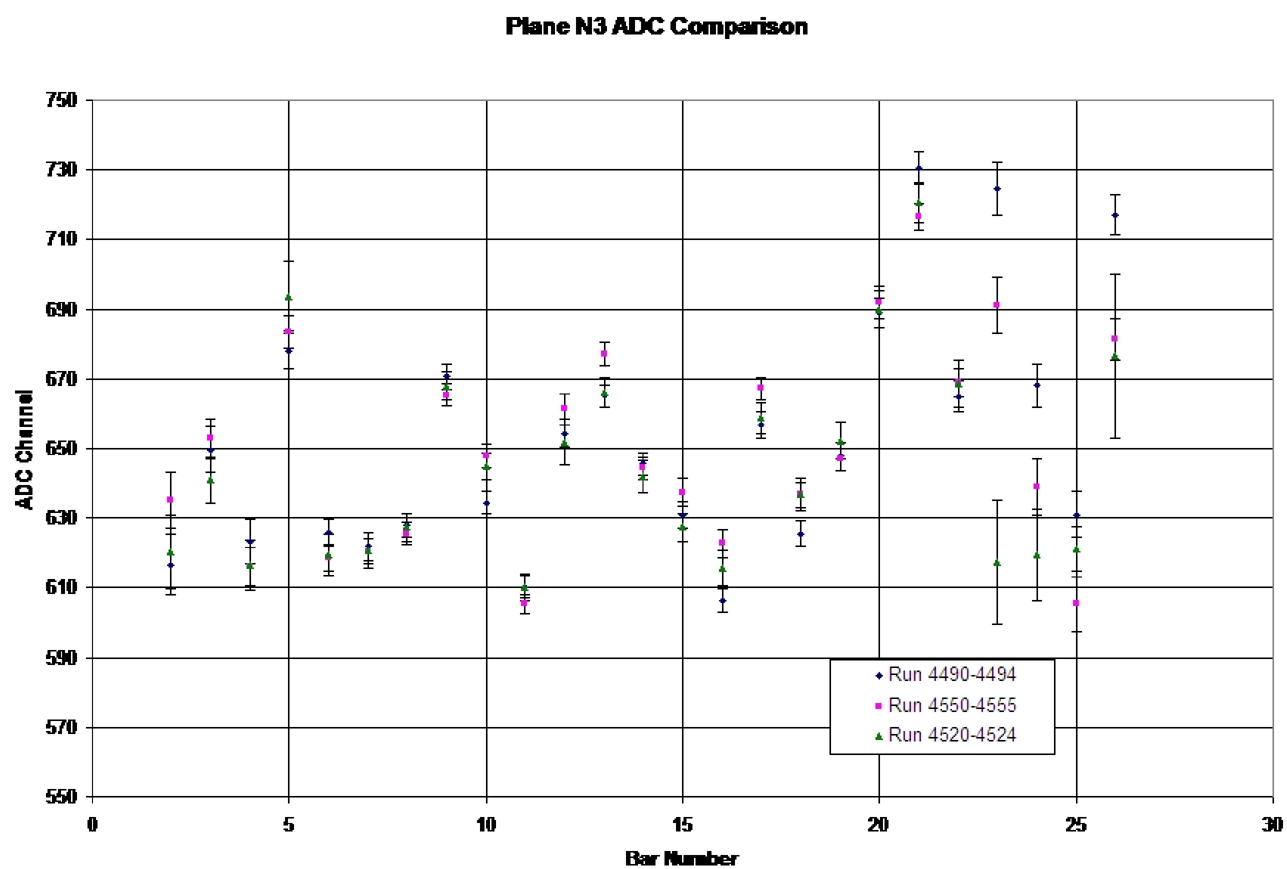

Figure 63: ADC channel response of Protons in N3 plane

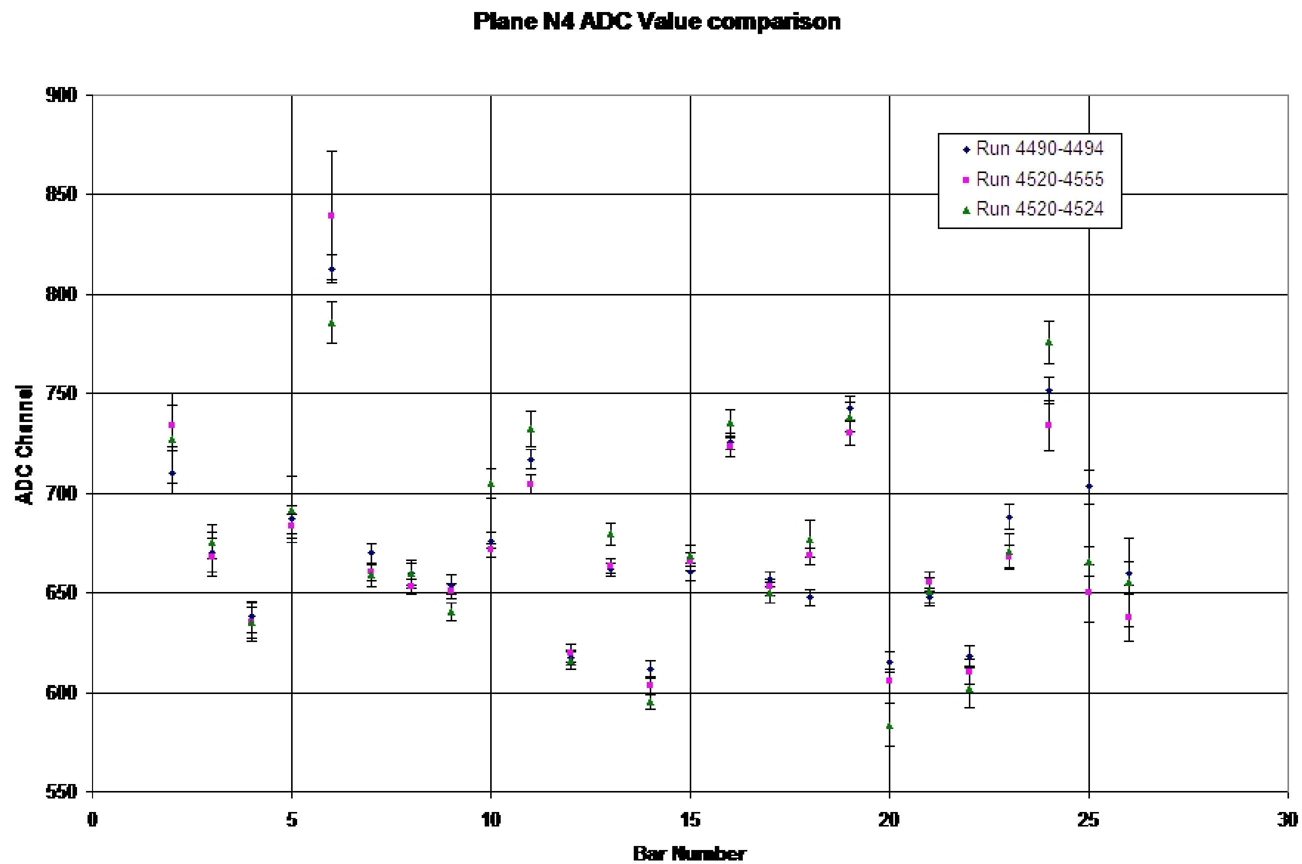

Figure 64: ADC channel response of Protons in N4 plane

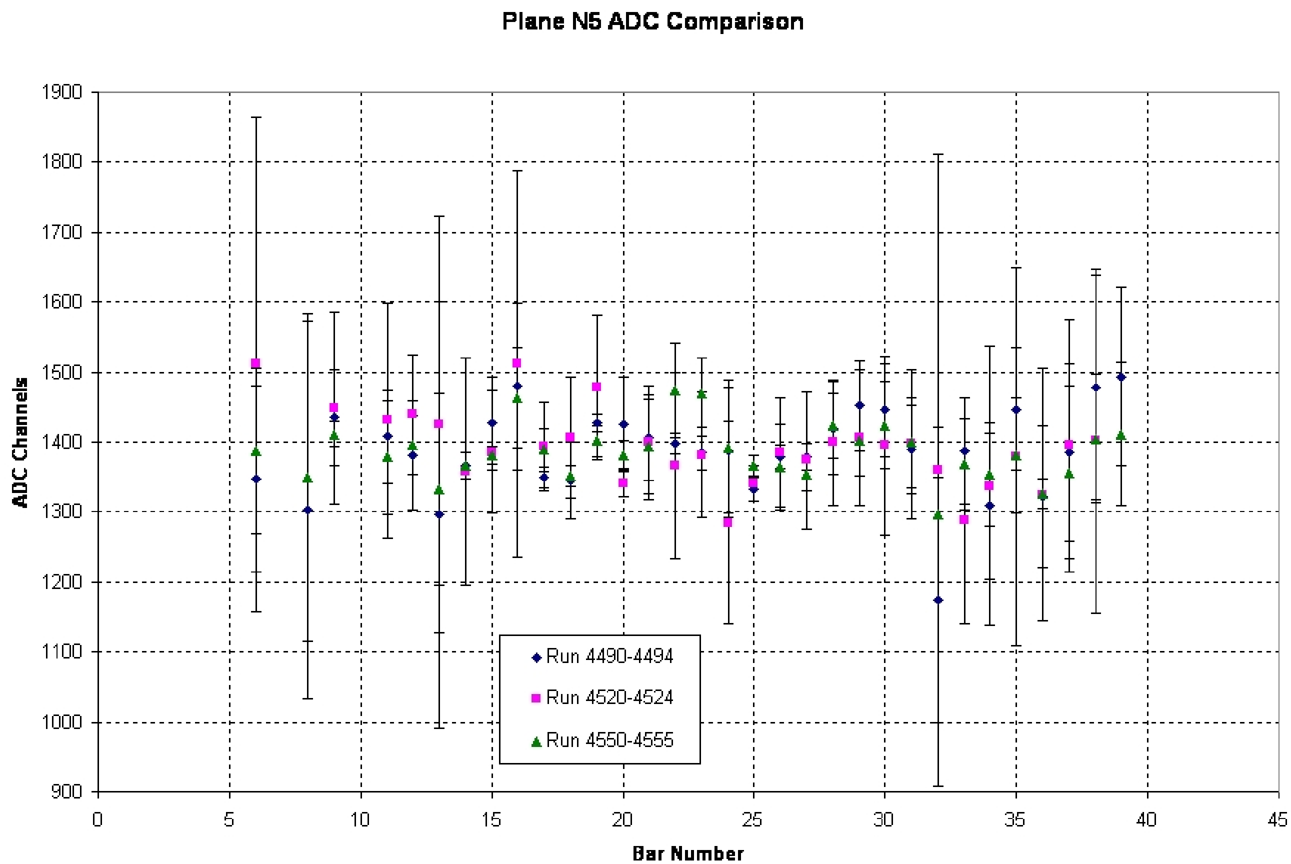

Figure 65: ADC channel response of Protons in N5 plane

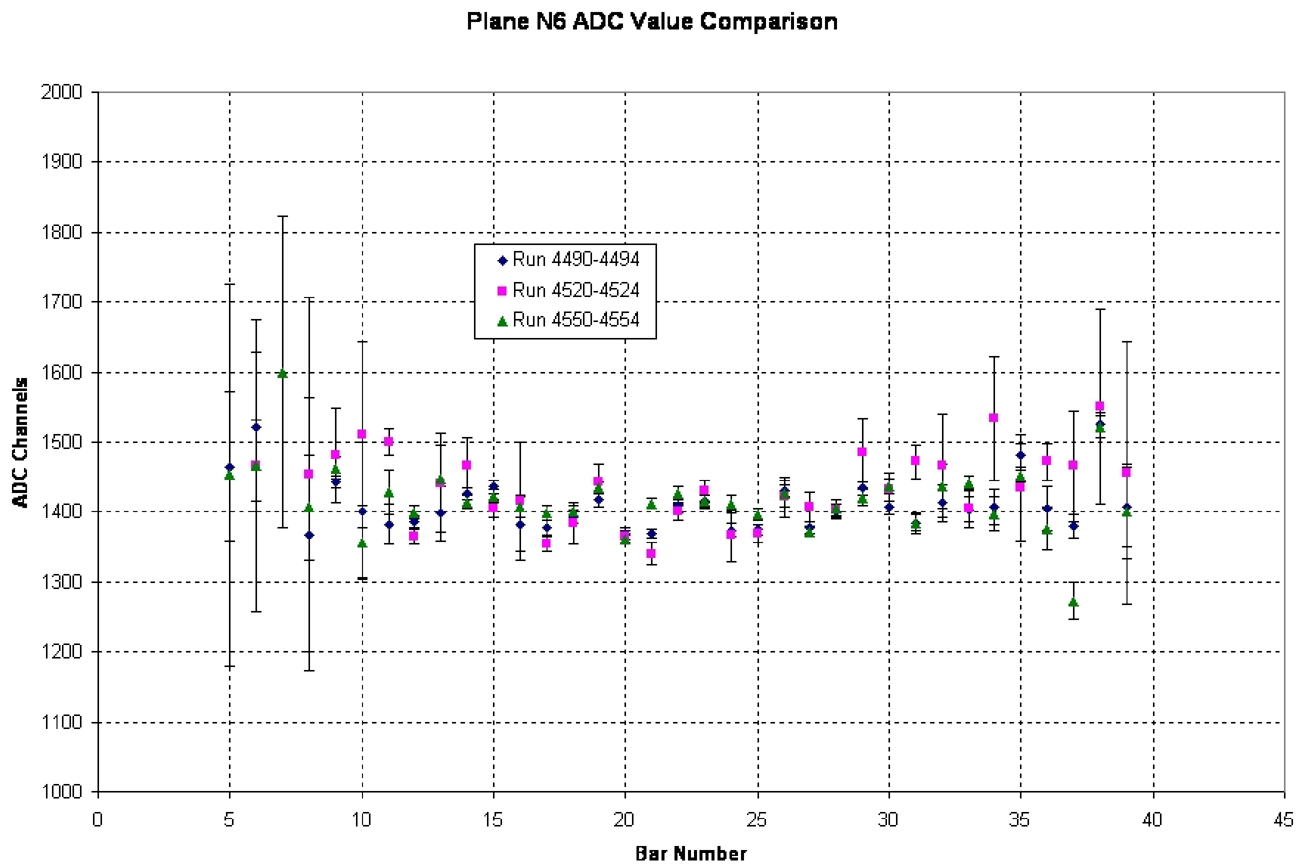

Figure 66: ADC channel response of Protons in N6 plane

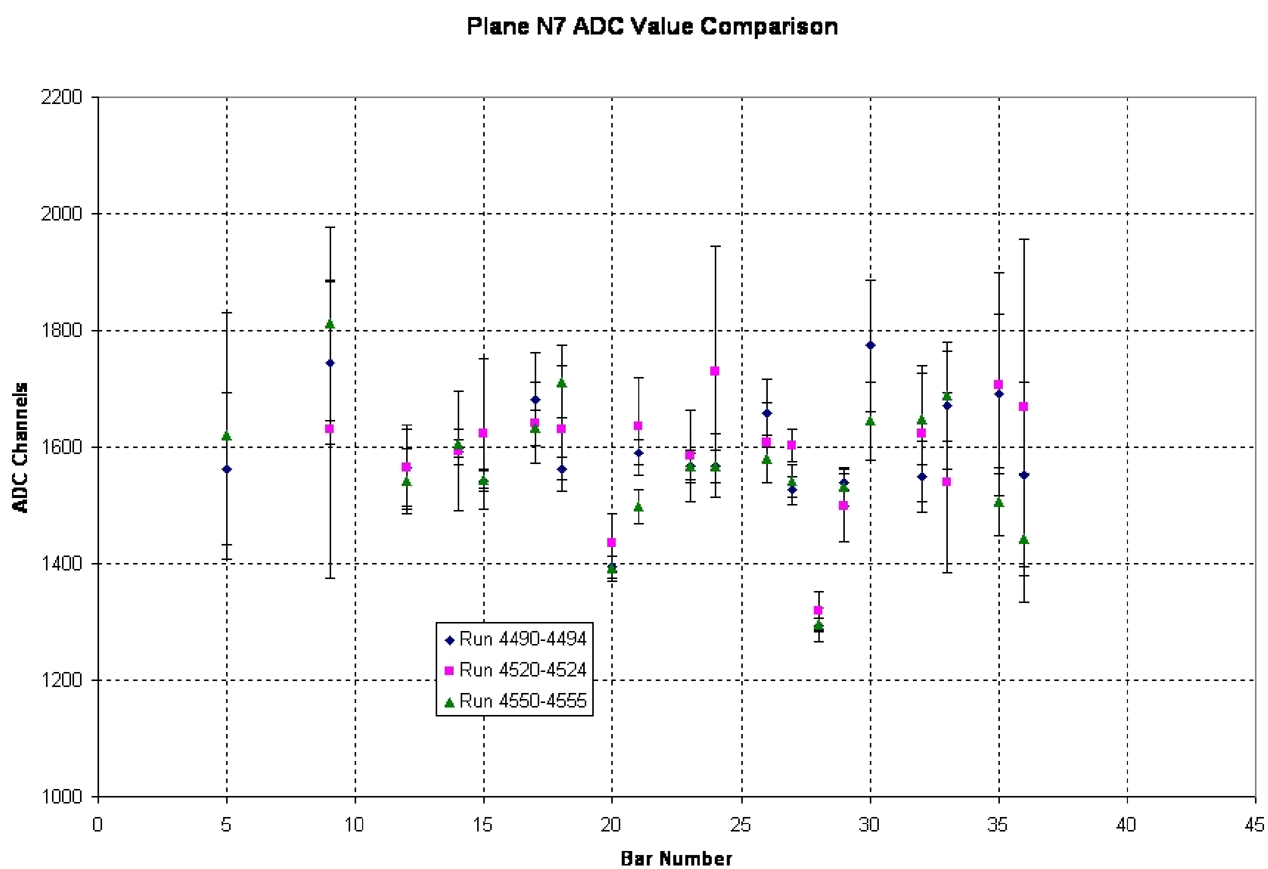

Figure 67: ADC channel response of Protons in N7 plane

8.3.2 TIME OF FLIGHT FROM TARGET TO N1 PLANE

Using long tracks created by protons in the Neutron Arm also allows us to check and calibrate the time of flight (TOF) of a proton from the target to the N1 plane in the Neutron Arm. To get this value we need to use the time the an electron took to hit the scintillator in BigBite and compare it to the time a proton hits the Neutron Arm. The Neutron Arm time is measured in ns relative to the Level One Accept (L1A) signal provided by one of the TDCs in the Neutron Arm. BigBite's trigger time uses a different common signal for its TDC and ADC digitization, which we call BBtrig. A separate TDC was used to record the difference between the Neutron Arm's, ND$_{recordedtime}$, and BigByte's time, called ctimeL1A. To obtain the TOF for a neutron/proton we then use the recorded time of the Neutron Arm, BigByte's trigger, and the ctimeL1A in the following fashion.

$$ND_{recordedtime} = ND_{realtime} - L1A \tag{29}$$

$$0.05 * ctimeL1A(ns) = L1A - BBtrig \tag{30}$$

$$\begin{aligned} NDtimerelativeBB &= ND_{realtime} - BBtrig \\ &= ND_{realtime} - L1A + (L1A - BBtrig) \\ &= ND_{recordedtime} + (L1A - BBtrig) \\ &= ND_{recordedtime} + 0.05 * ctimeL1A \end{aligned} \tag{31}$$

The ctimeL1A value is multiplied by 0.05 because this TDC uses a 50ps/channel. Figure 68 shows the plot of the proton TOF from the target. This plot has no corrections applied thus we see a bend in the plot reflecting the differences in path

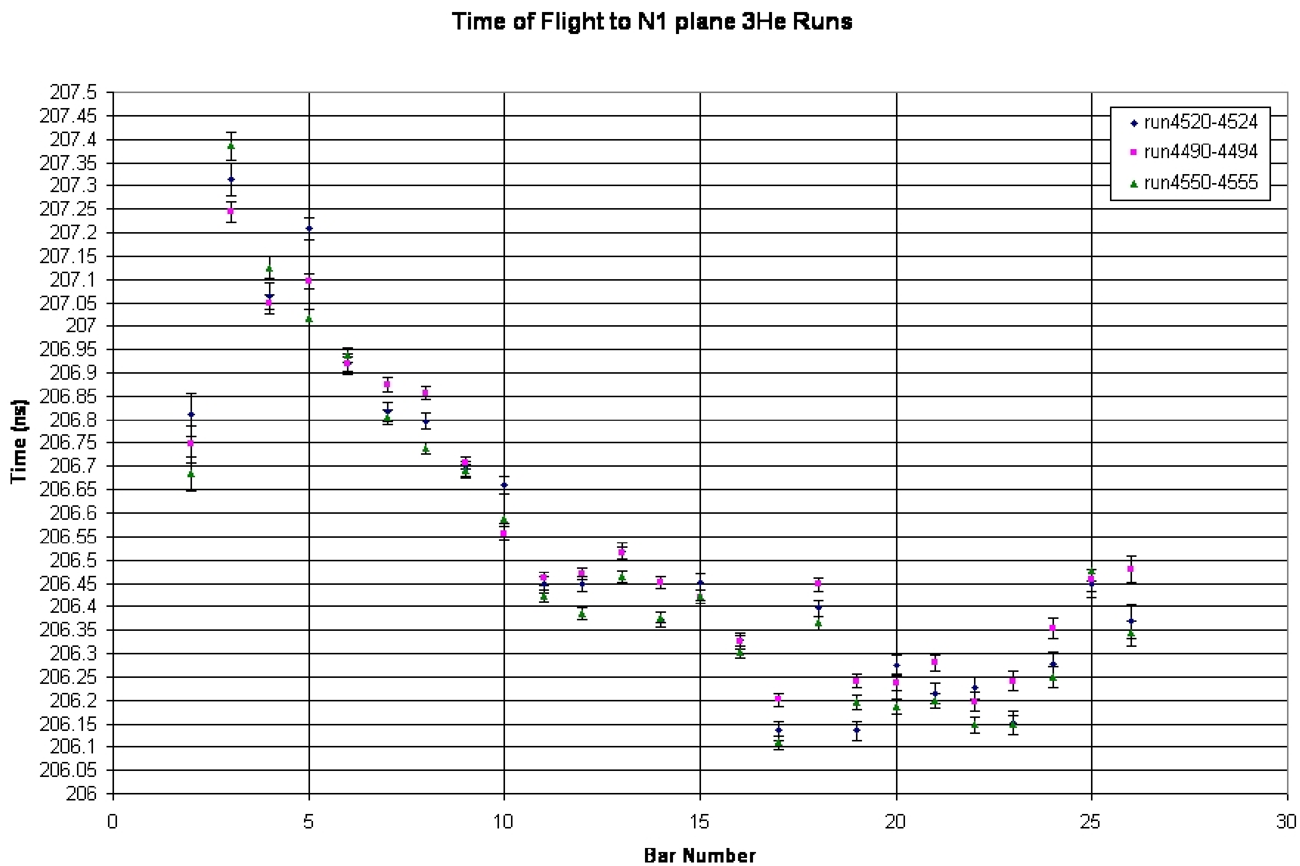

Figure 68: Time of Flight from target to N1, with no path length or RF correction

from the target to the different scintillator bars in the N1 Plane.

Because BigBite bends the electron's trajectory, the time the electron takes to hit BigBite needs to be corrected. Instead of correcting for the time of the electron in BigBite we can use the RF signal provided by the beam so that we can remove some of the dependence on BigBite. The beam sends packets of electrons every 2ns, we can use the time from BigBite to predict which electron bunch has hit the detector. Figure 69 shows the TOF with the RF correction included. As we can see it is only a small effect.

The shape of the times in the plots of figures 68 and 69, shows a small curvature due to the path length differences the proton takes. It takes a longer time for the proton to reach the scintillator bars at the top and bottom of the Neutron Arm. Correcting this we should be able to remove this curvature. In figure 70 is a plot with the path length correction added.

Finally we add an offset to set all the values to zero, so that we can compare the different sets of data from the beginning and end of kinematic 4, and can be found in figure 71. The differences in the TOF between the runs at the beginning to the end of kinematic 4 are with 50ps of each other excluding the points at the very top and bottom of the detector.

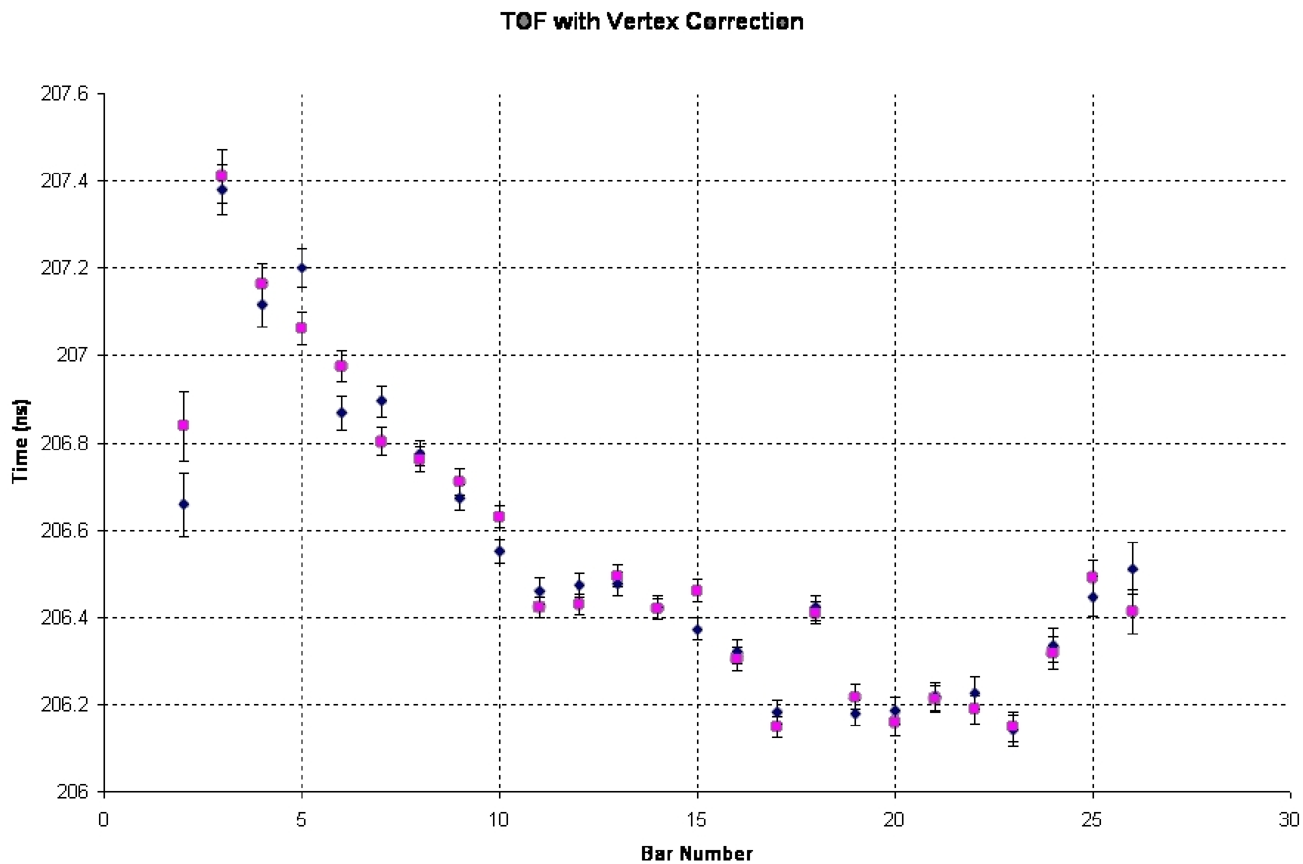

Figure 69: Time of Flight from target to N1 with RF corrections.

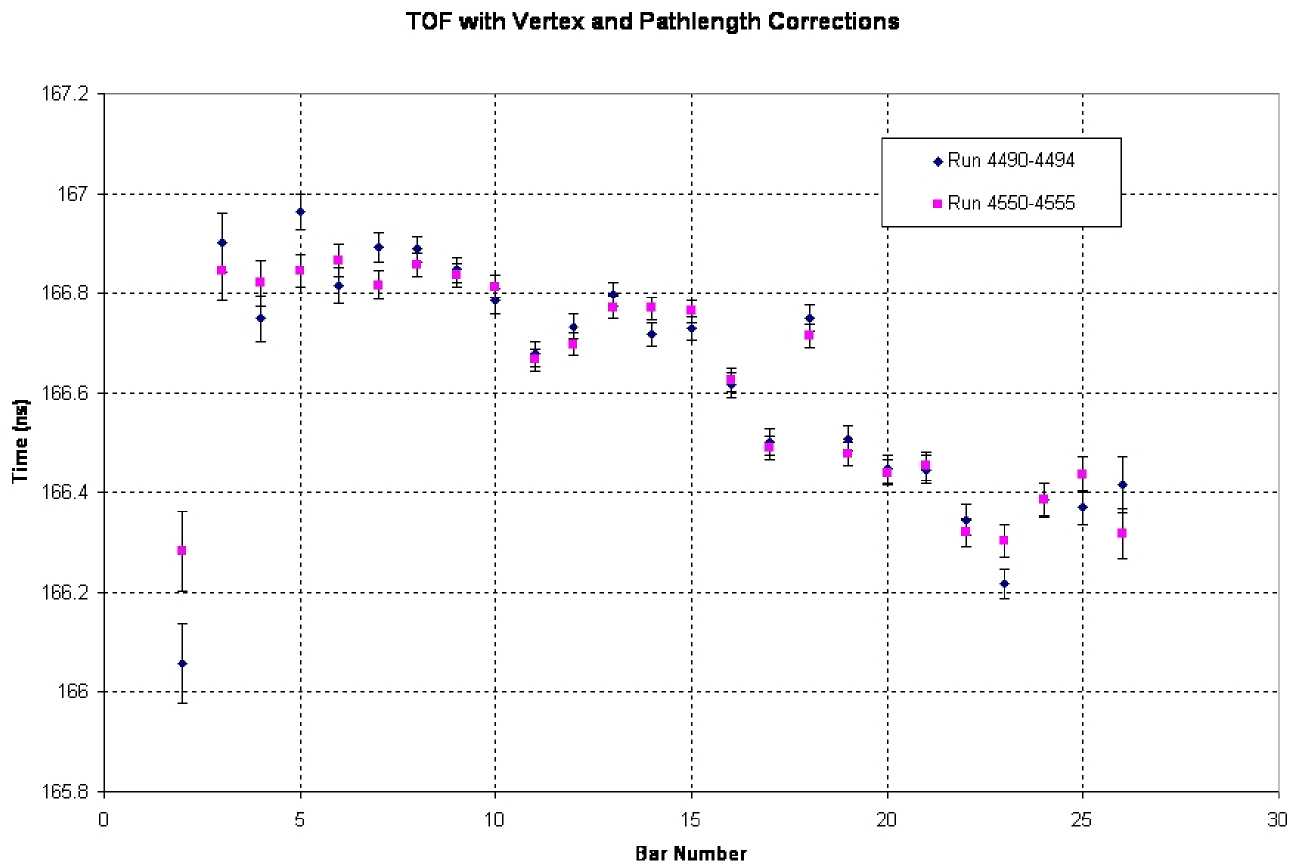

Figure 70: Time of Flight from target to N1 with RF and path length corrections.

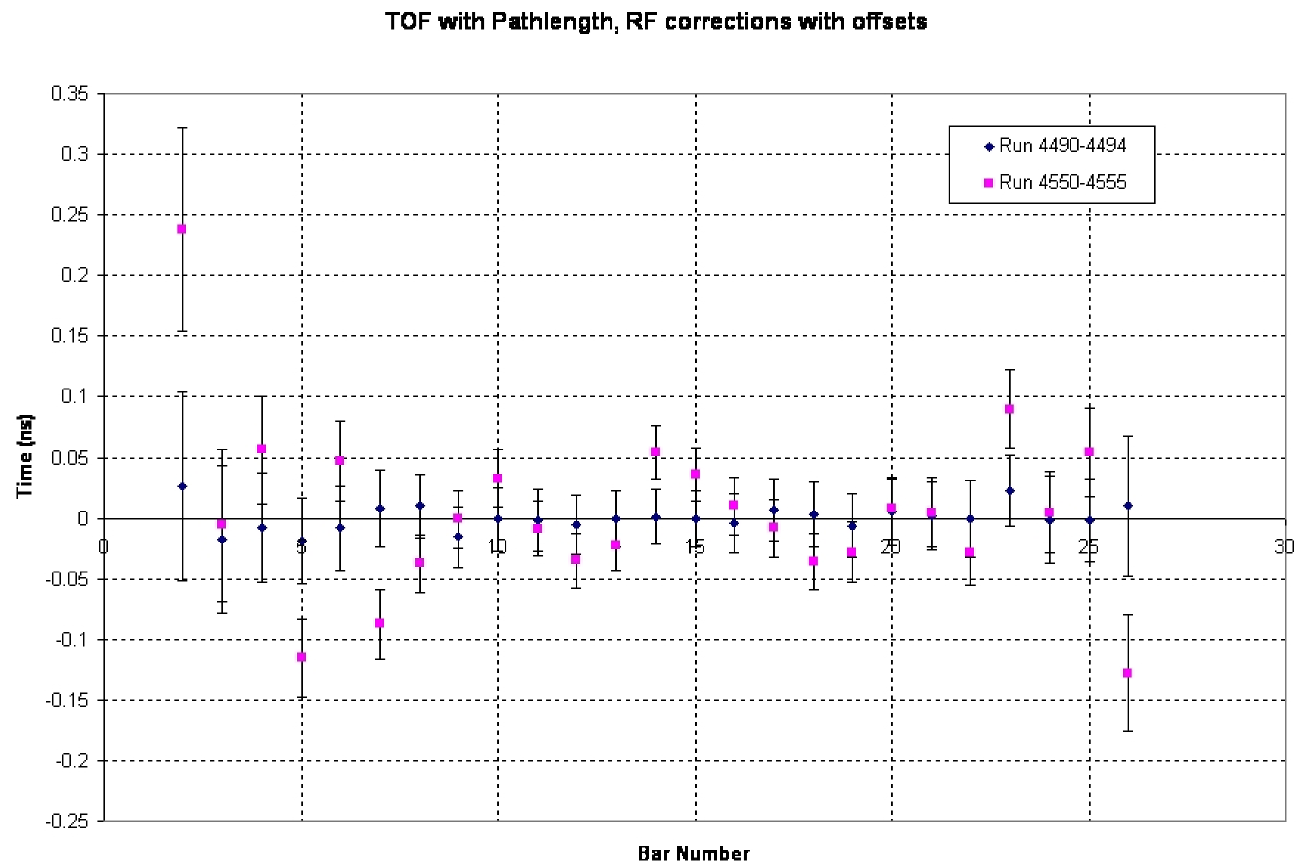

Figure 71: Time of Flight from target to N1 with RF and path length corrections with offset added.

8.4 KINEMATIC 3

Kinematic 3 as explained before is the kinematic where the Q^2 value is 3.4 GeV^2 and will give us the highest value of G_E^n to date. The runs used here to represent kinematic 3 is run 4290 through 4303. Again we will apply the same type of cuts on the data as we did with kinematic 4 data. The cut on Pdiff is shown in figure 72, and the resulting missing mass squared (W^2) is shown in figure 73. In kinematic 3 we get a lot more non-elastic and non-electron events, which subdues the elastic peak, as can be seen in the Pdiff and W^2 plots.

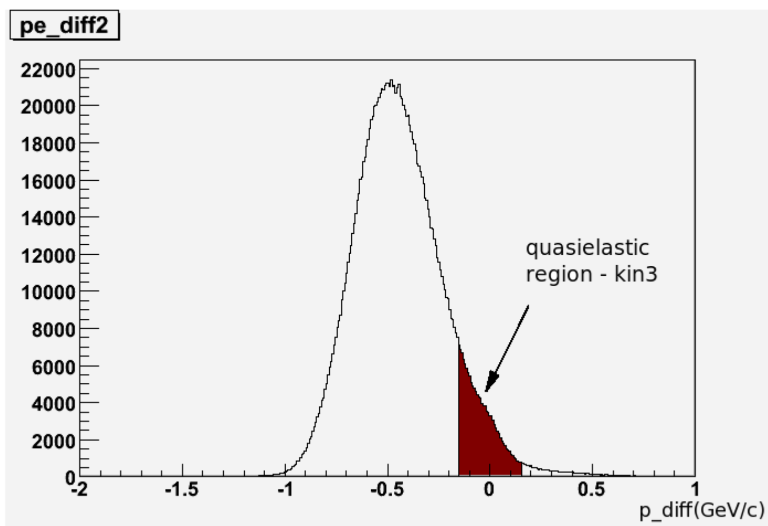

Figure 72: Selection on Pdiff for quasi-elastic events.

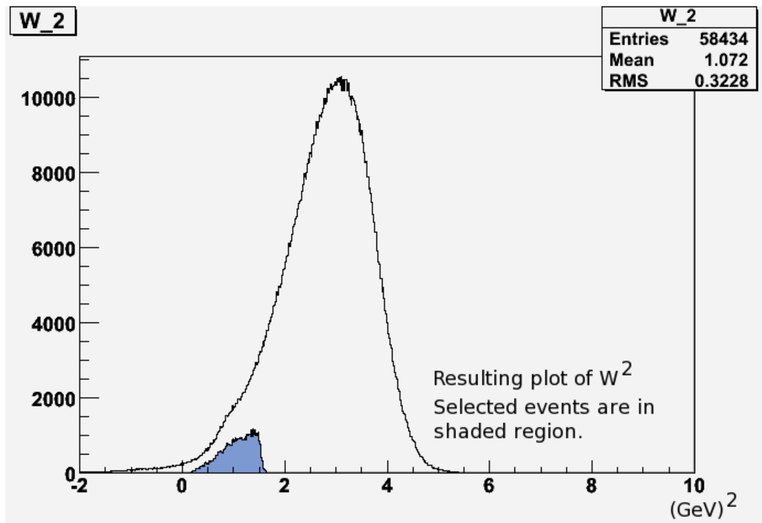

Figure 73: Resulting plot of W^2 of selected protons

We plot the intraplane time of flight by looking at long tracks created by protons in kinematic 3. In order to compare the results from kinematic 3 to kinematic 4 we apply the offsets from kinematic 4 directly to the proton events in kinematic 3. Figure 74 shows all of the bars in kinematic 3 without offsets applied and figure 75 shows all the bars with kinematic 4 offsets applied. A constant is added to the values in figure 75 for clarity purposes.

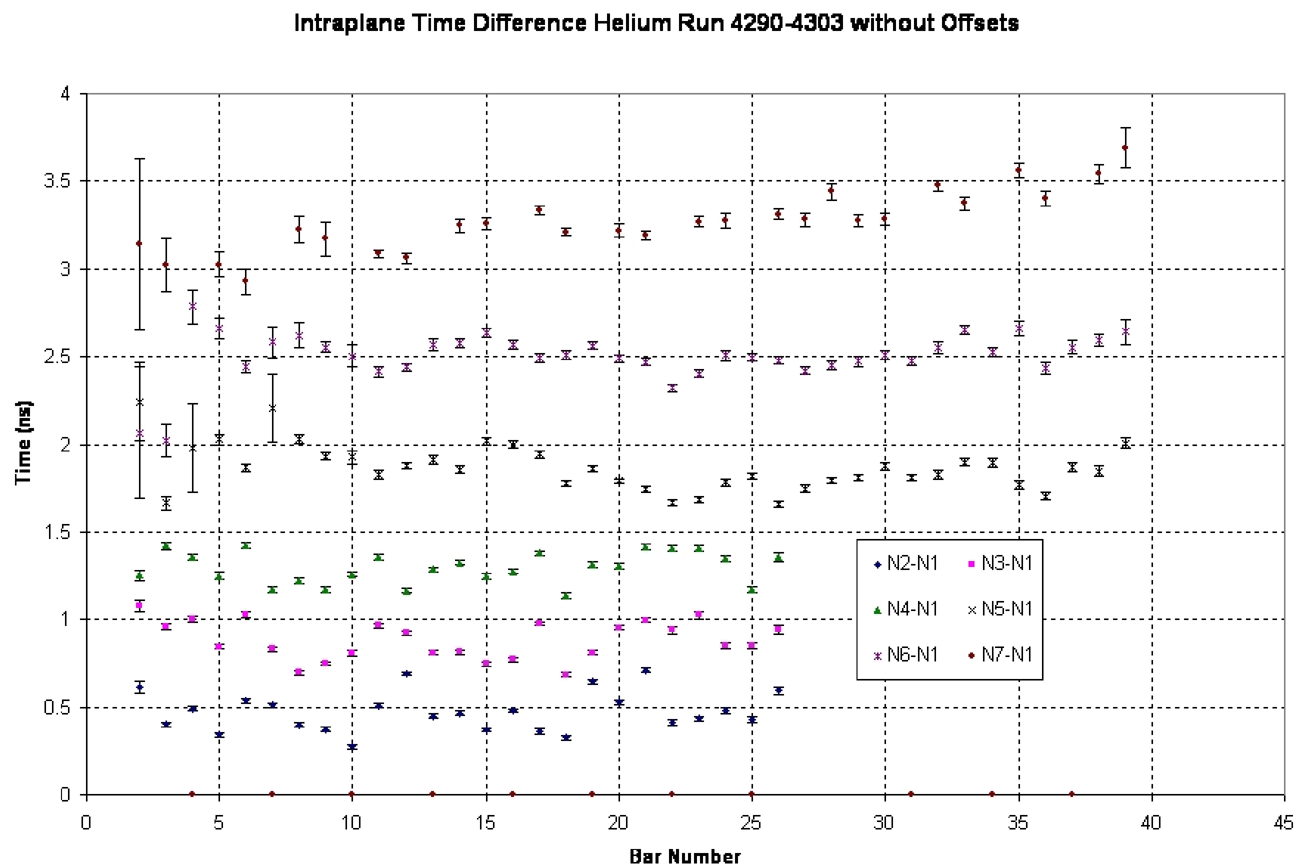

Figure 74: Intraplane time difference for kin3 with no offsets applied. Constant is added to the values to separate the different planes.

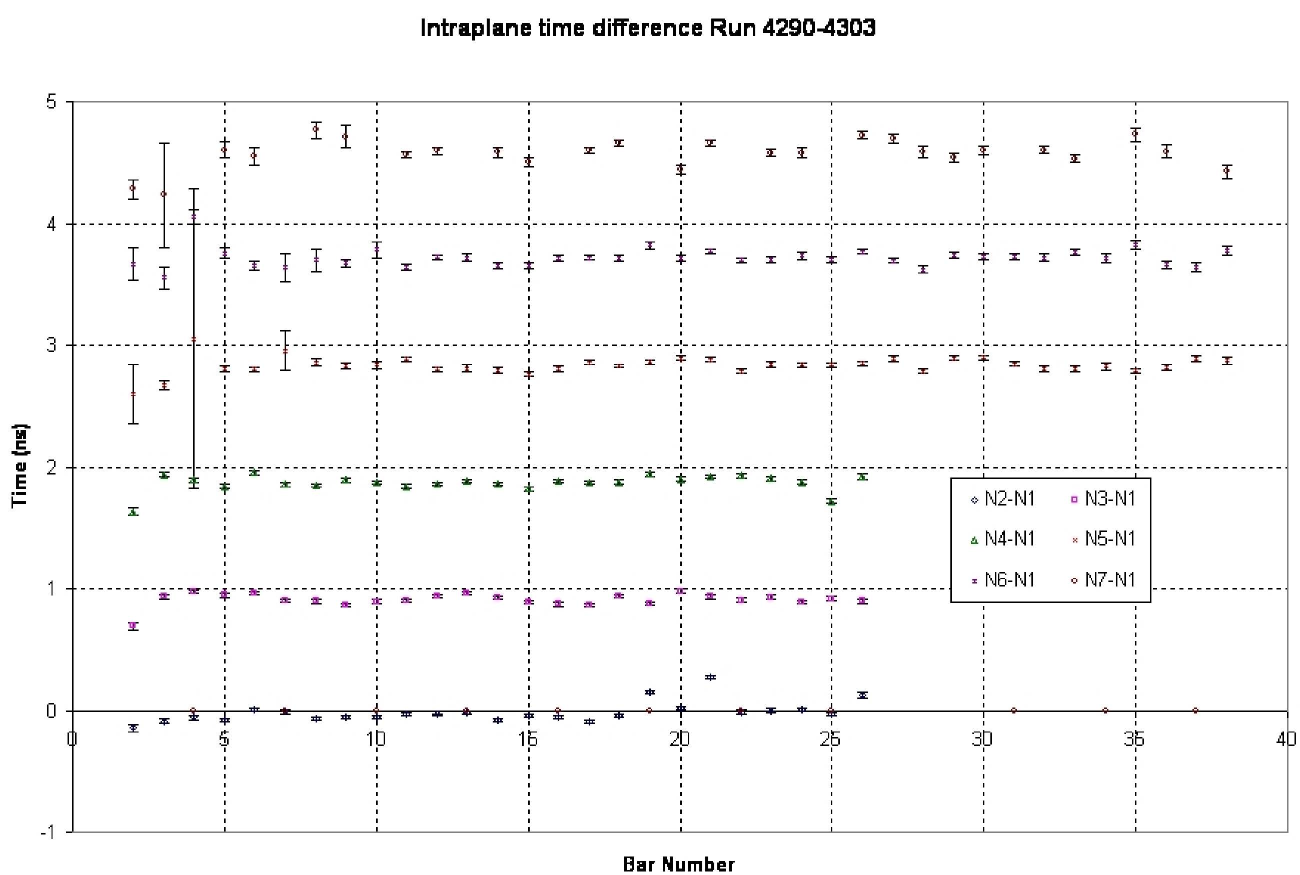

Figure 75: Intraplane time difference with offsets from kin4 applied to kin3. Constant is added to the values to separate the different planes.

In figures 76 through 81 we compare the intraplane time of flight from kinematic 4 to kinematic 3, both with offsets from kinematic 4 applied. What we see here is that in the kinematic 3 data the intraplane time of flight is less then kinematic 4 which shows the difference in momentum of the protons, since kinematic 4 had an electron beam energy of 2.079 GeV^2 and kinematic 3 had an electron beam energy of 3.290 GeV^2.

Figures 82 to 84 shows time of flight from the target to the N1 plane for kinematic 3 compared to the time of flight for kinematic 4. Figure 82 shows the time of flight with the RF corrections, figure 83 shows the pathlength and RF corrections added, and finally figure 84 shows the time of flight offsets from kinematic 4 added along with the pathlength and RF corrections. The differences in the time of flight, about 4ns, reflects the fact that the Neutron Arm is moved away from the target by about 2.71 meters from kinematic 4.

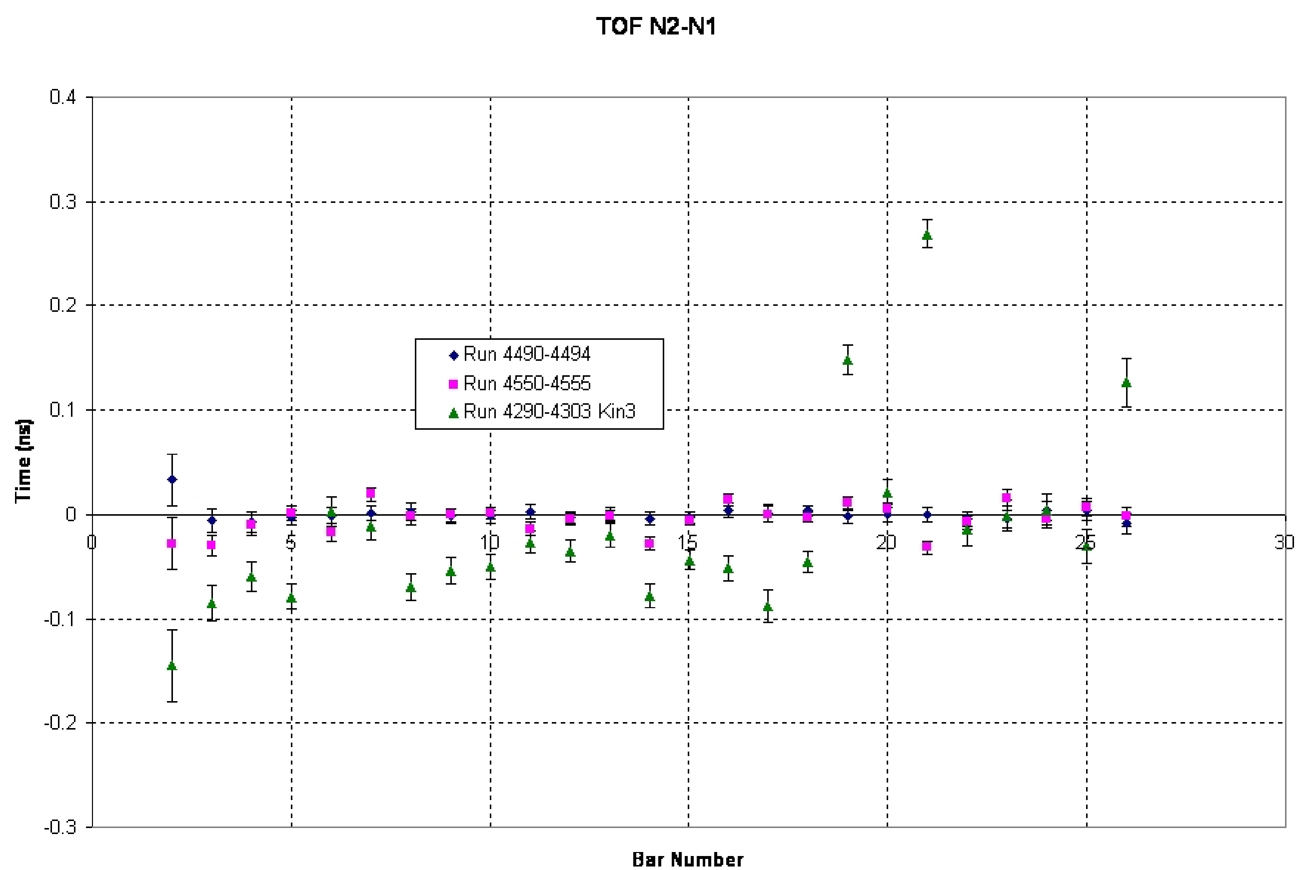

Figure 76: Intraplane time difference N2-N1 plane using helium offset from kin4 applied to kin3.

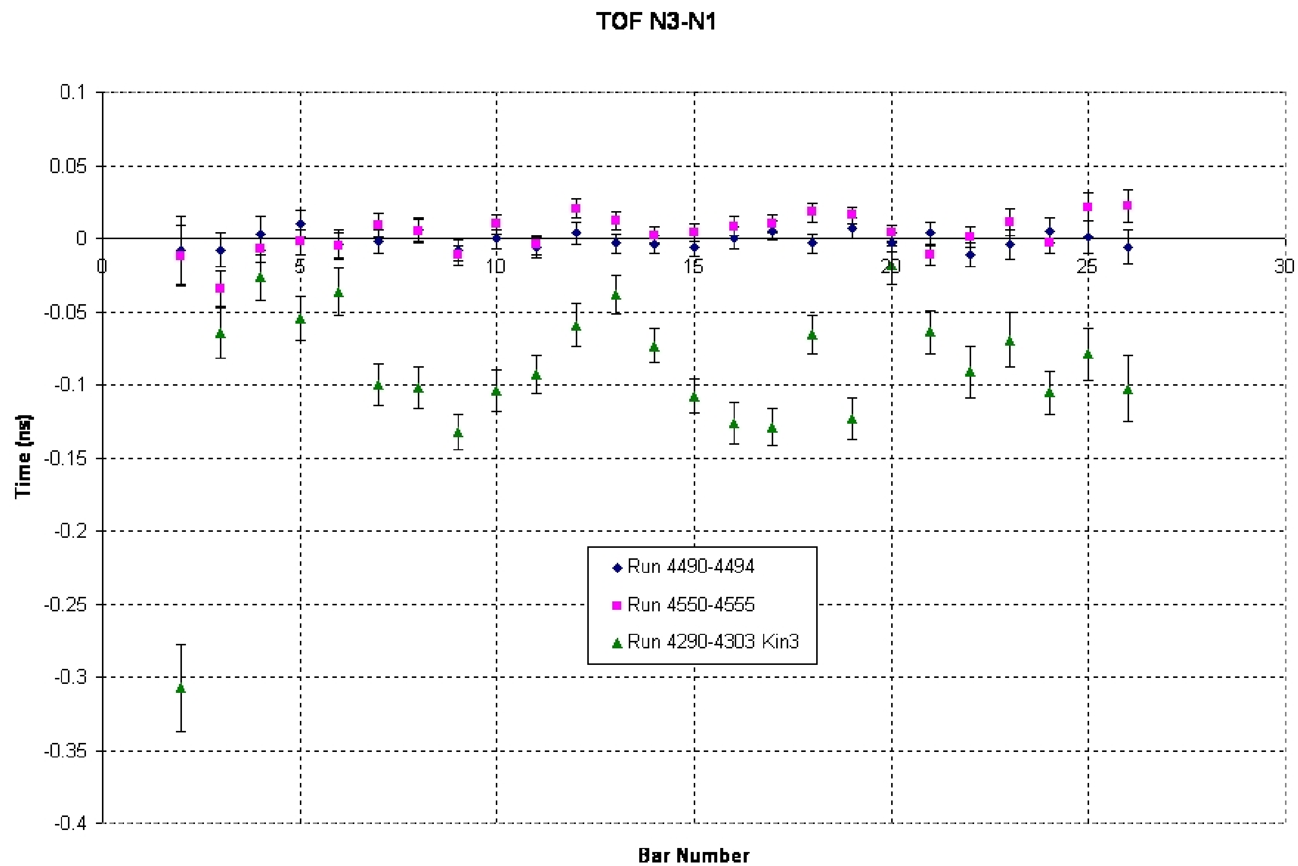

Figure 77: Intraplane time difference N3-N1 plane using helium offset from kin4 applied to kin3.

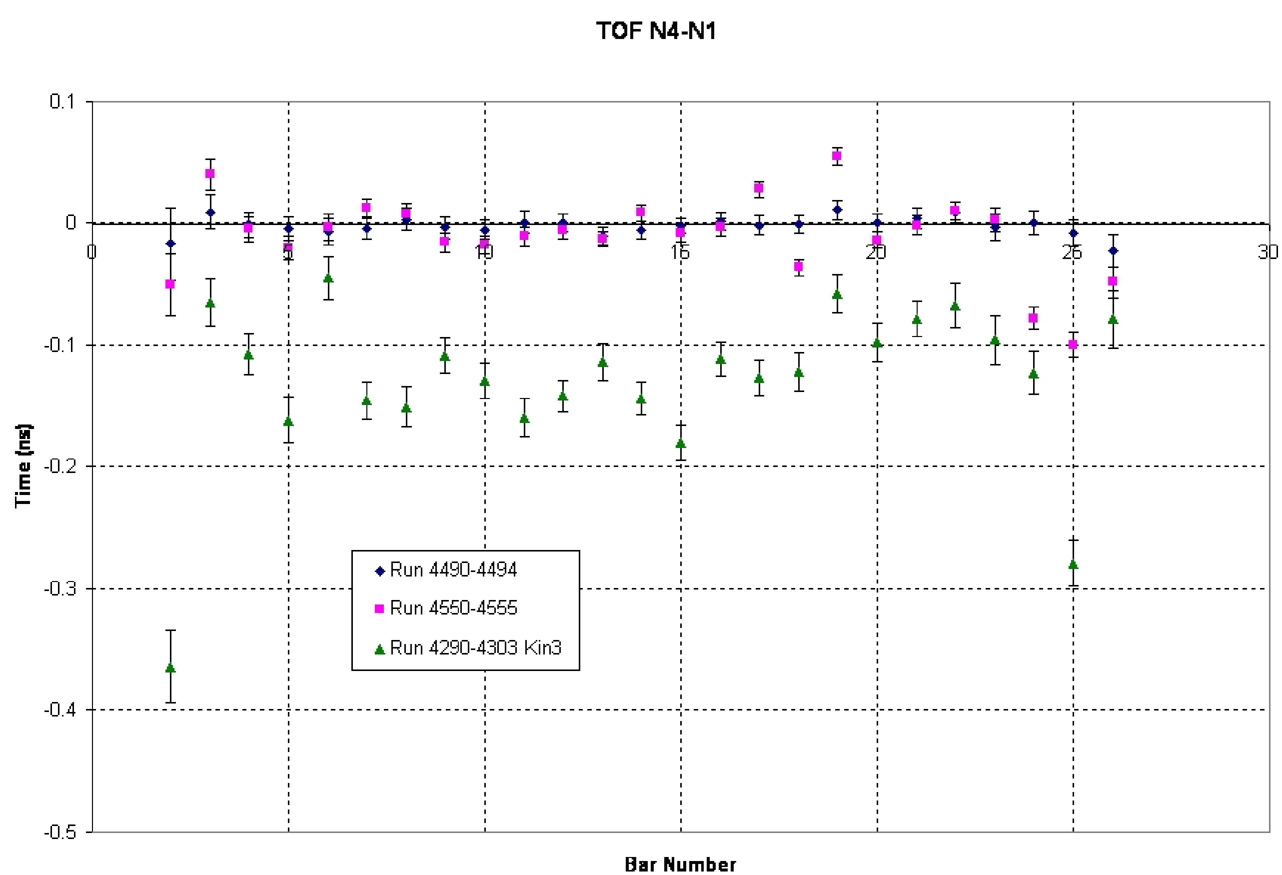

Figure 78: Intraplane time difference N4-N1 plane using helium offset from kin4 applied to kin3.

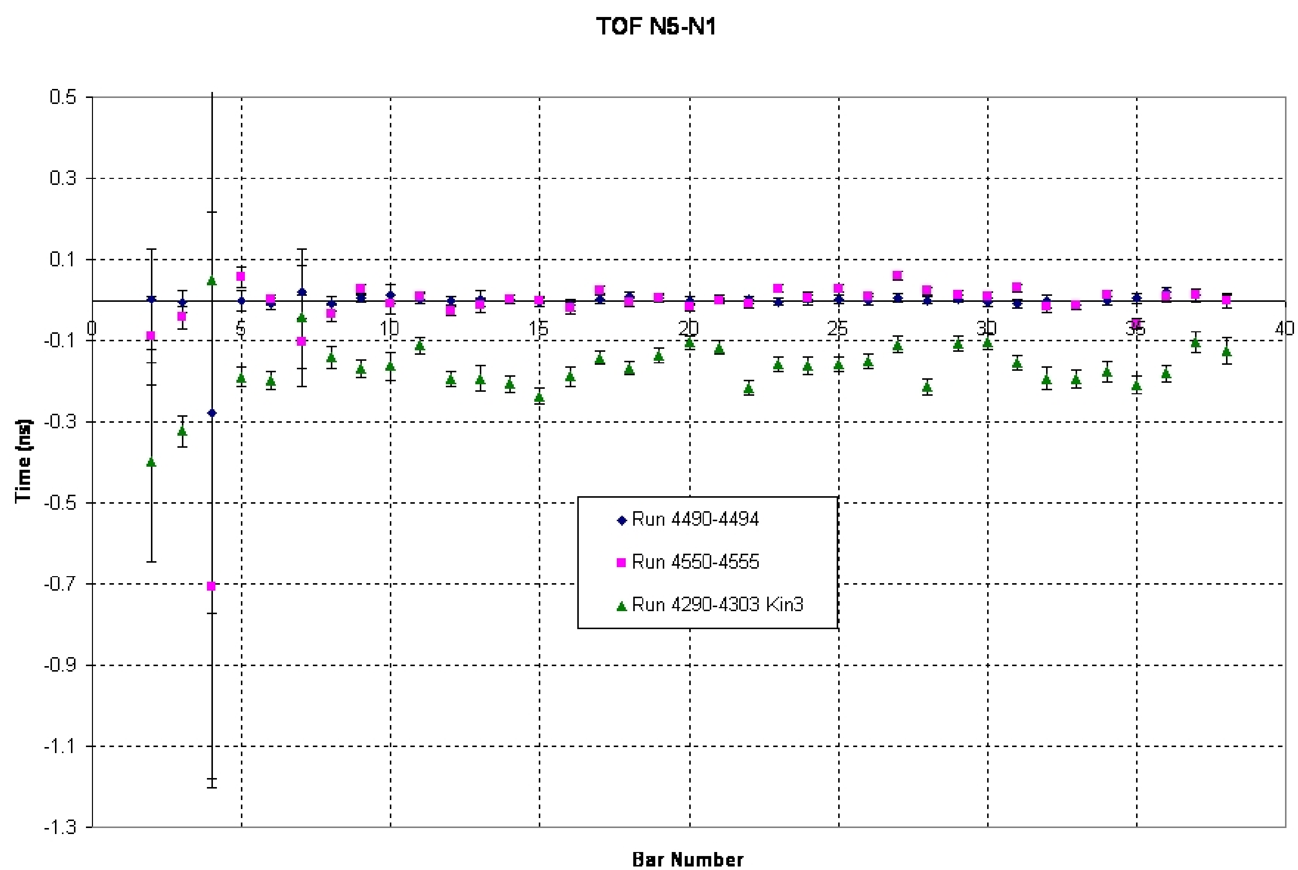

Figure 79: Intraplane time difference N5-N1 plane using helium offset from kin4 applied to kin3.

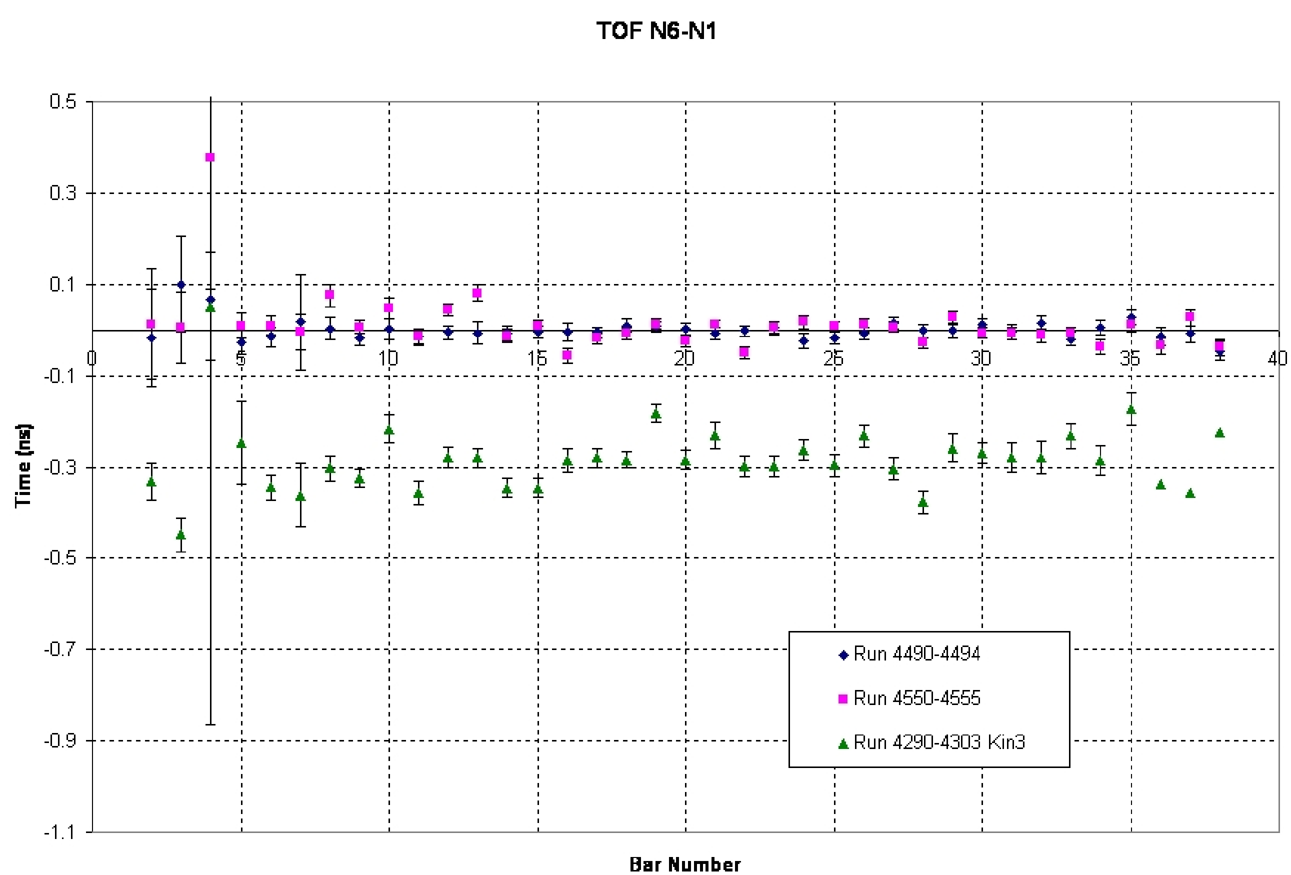

Figure 80: Intraplane time difference N6-N1 plane using helium offset from kin4 applied to kin3.

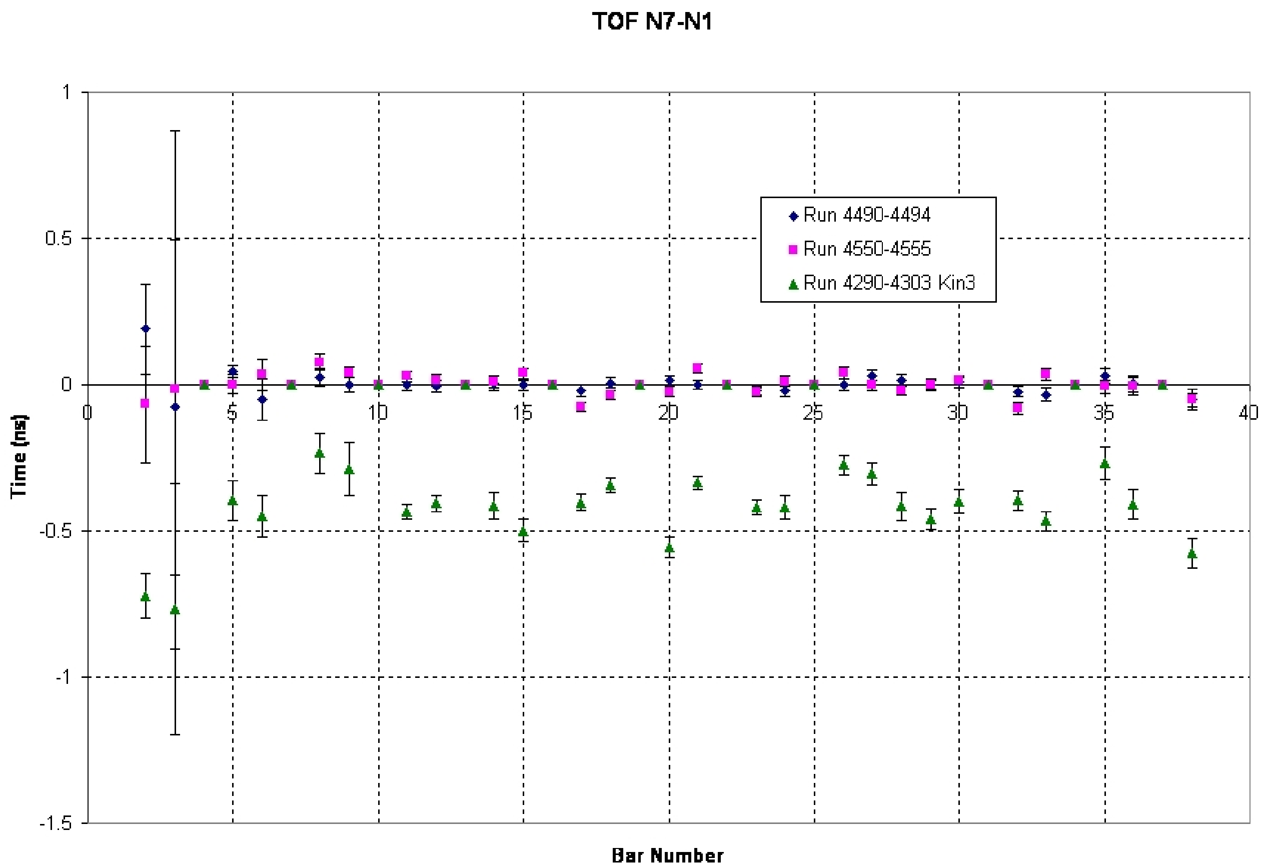

Figure 81: Intraplane time difference N7-N1 plane using helium offset from kin4 applied to kin3.

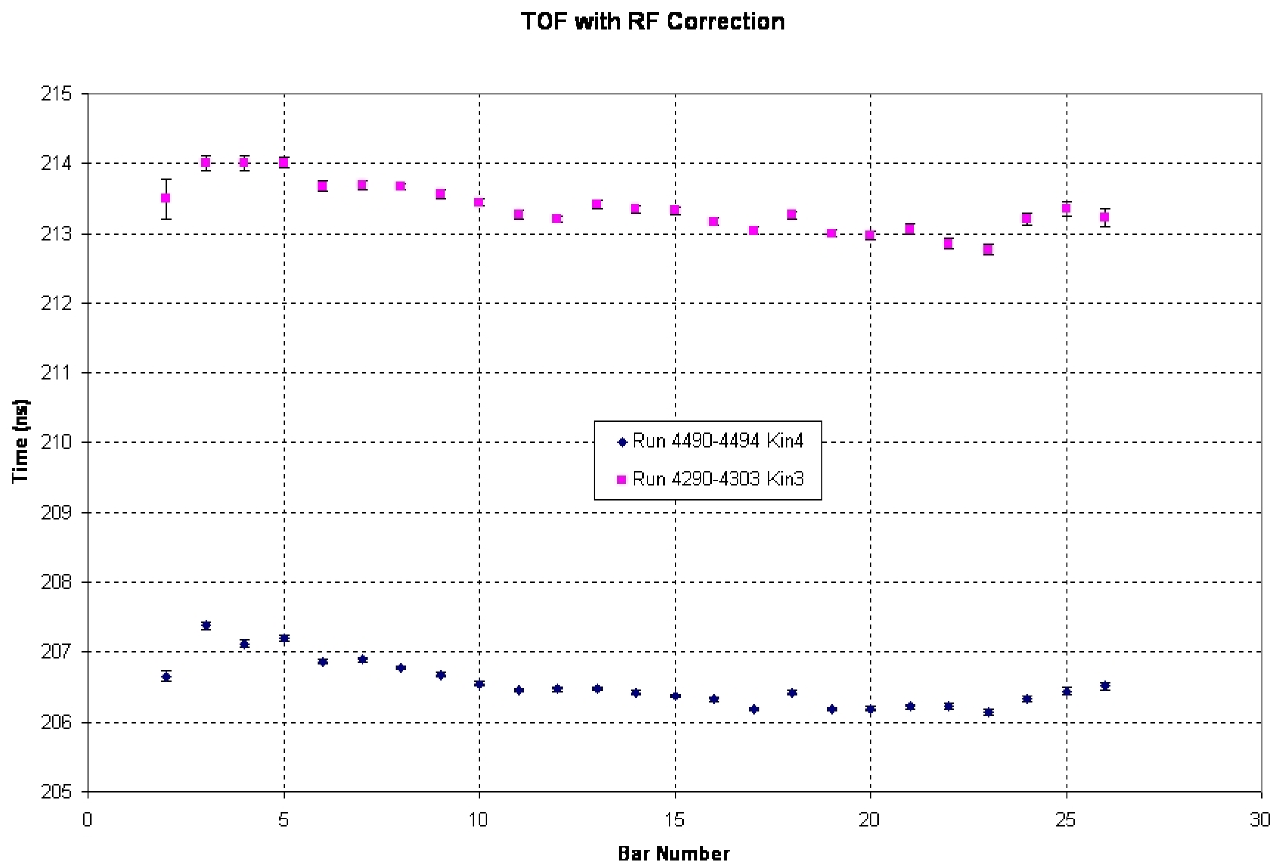

Figure 82: Time of Flight from target to N1 with RF corrections for kin3.

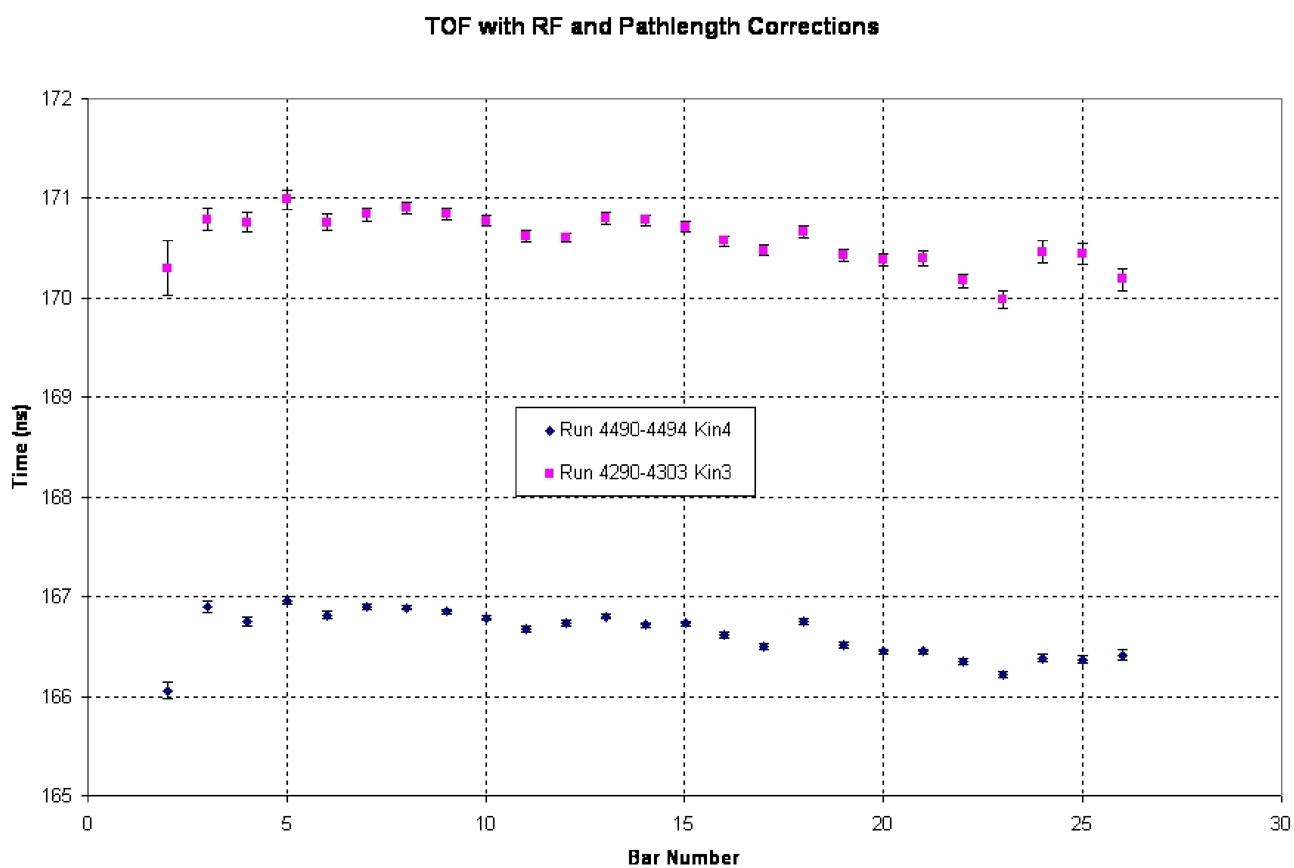

Figure 83: Time of Flight from target to N1 with RF and pathlength corrections for kin3.

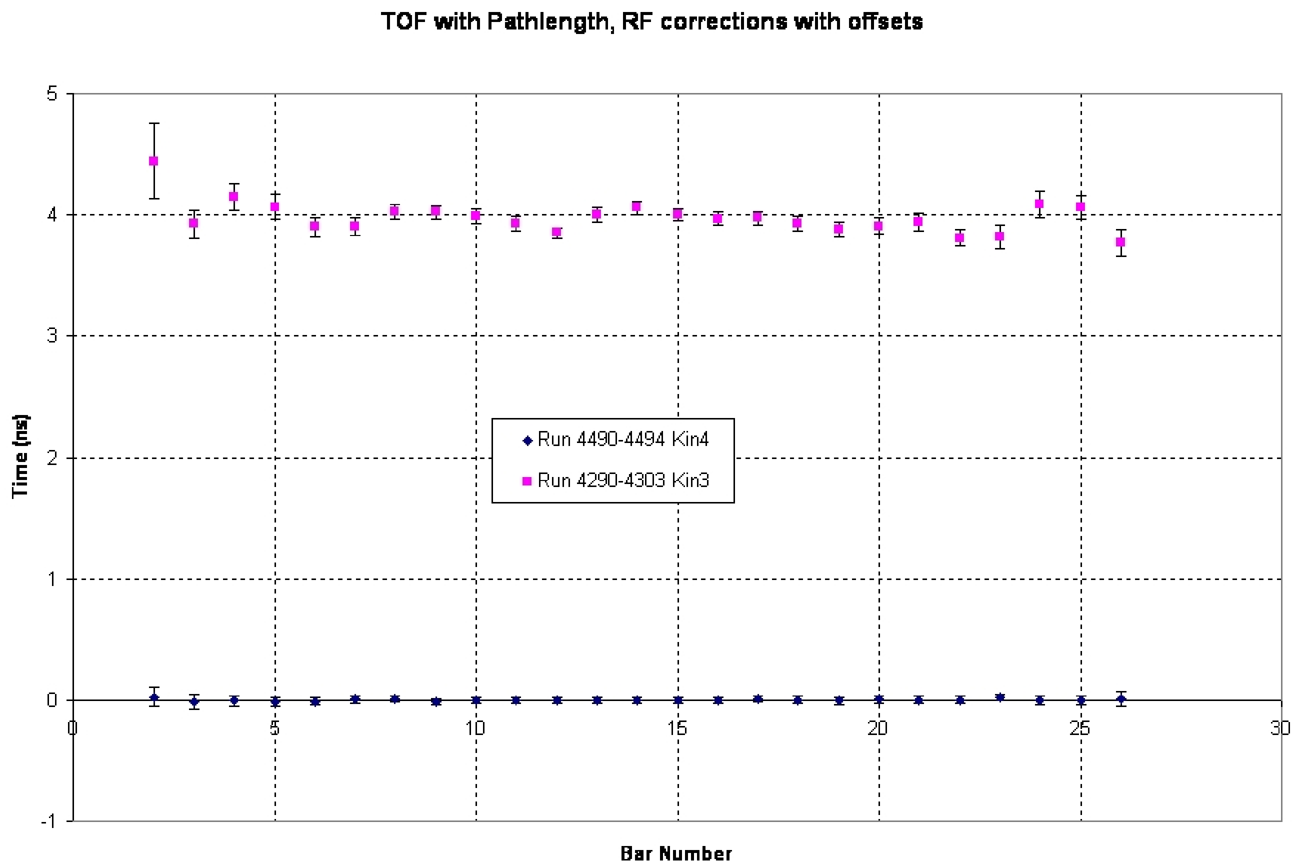

Figure 84: Time of Flight from target to N1 with RF and path length corrections with offset from kin4 added.

9 CONCLUSION

The study of the Neutron Arm shows that using long tracks traversing through the detector is an extremely useful tool. By using vertical tracks from cosmics we can calibrate the PMT responses allowing us to convert ADC channels to a corresponding energy value. On the other hand using long tracks in the horizontal direction provides us with the ability to calibrate the timing of protons traversing from the target through multiple planes of the Neutron Arm.

Looking at the different data sets at the beginning and end of kinematic 4 we see that the detector was very stable since the time fluctuations are on the order of 100ps which is about the limit of resolution of the scintillator bars and well within the required resolution of 300ps as stated in the proposal. The variances in the amplitude of the PMTs show that they are about 5% and about 10% for bars at the very top and bottom of the detector.

Comparing kinematic 3 to kinematic 4 we notice that the intraplane time of flight is generally smaller then in kinematic 4 due to the differences in proton momentum, whereas the time of flight from the target to the N1 plane gives a time that is about 4ns larger then in kinematic 4 due the different position of the Neutron Arm. Due to this fact separate offsets will probably have to be applied to the different kinematic points.

REFERENCES

[1] T. W. Donnelly and A. S. Raskin. Considerations of polarization in inclusive electron scattering from nuclei. *Annals of Physics*, 169:247, 1986.

[2] M. K. Jones et al. G_{E_p}/G_{M_p} ratio by polarization tranfer in $\overrightarrow{e}p \longrightarrow \overrightarrow{e}p$. *Physical Review Letters*, 84:1398, 2000.

[3] O. Gayou et al. Measurement of G_{E_p}/G_{M_p} in $\overrightarrow{e}p \longrightarrow \overrightarrow{e}p$ to Q^2=5.6 (GeV/c)^2. *arXiv:nucl-ex/0111010v2*, 2001.

[4] D. Rohe et al. Measurement of the neutron electron form factor G_E^n at $0.67(GeV/c)^2$ via $^3He(e,e'n)$. *Phys. Rev. Lett.*, 83:4257, 1999.

[5] M. Meyerhoff et al. First measurement of G_E^n in the exclusive quasielastic scattering of polarized electrons from polarized ^3He. *Phys. Lett. B*, 327:201, 1994.

[6] M. Ostrick et al. Measurement of the neutron electric form factor G_E^n in the Quasifree $^2H(e,e'n)p$ reaction. *Phys. Rev. Lett.*, 83:276, 1999.

[7] T. Eden et al. Electric form factor of the neutron from the $^2H(e,e'n)^1H$ reaction at $Q^2 = 0.255(GeV/c)^2$. *Phys. Rev. C*, 50:R1749, 1994.

[8] Gerald A. Miller. Charge density of the neutron. *arXiv:nucl-th/0705.2409v2*, 2007.

[9] M. N. Rosenbluth. High energy elastic scattering of electrons on protons. *Physical Review*, 79:615, 1950.

[10] T. W. Donnelly and A. S. Raskin. Polarization in coincidence electron scattering from nuclei. *Annals of Physics*, 191:78, 1989.

[11] Bogdan Wojtsekhowski et al. Proposal for Measurement of the Neutron Electric Form Factor G_E^n at high Q^2. *Jefferson Laboratory*, 2001.

[12] J.R.M. Annand et al. Large position sensitive plastic scintillation detectors. *Nuclear Instruments and Methods in Physics Research*, A262:329, 1987.

[13] Dimitri Nikolenko. Marking counters for Neutron Arm. *Jefferson Laboratory*, 2005.

[14] Aiden Kelleher et al. Target report for target cell Edna. *Jefferson Laboratory*, 2007.

[15] Timothy Ngo et al. Neutron Arm Geometry for the G_E^n Experiment. *Jefferson Laboratory, www.jlab.org/∼ngo*, 2007.

APPENDICES

The appendix serves to provide further geometrical information pertaining to the geometry of the Neutron Arm and timing offsets used. This detail was essential in recreating the different positions of the many scintillator bars required for analysis.

Although measurements on the position of the detector as a whole was taken by the survey team, the information on the position of the different cassette, how they fit in the frame of the Neutron Arm, and subsequently the individual scintillator bars had to be meticulously measured by me and Jonathan Miller, after the experiment was finished and the detector was taken apart. It was only after these measurements were finished that the survey team's report could be used to locate the different bars in the hall of the experiment. A majority of these drawings are drawn to scale and incorporate all of the measurements made after the detector had been disassembled. I also wrote and submitted a complete technical document detailing the Neutron Arm Geometry to Jefferson Laboratory [15].

A NEUTRON ARM GEOMETRY

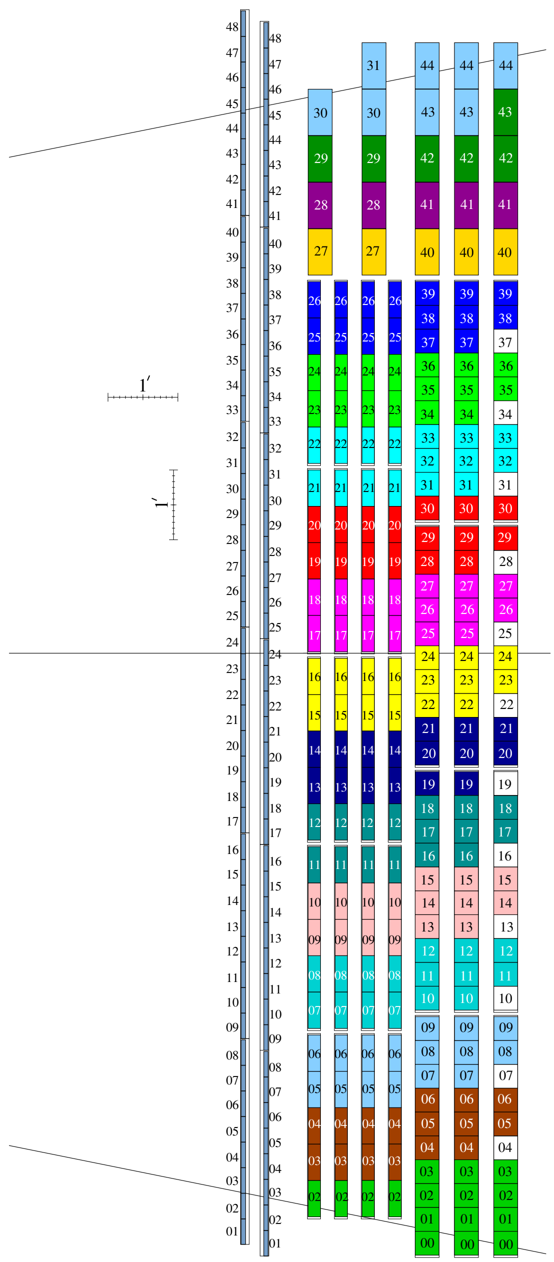

Figure 85: Side view of Neutron Detector with proper scale. Courtesy of Igor Rachek

A.1 PLANES OF THE NEUTRON ARM

The Neutron Arm contains overall ten planes of detectors, two of which are made up of veto counters which are described as V1 and shown in Fig 86 and V2 shown in Fig 87, one plane for the Marker counter Fig 88, and the rest are neutron detectors labeled N1 through N7. The next set of diagrams describes how the individual planes are created with the use of different cassettes. The majority of cassettes have a T-spacer at the top that is half inch (1.27cm) thick, however Glasgow cassettes N1.1, N2.1, and N7.4 have 2 spacers totaling one inch (2.54cm) and veto V1.1 has no spacers. The measurements of the detector bars are with respect to the top of the first detector bar. The active centers drawn are the centers of the detector bars and not of the cassette. Also the active center of V1 and V2 planes are offset from each other by one inch away from the active center of the CMU cassettes in the N1 plane.

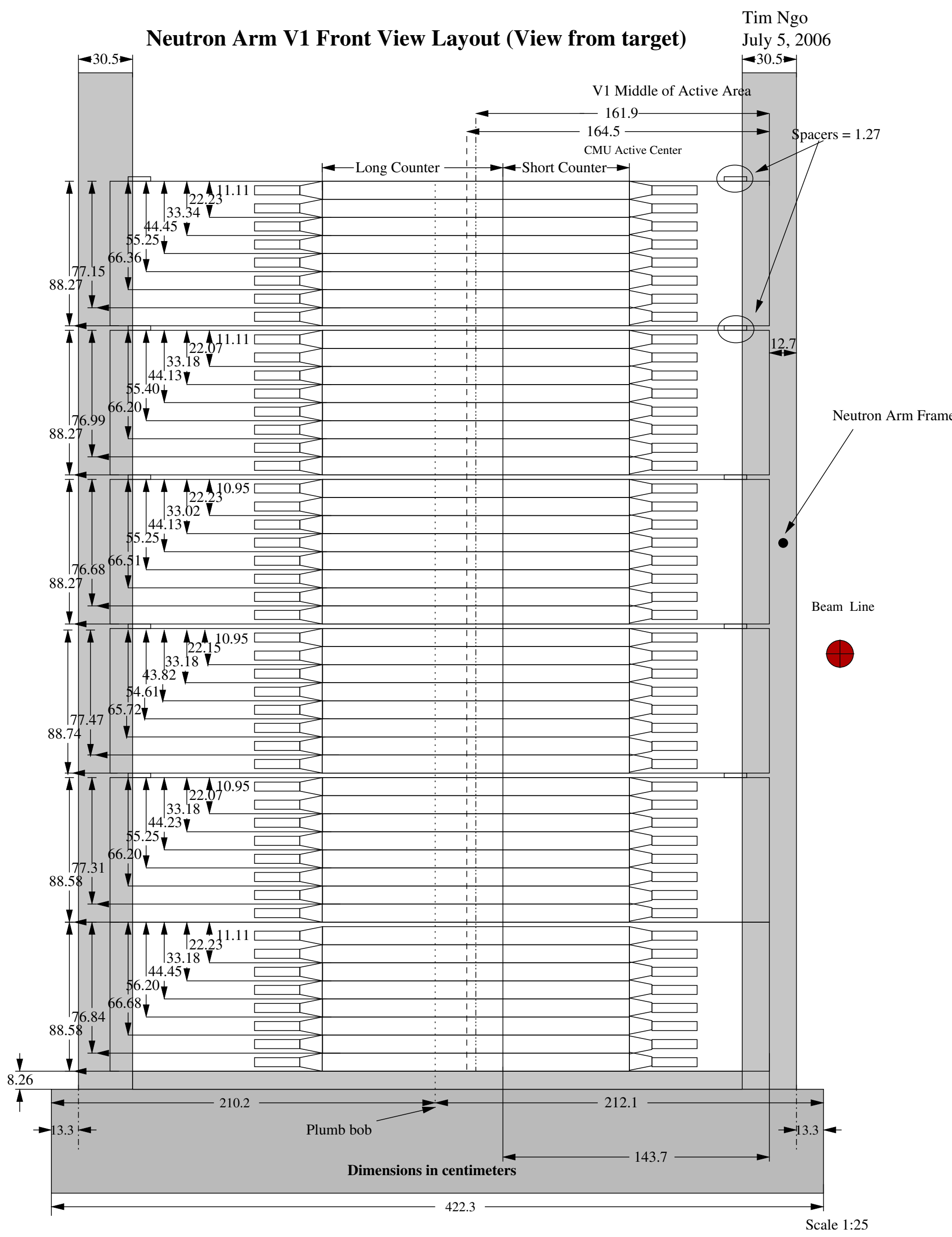

Figure 86: Veto1 Plane

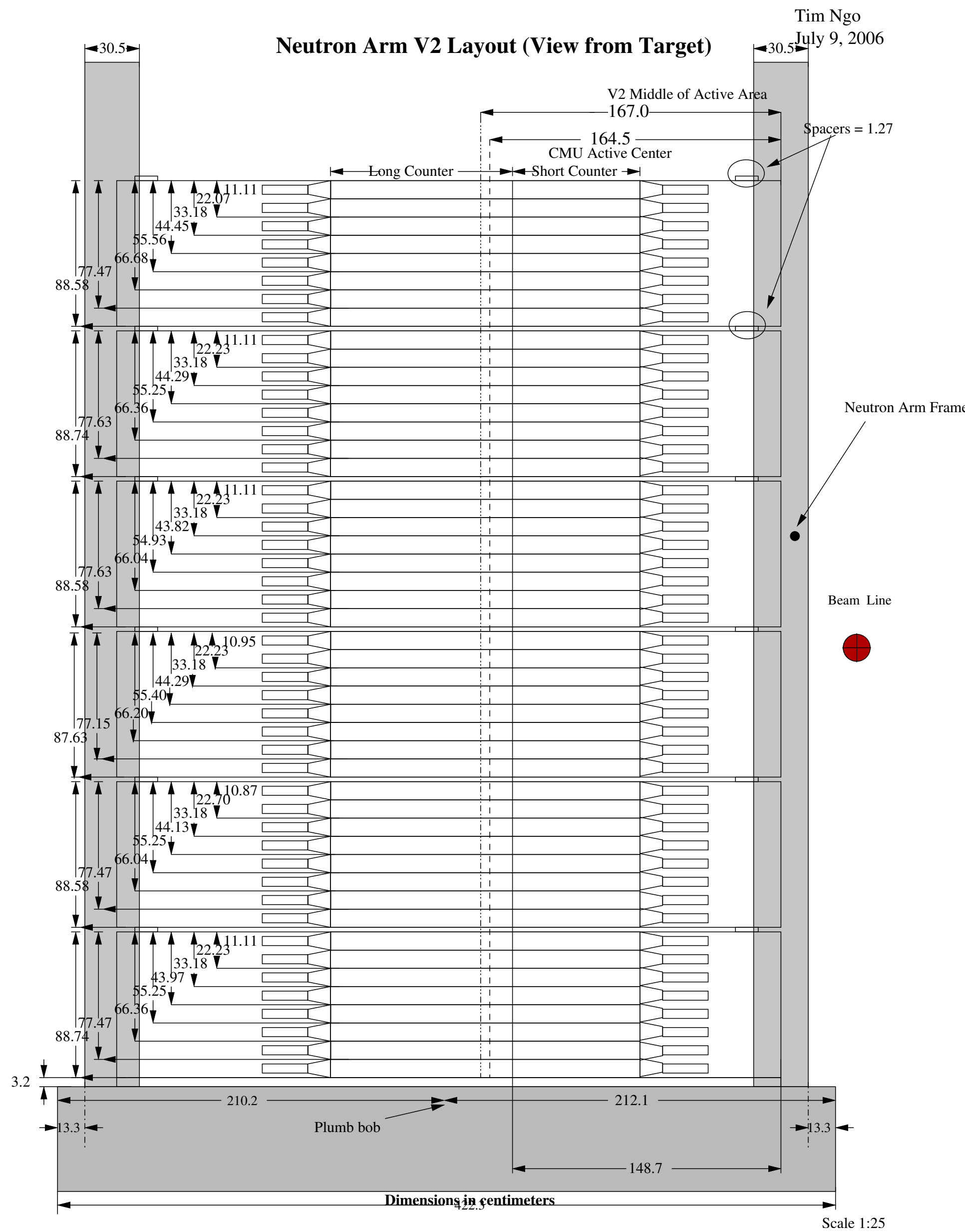

Figure 87: Veto2 Plane

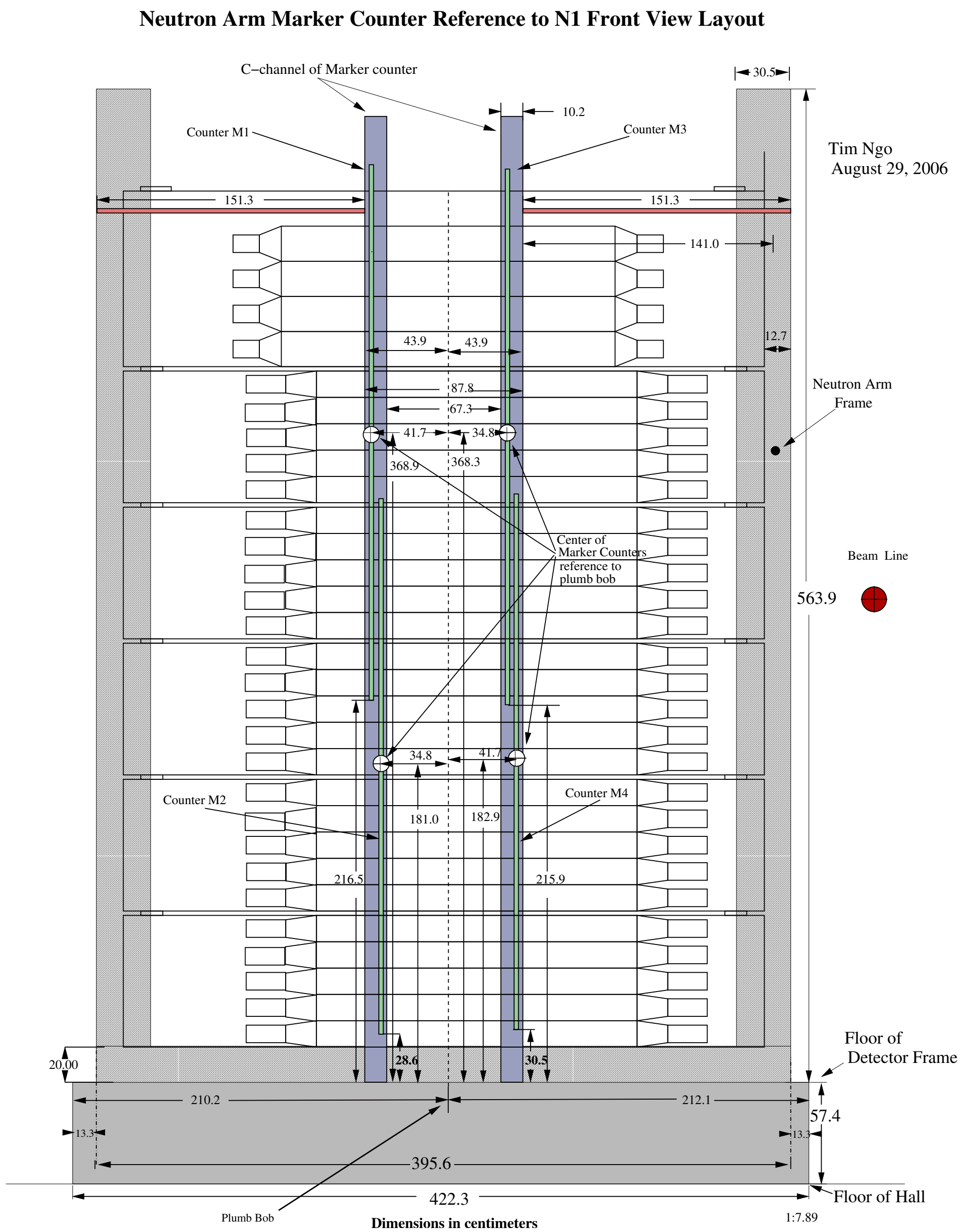

Figure 88: A majority of the dimensions for the Marker counters were provided in a report by Dimitri Nikolenko

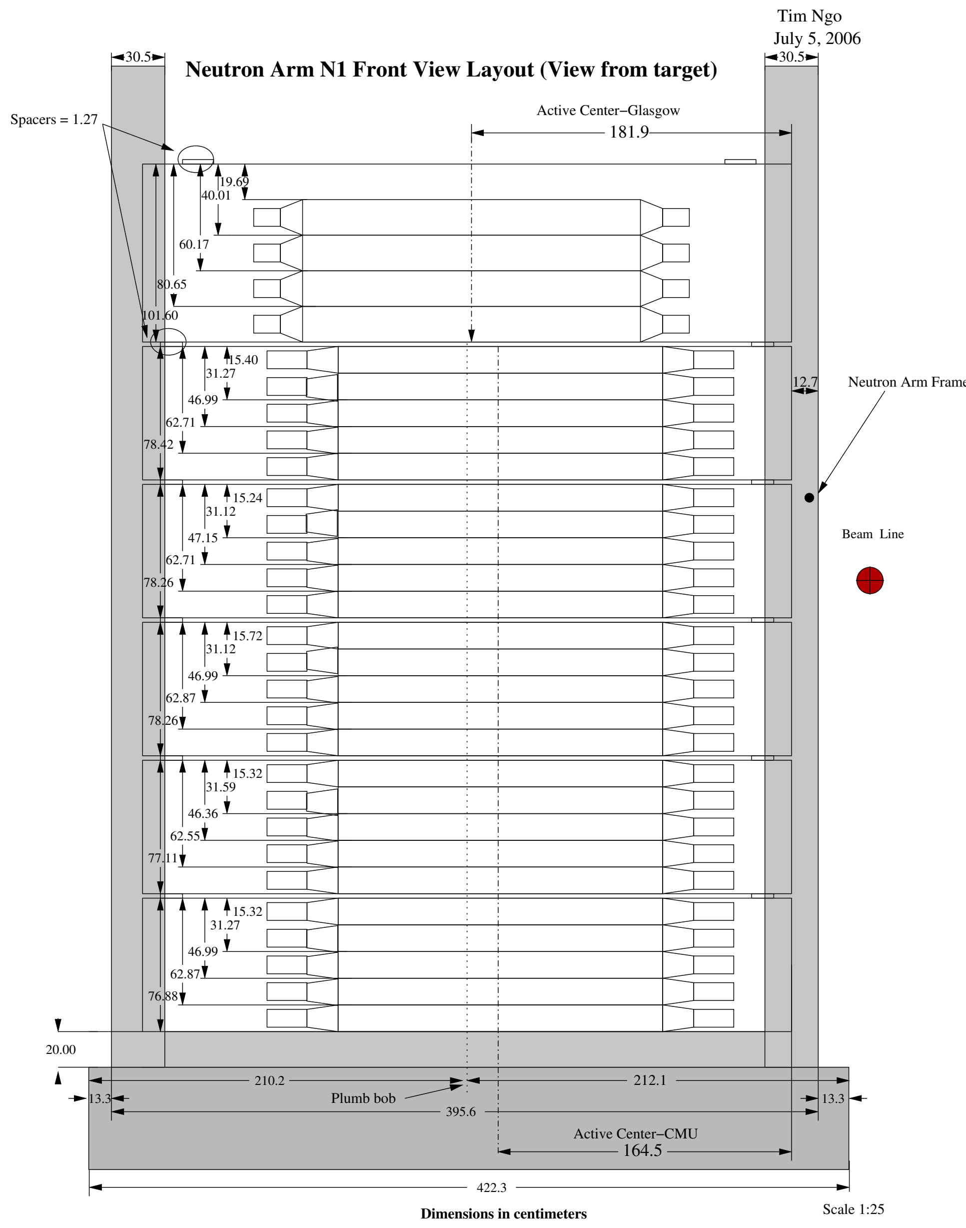

Figure 89: N1 Plane

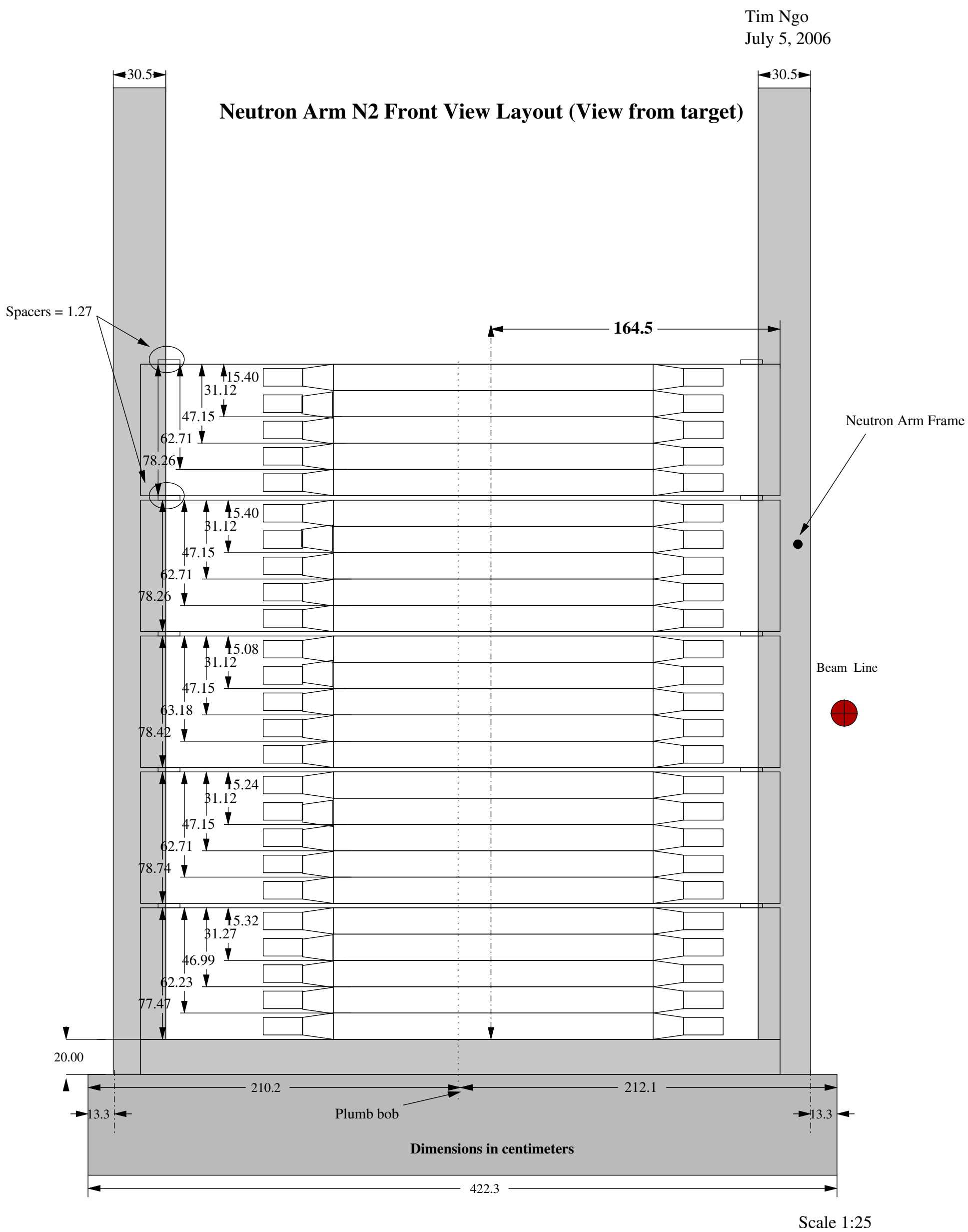

Figure 90: N2 Plane

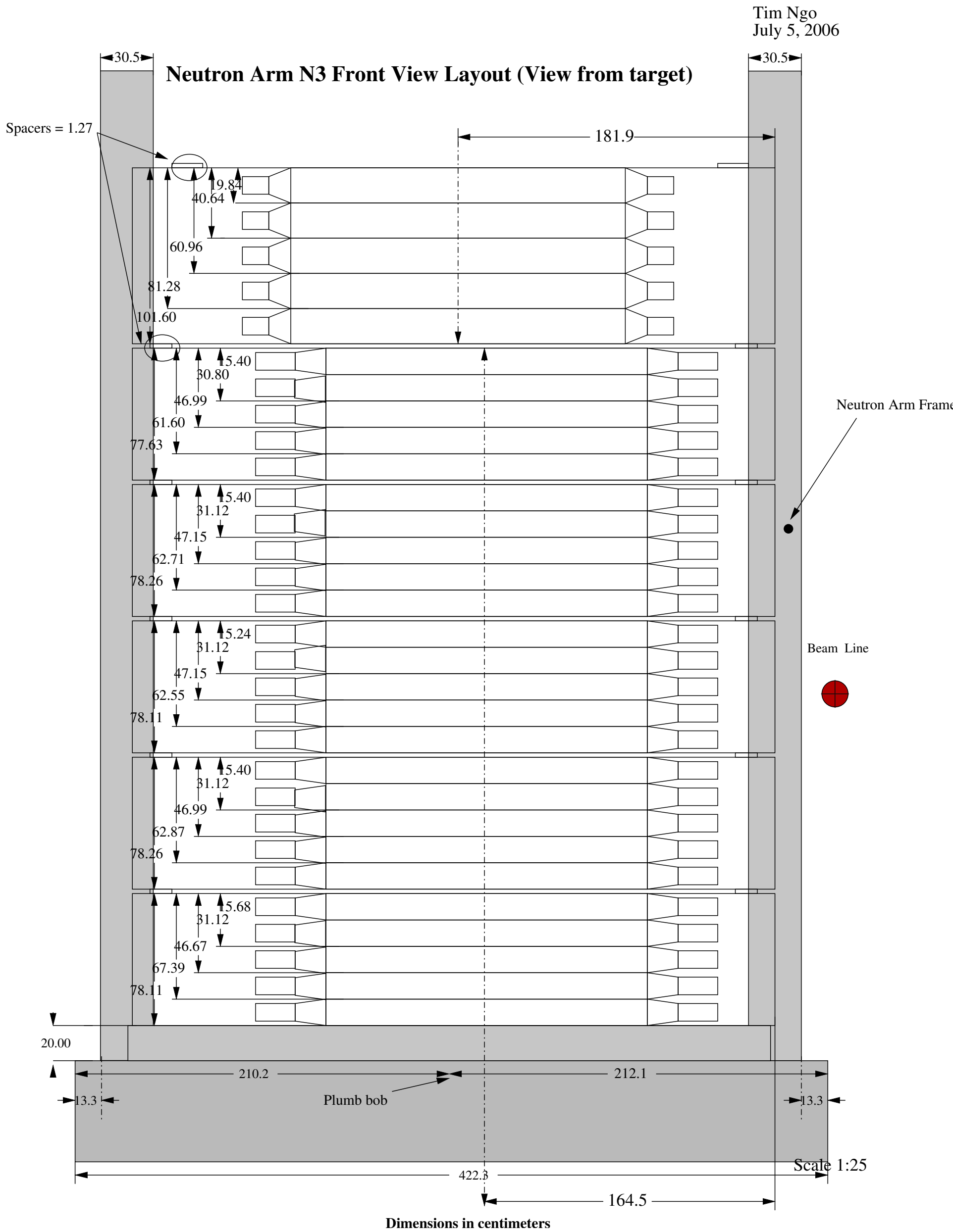

Figure 91: N3 Plane

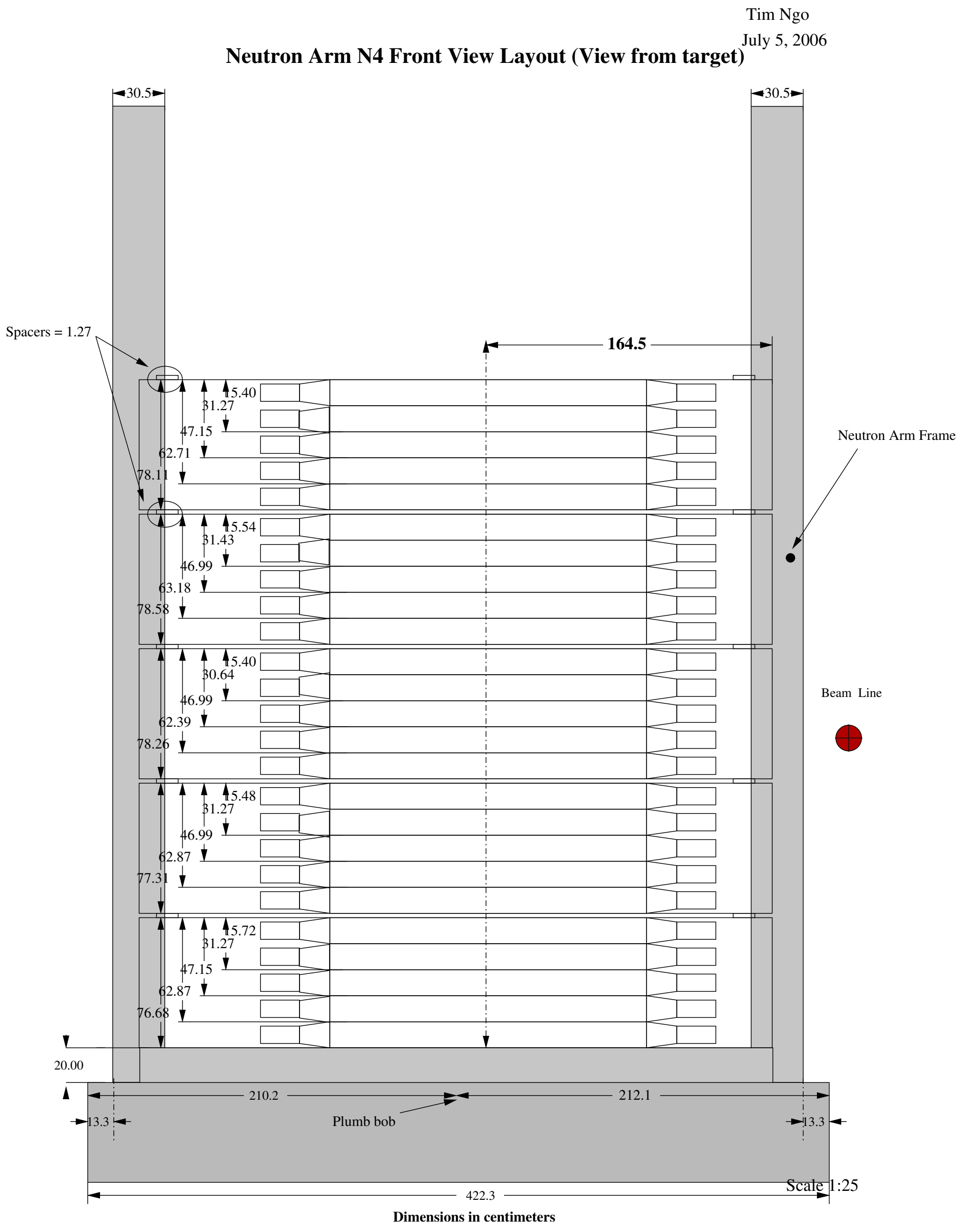

Figure 92: N4 Plane

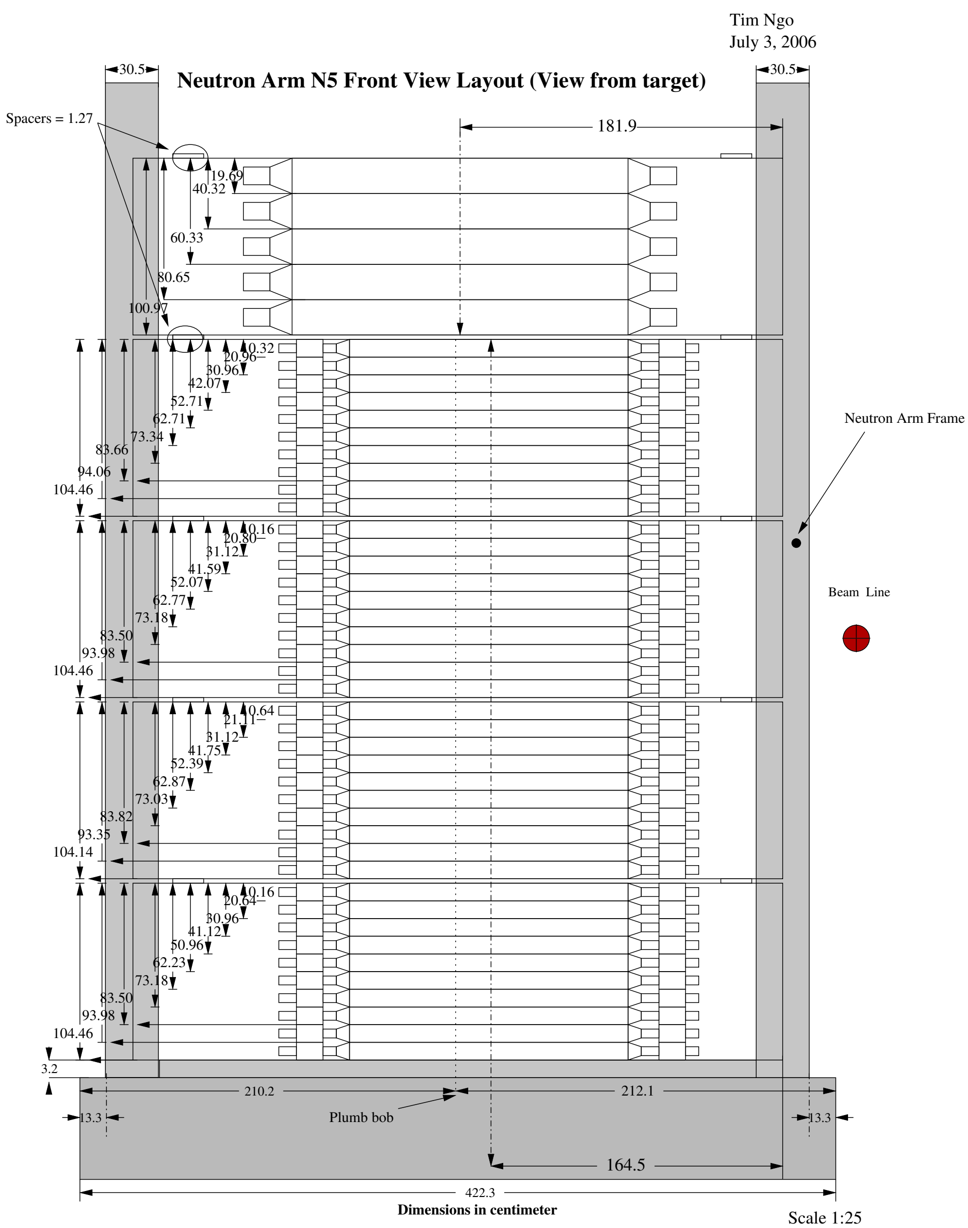

Figure 93: N5 Plane

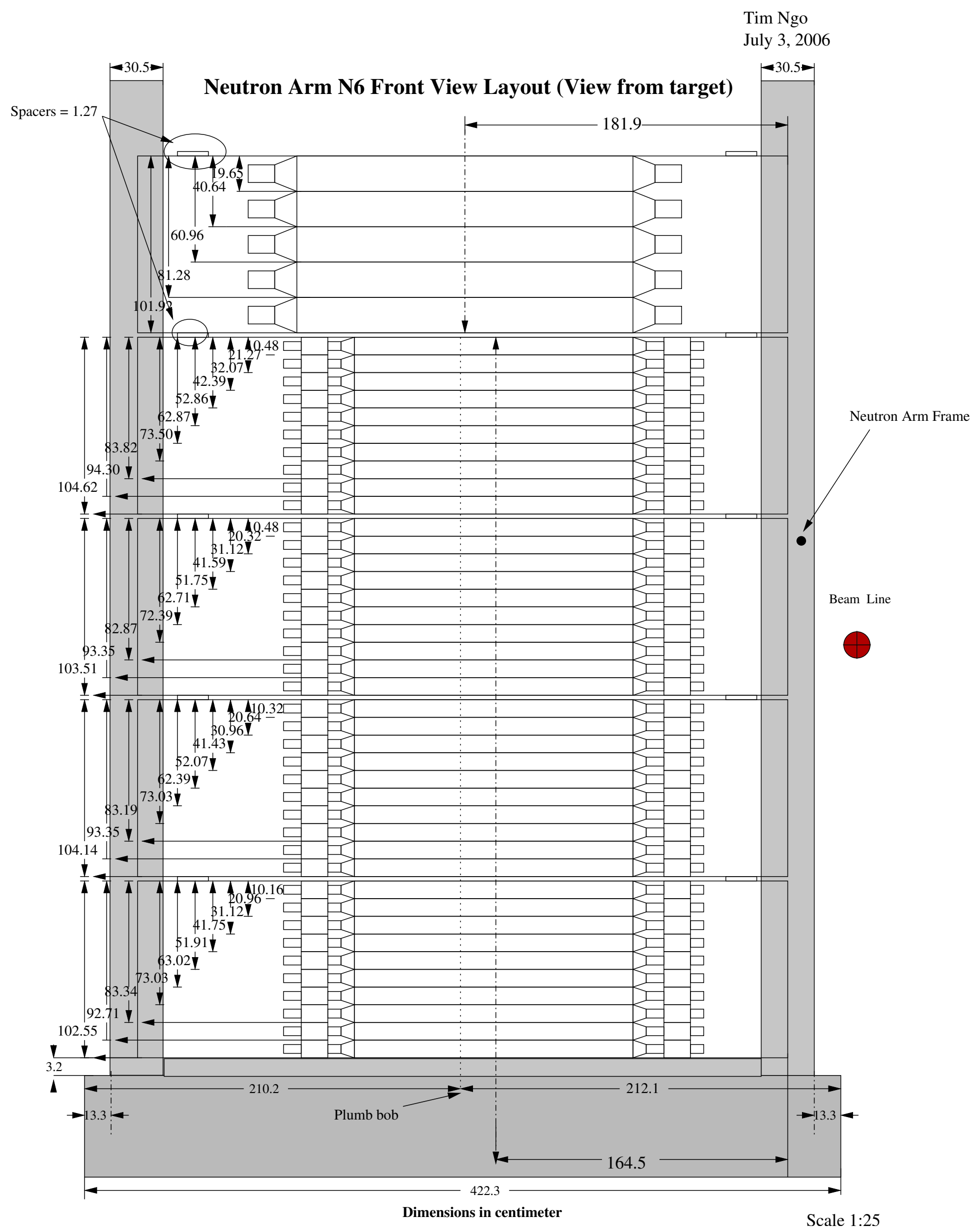

Figure 94: N6 Plane

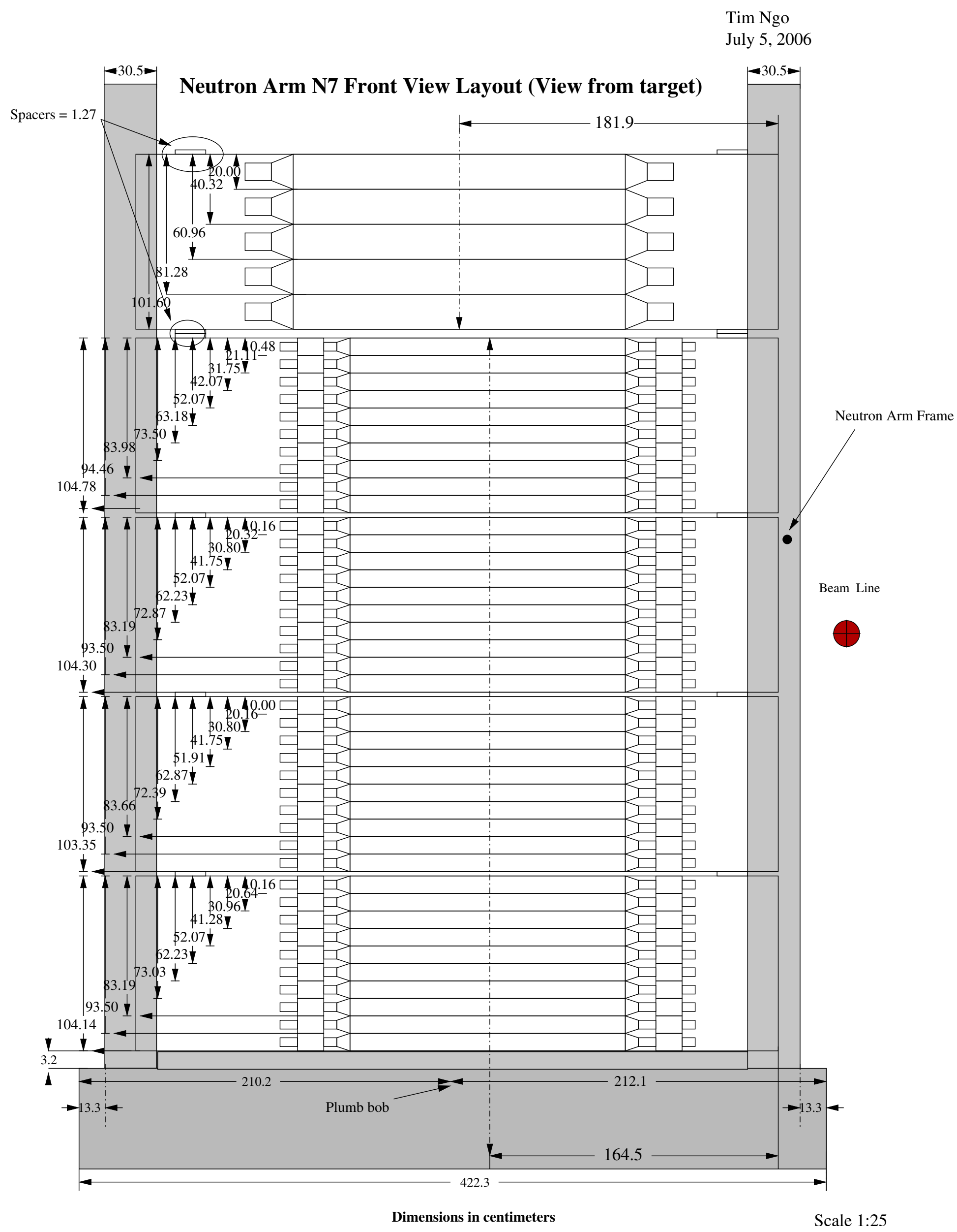

Figure 95: N7 Plane

A.2 CASSETTE GEOMETRY AND COUNTER PROFILE

The geometry of the cassettes Fig 96 shows the dimensions of each of the four different cassettes. The CMU, UVA, and Glasgow have very similar structures aside from the different size of the actual detector bars. These have two half inch plates of iron on the front of the cassette and one quarter inch plate of aluminum on the back. The veto counters however are different because of the aluminum struts that are used to hold the detector bars. Veto cassettes are made up of long and short counters. The shorter counter is located closer to the beam then the long counters. Veto cassettes have only one plate of half inch iron on the front. The profile of the different type of counters is shown in Fig 97.

3D View of Cassette

Neutron Arm Cassette Geometry

Veto Cassette (V1, V2)

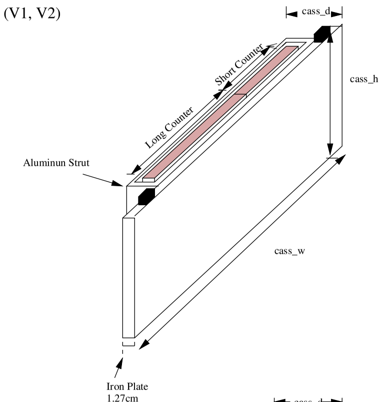

CMU,NA NU, Glasgow Cassette (N1−N7)

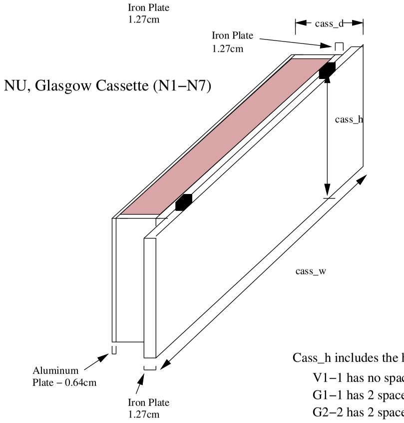

	cass_h	cass_w	cass_d
V.1.1	89.85	365.76	7.72
V.1.2	89.85	365.76	7.80
V.1.3	89.85	365.76	7.85
V.1.4	89.85	365.76	7.72
V.1.5	89.85	365.76	7.75
V.1.6	89.85	365.76	7.75

	cass_h	cass_w	cass_d
V.2.1	89.85	365.76	7.72
V.2.2	89.85	365.76	7.80
V.2.3	89.85	365.76	7.75
V.2.4	89.85	365.76	7.80
V.2.5	89.85	365.76	7.72
V.2.6	89.85	365.76	7.77

	cass_h	cass_w	cass_d
N.1.1	82.55	365.76	9.91
N.1.2	82.55	365.76	10.06
N.1.3	82.55	365.76	10.01
N.1.4	82.55	365.76	10.13
N.1.5	82.55	365.76	9.86
G.1.1	104.14	365.76	15.9

	cass_h	cass_w	cass_d
N.2.1	82.55	365.76	9.83
N.2.2	82.55	365.76	9.78
N.2.3	82.55	365.76	10.13
N.2.4	82.55	365.76	10.11
N.2.5	82.55	365.76	9.86

	cass_h	cass_w	cass_d
N.3.1	82.55	365.76	9.91
N.3.2	82.55	365.76	9.75
N.3.3	82.55	365.76	9.78
N.3.4	82.55	365.76	9.93
N.3.5	82.55	365.76	10.16
G.3.1	104.14	365.76	15.88

	cass_h	cass_w	cass_d
N.4.1	82.55	365.76	9.91
N.4.2	82.55	365.76	9.88
N.4.3	82.55	365.76	9.83
N.4.4	82.55	365.76	9.96
N.4.5	82.55	365.76	10.16

	cass_h	cass_w	cass_d
N.5.1	107.31	365.76	14.50
N.5.2	107.31	365.76	14.22
N.5.3	107.31	365.76	14.53
N.5.4	107.31	365.76	13.97
G.3.1	104.14	365.76	15.88

	cass_h	cass_w	cass_d
N.6.1	107.31	365.76	14.00
N.6.2	107.31	365.76	14.17
N.6.3	107.31	365.76	14.40
N.6.4	107.31	365.76	14.35
G.4.1	104.14	365.76	16.00

	cass_h	cass_w	cass_d
N.7.1	107.31	365.76	14.53
N.7.2	107.31	365.76	14.27
N.7.3	107.31	365.76	14.40
N.7.4	107.31	365.76	14.50
G.5.1	104.14	365.76	15.90

Cass_h includes the height of the spacers.
V1−1 has no spacers.
G1−1 has 2 spacers.
G2−2 has 2 spacers.
N3−4 has 2 spacers.

Tim Ngo
June 07, 2006

Figure 96: Cassette Geometry

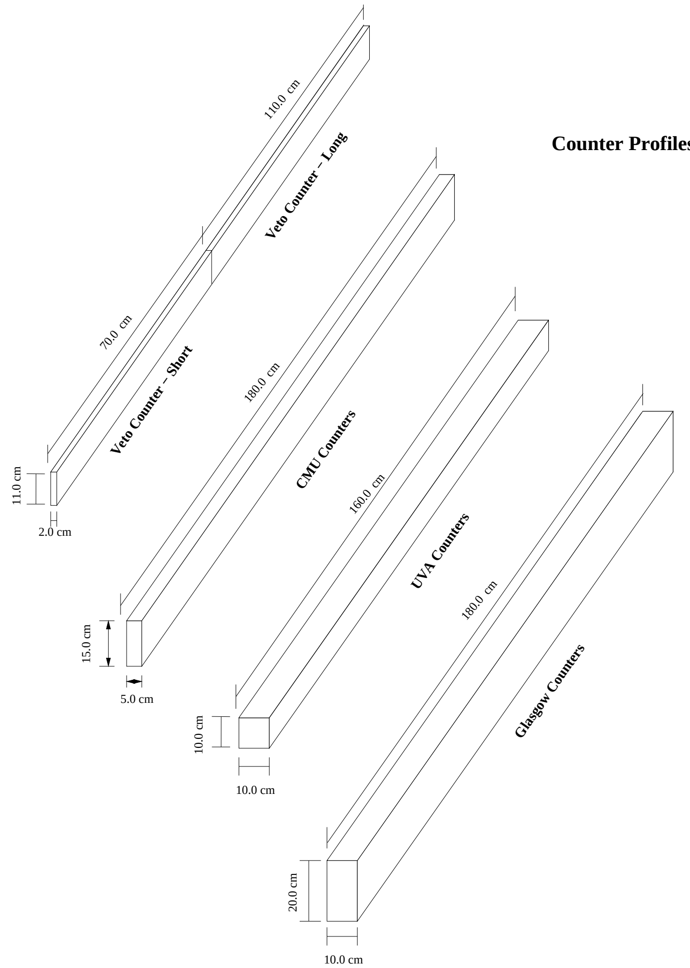

Figure 97: The different types of counters used in the Neutron Arm.

Jefferson Lab Alignment Group

Data Transmittal

TO: B. Wojtsekhowski, J. LeRose		**DATE:** 11 Jan 2006
FROM: Chris Curtis	**Checked:**	**# :** A1029

DETAILS:

Below are the results of the first three position surveys for the Hall A Big Hand detector. Four fiducials on each side of the detector were shot (labeled clockwise from bottom left), together with the central plumb bob point ("Ctr"). Coordinates are in millimeters based on the ideal target location as origin. Positive Z is downstream along the beamline, positive X is to the beam right, and positive Y is up.

Position #1 – Left Outer Rail (2A\HallA\060106B)

	Z(mm)	X(mm)	Y(mm)
CTR1	9649.9	5155.3	-2510.0
HABHA	10996.1	3557.2	-1341.2
HABHB	10994.1	3555.4	901.5
HABHC	12231.0	4272.8	897.5
HABHD	12220.4	4274.4	-1340.9
HABHE	10169.5	7809.9	-1325.3
HABHF	10167.9	7802.0	916.1
HABHG	8945.1	7090.0	917.1
HABHH	8939.2	7086.7	-1325.4

Position #2 – Right Outer Rail (2A\HallA\060106C)

	Z(mm)	X(mm)	Y(mm)
CTR2	9889.7	4736.9	-2509.8
HABHA	11233.8	3137.6	-1340.5
HABHB	11230.9	3135.8	902.2
HABHC	12468.4	3852.1	898.8
HABHD	12458.9	3853.6	-1339.6
HABHE	10411.1	7391.0	-1324.9
HABHF	10408.5	7383.1	916.4
HABHG	9184.9	6672.3	916.9
HABHH	9180.1	6668.9	-1325.6

Figure 98: Survey Data A1029 Page 1

Position #3 – Center Rail **(2A\HallA\060106A)**

CTR3	6682.7	4803.9	-2512.9
HABHA	8027.3	3209.1	-1338.1
HABHB	8021.5	3212.3	904.6
HABHC	9258.3	3929.8	901.1
HABHD	9251.4	3926.7	-1337.3
HABHE	7198.1	7460.8	-1332.8
HABHF	7192.1	7457.2	908.7
HABHG	5969.2	6745.2	908.5
HABHH	5968.2	6737.2	-1334.1

Figure 99: Survey Data A1029 Page 2

Jefferson Lab Alignment Group

Data Transmittal

TO: B, Wojtsekhowski, E. Chudakov, J. LeRose		**DATE:** 16 Feb 2006	
FROM: Chris Curtis	**Checked:**		**# :** A1040

DETAILS:

Below are the locations of the foil targets on the Big Hand detector in the four run positions. Four foil targets were added on each side of the and measured once. These locations are derived from the surveys reported on DTM #A1029 and a further survey carries out on Feb 14, 2006. The foils are labeled clockwise from bottom left. Coordinates are in millimeters based on the ideal target location as origin. Positive Z is downstream along the beamline, positive X is to the beam right, and positive Y is up.

Position #1 – Left Outer Rail (2A\HallA\060106B)

	Z(mm)	X(mm)	Y(mm)
BHF1	11185.2	3893.2	-1373.1
BHF2	11203.2	3898.9	1779.2
BHF3	11958.2	4334.7	1764.4
BHF4	11940.5	4335.1	-1435.7
BHF5	10082.3	7530.6	-1343.3
BHF6	10083.7	7521.5	1796.8
BHF7	9322.3	7087.0	1800.1
BHF8	9320.6	7086.5	-1328.9

Position #2 – Right Outer Rail (2A\HallA\060106C)

BHF1	11423.3	3473.4	-1372.3
BHF2	11439.9	3479.1	1780.0
BHF3	12195.3	3914.3	1765.5
BHF4	12179.0	3914.6	-1434.6
BHF5	10323.6	7111.8	-1343.0
BHF6	10323.7	7102.8	1797.1
BHF7	9561.9	6668.9	1800.1
BHF8	9561.5	6668.3	-1328.9

Position #3 – Center Rail (2A\HallA\060106A)

Figure 100: Survey Data A1040 Page 1

BHF1	8216.5	3545.0	-1370.6
BHF2	8228.6	3557.3	1781.8
BHF3	8983.3	3993.6	1767.4
BHF4	8971.6	3987.2	-1432.7
BHF5	7111.0	7181.6	-1350.6
BHF6	7106.5	7179.2	1789.6
BHF7	6345.4	6744.1	1792.4
BHF8	6349.5	6736.9	-1336.6

Jefferson Lab Alignment Group Data Transmittal Continued		**Page**	2	**of**	2
Date :	Feb 16, 2006	**Transmittal # :**	A1040		

Position #4 – Inner Rail / Start Position (2B\HallA\060214A)

	Z(mm)	X(mm)	Y(mm)
BHF1	5975.1	1971.0	-1357.3
BHF2	6007.4	2000.5	1794.8
BHF3	6761.2	2438.1	1773.3
BHF4	6728.9	2414.3	-1426.6
BHF5	4862.8	5605.7	-1349.8
BHF6	4878.6	5620.3	1790.3
BHF7	4118.3	5183.8	1800.4
BHF8	4102.4	5159.7	-1328.5

Figure 101: Survey Data A1040 Page 2

Jefferson Lab Alignment Group

Data Transmittal

TO: B, Wojtsekhowski, E. Chudakov, T. Ngo, J. LeRose		**DATE:** 13 Jul, 2006
FROM: Chris Curtis	**Checked:**	**#:** A1068

DETAILS:

Below are the locations of the fiducial blocks and foil targets on the Big Hand detector in the four post-run surveys. Only the fiducial blocks were measured directly. The foil target locations were derived from the survey of the fiducial blocks and a tie survey carried out on Feb 1st, 2006. The targets are labeled clockwise from bottom left, with the fiducial blocks as A-H and the foils as 1-8. Coordinates are in millimeters based on the ideal target location as origin. Positive Z is downstream along the beamline, positive X is to the beam right, and positive Y is up.

Position #1 – Left Outer Rail (2B\HallA\Gen\060515a)

	Z(mm)	X(mm)	Y(mm)
HABHA	11002.1	3565.0	-1342.2
HABHB	11000.7	3565.5	900.6
HABHC	12237.2	4284.0	895.3
HABHD	12225.1	4284.8	-1343.2
HABHE	10161.3	7814.0	-1327.2
HABHF	10157.2	7804.3	914.3
HABHG	8934.9	7091.2	912.9
HABHH	8932.7	7087.9	-1329.6
BHF1	11191.0	3901.4	-1374.9
BHF2	11207.6	3907.6	1777.4
BHF3	11960.9	4346.2	1762.9
BHF4	11944.7	4346.1	-1437.2
BHF5	10074.3	7534.6	-1346.1
BHF6	10074.3	7525.9	1794.0
BHF7	9314.6	7088.5	1797.1
BHF8	9314.3	7087.6	-1332.0

Position #2 – Right Outer Rail (2B\HallA\Gen\060515b)

HABHA	11242.0	3149.1	-1341.6
HABHB	11239.4	3149.2	901.1
HABHC	12475.3	3869.0	896.6
HABHD	12464.2	3870.2	-1341.9
HABHE	10396.7	7397.2	-1326.4
HABHF	10391.5	7387.1	915.1
HABHG	9170.0	6672.8	913.0
HABHH	9168.9	6669.8	-1329.5
BHF1	11430.6	3485.7	-1374.2
BHF2	11445.5	3491.4	1778.1
BHF3	12198.4	3930.9	1764.0
BHF4	12183.8	3931.2	-1436.1
BHF5	10310.0	7117.7	-1345.4
BHF6	10308.5	7108.5	1794.7
BHF7	9549.2	6670.3	1797.3
BHF8	9550.4	6669.9	-1331.7

Figure 102: Survey Data A1068 Page 1

Jefferson Lab Alignment Group Data Transmittal Continued	Page 2 of 2
Date : 13 July, 2006	Transmittal # : A1068

Position #3 – Center Rail (2B\HallA\Gen\060511a)

	Z(mm)	X(mm)	Y(mm)
HABHA	8026.2	3208.1	-1339.5
HABHB	8020.3	3212.6	903.2
HABHC	9259.0	3927.5	899.2
HABHD	9251.3	3924.4	-1339.4
HABHE	7197.8	7459.5	-1333.8
HABHF	7189.3	7453.9	907.7
HABHG	5964.9	6744.4	905.2
HABHH	5967.1	6737.1	-1337.3
BHF1	8216.1	3543.9	-1372.5
BHF2	8226.5	3555.7	1779.9
BHF3	8981.2	3992.1	1766.0
BHF4	8971.2	3986.3	-1434.1
BHF5	7110.0	7180.4	-1352.4
BHF6	7103.9	7177.4	1787.7
BHF7	6342.8	6742.2	1790.1
BHF8	6348.7	6735.6	-1338.9

Position #4 – Extreme Left Outer Rail (2B\HallA\Gen\060512b)

HABHA	10796.7	3914.2	-1343.1
HABHB	10796.1	3914.1	899.7
HABHC	12033.4	4631.4	894.2
HABHD	12020.4	4632.8	-1344.3
HABHE	9960.2	8164.0	-1326.7
HABHF	9956.9	8153.8	914.8
HABHG	8734.0	7441.9	913.7
HABHH	8730.8	7439.2	-1328.8
BHF1	10985.9	4250.4	-1375.8
BHF2	11003.7	4255.8	1776.5
BHF3	11757.5	4693.7	1761.8
BHF4	11740.0	4694.4	-1438.3
BHF5	9872.9	7884.8	-1345.7
BHF6	9874.1	7875.3	1794.4
BHF7	9113.9	7438.6	1797.7
BHF8	9112.4	7438.5	-1331.3

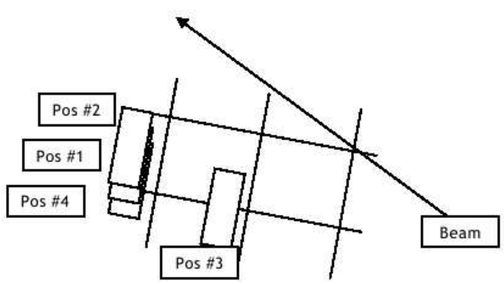

Figure 103: Survey Data A1068 Page 2

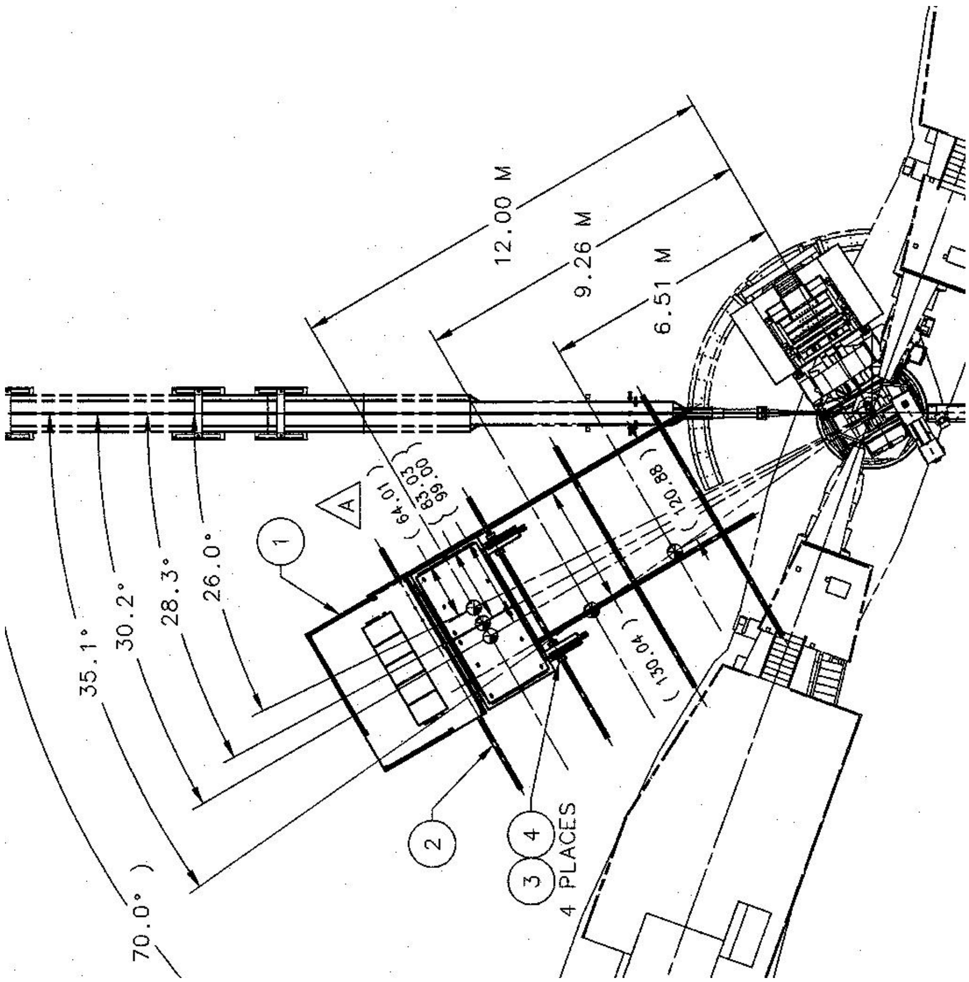

Figure 104: Neutron Arm on Track Schematic provided by Robby Hicks drawing 65520-D-34037-00 on 07/20/06

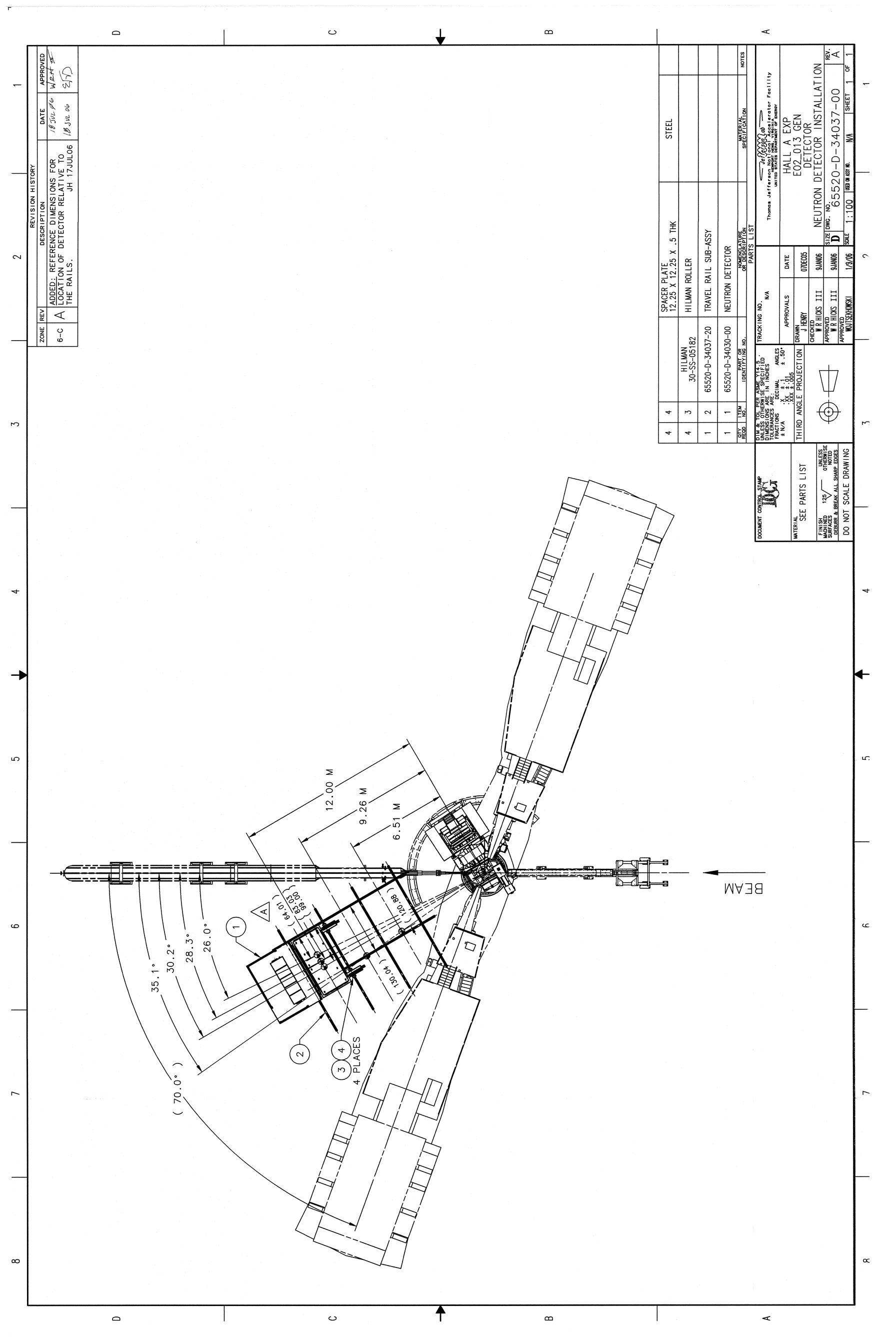

Figure 105: Neutron Arm on Track Schematic provided by Robby Hicks drawing 65520-D-34037-00 on 07/20/06

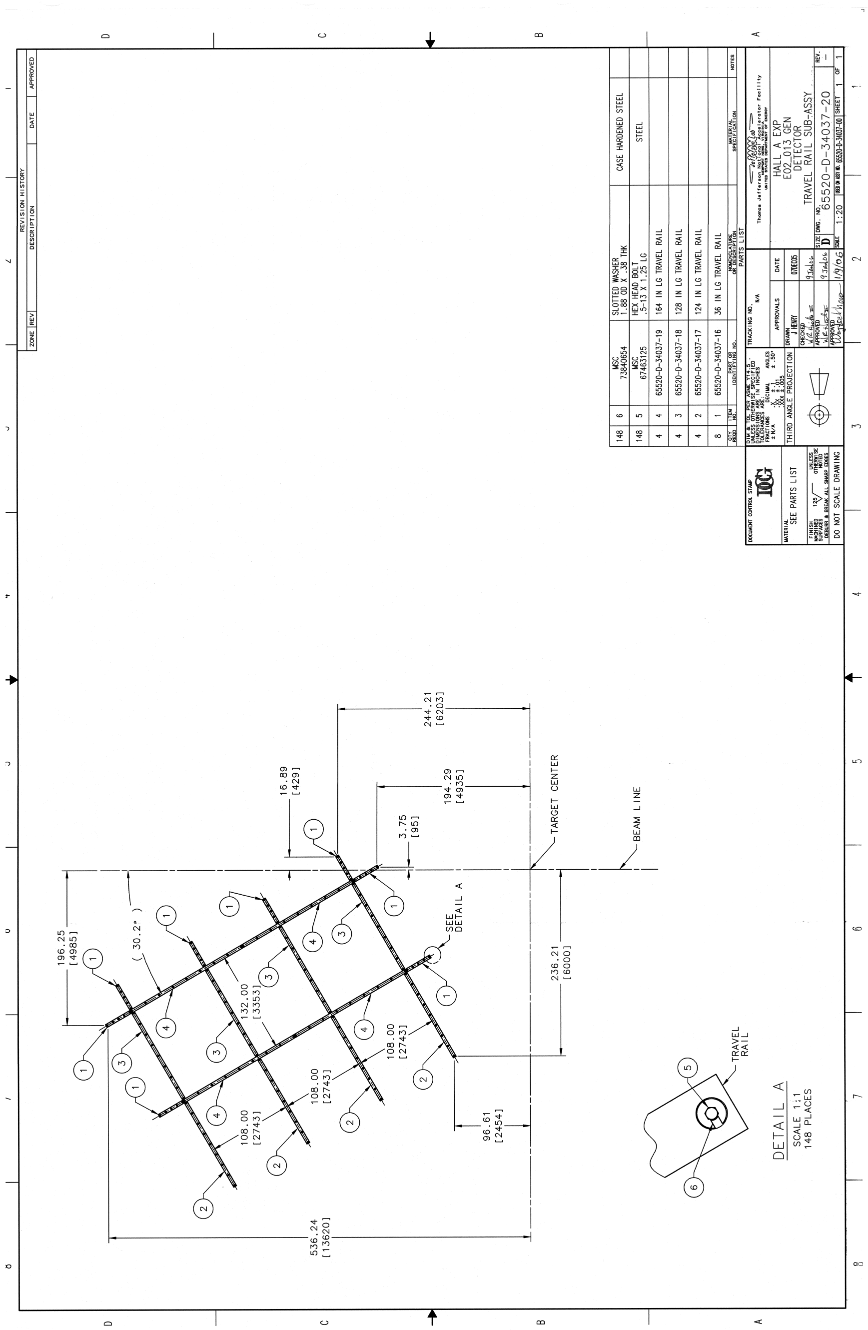

Figure 106: Neutron Arm on Track Schematic provided by Robby Hicks drawing 65520-D-34037-20 on 07/20/06

A.5 NEUTRON ARM ASSEMBLY DRAWING

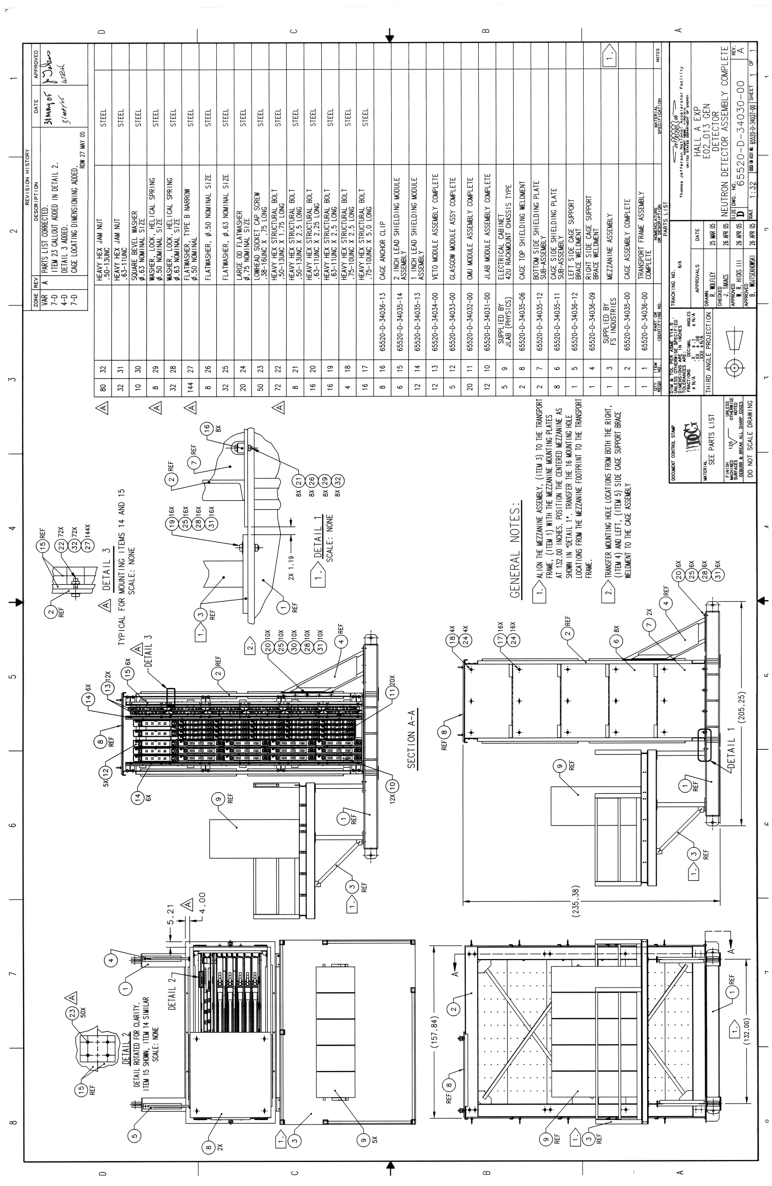

Figure 107: Final Neutron Detector Assembly Schematic by Robby Hicks

B TIME OFFSET

The time offsets used for both the intraplane time of flight and time of flight from the target to the N1 plane of the Neutron Arm can be found in this section.

Intraplane Time Offsets Kinematic 4

Bar Number in N1 Plane	TOF Offset Target to N1 Plane	Plane N2-N1 Bar Number	Plane N2-N1 Offset (ns)	Plane N3-N1 Bar Number	Plane N3-N1 Offset (ns)	Plane N4-N1 Bar Number	Plane N4-N1 Offset (ns)	Plane N5-N1 Bar Number	Plane N5-N1 Offset (ns)	Plane N6-N1 Bar Number	Plane N6-N1 Offset (ns)	Plane N7-N1 Bar Number	Plane N7-N1 Offset (ns)
2	166.0575	2	0.7817	2	1.4341	2	1.6086	2	2.6613	2	2.5915	2	3.6401
3	166.9012	3	0.4765	3	1.0218	3	1.4857	3	1.9679	3	2.4936	3	3.6812
4	166.7488	4	0.5537	4	1.0391	4	1.4556	4	2.4894	4	2.8796	4	n/a
5	166.9631	5	0.4197	5	0.9164	5	1.4270	5	2.1673	5	2.9101	5	3.3860
6	166.8152	6	0.5328	6	1.0630	6	1.4749	6	2.1090	6	2.8051	6	3.4543
7	166.8924	7	0.5266	7	0.9108	7	1.3055	7	2.2605	7	2.9837	7	n/a
8	166.8880	8	0.4657	8	0.7867	8	1.3687	8	2.1751	8	2.9298	8	3.6120
9	166.8467	9	0.4227	9	0.8850	9	1.2718	9	2.1034	9	2.8812	9	3.4667
10	166.7849	10	0.3347	10	0.9208	10	1.3868	10	2.0726	10	2.6763	10	0.0000
11	166.6779	11	0.5370	11	1.0531	11	1.5058	11	1.9313	11	2.7688	11	3.5205
12	166.7333	12	0.7148	12	0.9695	12	1.2996	12	2.0698	12	2.7192	12	3.4685
13	166.7977	13	0.4644	13	0.8459	13	1.4001	13	2.1238	13	2.8594	13	n/a
14	166.7185	14	0.5386	14	0.8942	14	1.4614	14	2.0529	14	2.9241	14	3.6437
15	166.7283	15	0.3965	15	0.8673	15	1.4310	15	2.2565	15	2.9781	15	3.7821
16	166.6158	16	0.5214	16	0.8931	16	1.3900	16	2.1984	16	2.9021	16	n/a
17	166.5017	17	0.4683	17	1.1057	17	1.5123	17	2.0779	17	2.7714	17	3.7750
18	166.7495	18	0.3706	18	0.7397	18	1.2471	18	1.9458	18	2.7907	18	3.5507
19	166.5088	19	0.4961	19	0.9224	19	1.3519	19	2.0048	19	2.7944	19	n/a
20	166.4474	20	0.5007	20	0.9724	20	1.4130	20	1.8882	20	2.7726	20	3.7586
21	166.4464	21	0.4415	21	1.0601	21	1.4943	21	1.8649	21	2.7139	21	3.5364
22	166.3457	22	0.4293	22	1.0348	22	1.4792	22	1.8825	22	2.6482	22	n/a
23	166.2162	23	0.4328	23	1.0765	23	1.5069	23	1.8576	23	2.6889	23	3.6662
24	166.3846	24	0.4730	24	0.9569	24	1.4667	24	1.9096	24	2.7750	24	3.6820
25	166.3707	25	0.4750	25	0.9388	25	1.4437	25	1.9776	25	2.8245	25	n/a
26	166.4157	26	0.5060	26	1.0449	26	1.4387	26	1.8160	26	2.7400	26	3.6545
								27	1.8398	27	2.7172	27	3.6048
								28	1.9616	28	2.8002	28	3.8230
								29	1.9228	29	2.7557	29	3.7356
								30	1.9897	30	2.7641	30	3.6664
								31	1.9473	31	2.7929	31	n/a
								32	2.0065	32	2.8365	32	3.8682
								33	2.0729	33	2.9074	33	3.7797
								34	2.0881	34	2.8733	34	n/a
								35	1.9825	35	2.8124	35	3.9174
								36	1.8822	36	2.8037	36	3.8640
								37	1.9790	37	2.8369	37	n/a
								38	1.9290	38	2.8161	38	4.0287
								39	2.1067	39	3.0247	39	4.0130

Figure 108: Time offsets used to apply to kinematic 4 data.

Intraplane Time Offsets Kinematic 3

Bar Number in N1 Plane	TOF Offset Target to N1 Plane	Plane N2-N1 Bar Number	Plane N2-N1 Offset (ns)	Plane N3-N1 Bar Number	Plane N3-N1 Offset (ns)	Plane N4-N1 Bar Number	Plane N4-N1 Offset (ns)	Plane N5-N1 Bar Number	Plane N5-N1 Offset (ns)	Plane N6-N1 Bar Number	Plane N6-N1 Offset (ns)	Plane N7-N1 Bar Number	Plane N7-N1 Offset (ns)
2	170.2951	2	0.6139	2	1.0758	2	1.2528	2	2.2421	2	2.0666	2	3.1429
3	170.7875	3	0.4003	3	0.9562	3	1.4195	3	1.6641	3	2.0224	3	n/a
4	170.7605	4	0.4913	4	0.9998	4	1.3558	4	1.9785	4	2.7846	4	n/a
5	170.9900	5	0.3424	5	0.8463	5	1.2504	5	2.0278	5	2.6607	5	3.0268
6	170.7611	6	0.5357	6	1.0267	6	1.4203	6	1.8672	6	2.4412	6	2.9279
7	170.8376	7	0.5103	7	0.8305	7	1.1729	7	2.2054	7	2.5830	7	n/a
8	170.8971	8	0.3985	8	0.6952	8	1.2188	8	2.0294	8	2.6222	8	3.2228
9	170.8446	9	0.3722	9	0.7490	9	1.1722	9	1.9309	9	2.5545	9	3.1734
10	170.7734	10	0.2772	10	0.8079	10	1.2577	10	1.9264	10	2.5031	10	n/a
11	170.6168	11	0.5091	11	0.9652	11	1.3580	11	1.8273	11	2.4150	11	3.0868
12	170.6088	12	0.6917	12	0.9247	12	1.1622	12	1.8800	12	2.4411	12	3.0615
13	170.7957	13	0.4473	13	0.8123	13	1.2867	13	1.9122	13	2.5655	13	n/a
14	170.7777	14	0.4650	14	0.8156	14	1.3256	14	1.8557	14	2.5771	14	3.2464
15	170.7156	15	0.3675	15	0.7469	15	1.2468	15	2.0174	15	2.6351	15	3.2566
16	170.5727	16	0.4802	16	0.7727	16	1.2757	16	1.9987	16	2.5693	16	n/a
17	170.4798	17	0.3646	17	0.9769	17	1.3771	17	1.9418	17	2.4934	17	3.3352
18	170.6661	18	0.3255	18	0.6825	18	1.1390	18	1.7797	18	2.5075	18	3.2121
19	170.4303	19	0.6443	19	0.8103	19	1.3136	19	1.8610	19	2.5642	19	n/a
20	170.3860	20	0.5276	20	0.9520	20	1.3026	20	1.7897	20	2.4895	20	3.2208
21	170.4041	21	0.7115	21	0.9967	21	1.4144	21	1.7430	21	2.4691	21	3.1914
22	170.1715	22	0.4117	22	0.9391	22	1.4056	22	1.6652	22	2.3208	22	n/a
23	169.9862	23	0.4352	23	1.0248	23	1.4048	23	1.6855	23	2.4005	23	3.2701
24	170.4592	24	0.4786	24	0.8516	24	1.3451	24	1.7812	24	2.5067	24	3.2756
25	170.4431	25	0.4321	25	0.8511	25	1.1700	25	1.8158	25	2.4937	25	n/a
26	170.1889	26	0.5959	26	0.9431	26	1.3580	26	1.6581	26	2.4783	26	3.3106
								27	1.7450	27	2.4205	27	3.2809
								28	1.7927	28	2.4525	28	3.4409
								29	1.8086	29	2.4718	29	3.2761
								30	1.8755	30	2.5060	30	3.2858
								31	1.8080	31	2.4763	31	n/a
								32	1.8264	32	2.5524	32	3.4738
								33	1.8976	33	2.6499	33	3.3738
								34	1.8978	34	2.5251	34	n/a
								35	1.7678	35	2.6621	35	3.5582
								36	1.7050	36	2.4331	36	3.4036
								37	1.8705	37	2.5552	37	n/a
								38	1.8467	38	2.5966	38	3.5412
								39	2.0063	39	2.6414	39	3.6919

Figure 109: Time offsets used to apply to kinematic 3 data.